Resonant coherent excitation of relativistic heavy ions channeled in a Si crystal

（シリコン結晶内をチャネリングする相対論的重イオンの干渉性共鳴励起）

Takaomi Ito

Contents

List of symbols

a_B	Bohr radius
a_{TF}	Thomas-Fermi radius
c	Velocity of light
d	Distance between atoms along a crystal axis
d_p	Inter-planar distance
e	Charge of electron
f^{17}	Fraction of survived Ar^{17+} ions transmitted trough a crystal
h	Planck's constant
$\hbar$	Planck's constant divided by 2π
k, l	Indexes of resonance coherent excitation
m	Mass of electron
$n_e(x)$	Local electron density at position x
n_a	Number of quantum states of axial channeled ion
n_p	Number of quantum states of planar channeled ion
q	Sommerfeld parameter
u_1	RMS lattice vibration amplitude in one direction
υ	Ion velocity
υ_B	Bohr velocity
υ_F	Fermi velocity
$\upsilon_\perp$	Ion velocity perpendicular to channel axis or plane
w_{12}	Transition probability from $n = 1$ to 2 state
x	Distance from channel plane
z	Ion position parallel to beam direction
z_0	Target thickness
A, B	Constants in Eq.(2.96)
E_0	Incident ion energy
E_{out}	Energy of electron escaped from target
E_{es}	Sum of energy of escaped electrons per ion passage
E_{trans}	Transition energy of ion
$F_{n0}(\boldsymbol{K})$	Matrix element for transition from the ground state to n-th excited state
$\boldsymbol{G}_{n0}(\boldsymbol{K})$	Matrix element for transition originating from relativistic correction
$\boldsymbol{G}$	Reciprocal lattice vector
I	Mean ionization energy
$\boldsymbol{K}$	Momentum transfer divided by $\hbar$
M_1	Mass of projectile ion
M_2	Mass of target atom
M_{12}	Transition matrix element from $n = 1$ to 2 state
N	Atomic density of target
Q	$Q(1 + Q/2mc^2) = \hbar^2K^2/2m$
S	Stopping power
T	Energy transfer from ion to target atom
T_{osc}	Period of channeling oscillation
$V(r)$	Atomic potential
$U_a(\rho)$	Axial continuum potential
$U_p(x)$	Planar continuum potential

Z_1	Atomic number of projectile ion
Z_2	Atomic number of target atom
Z_{eff}	Effective charge of channeled ion
α	Fine structure constant
$\boldsymbol{\alpha}_j$	Dirac current operator of j-th electron
α_c	Contribution to stopping power for channeled ion from close collision
β	v/c
$\chi(x)$	Thomas-Fermi function
γ	$1/\sqrt{1-\beta^2}$
λ_i	Mean free path for ionization
λ_R	Path length of channeled ion per Rabi oscillation
λ_x	Mean free path for radiative decay
$\nu(k,l)$	Frequency of oscillating electromagnetic field for (k,l) resonance
ρ	Distance from crystal string
σ_L	Standard deviation of energy loss distribution
σ_D	Standard deviation of energy deposition distribution
ψ_1	Critical angle for axial channeling
ψ_p	Critical angle for planar channeling
ΔE_L	Energy loss
ΔE_D	Energy deposition
$\Delta\varepsilon$	Energy straggling
Ω	Frequency for Rabi oscillation

1. Introduction

Channeling effect was first observed in 1960, and many related phenomena, *e.g.*, stopping power of channeled ions or an angular distribution of transmitted ions, were extensively studied [1,2]. The channeling is a unique condition for ions, which has a small probability of collisions with target atoms, and there are several advantages for studying phenomena relevant to ion-solid collisions. For instance, the stopping power of partially stripped ions with frozen-charge state is easily measured because of a small probability of the charge exchange [3]. Atomic processes, such as radiative electron capture [4] or dielectronic recombination [5] are clearly observed because of a reduction of the background originating from bremsstrahlung. Moreover, studies on the impact parameter dependence of the energy loss and the charge state distribution of channeled ions can be performed [6,7].

Resonant coherent excitation (RCE) is one of the most interesting phenomena, which takes place under the channeling condition where the crystal periodic structure along the ion path is involved. The phenomenon in nuclear levels was predicted by Okorokov in 1965 [8]. The RCE in atomic levels was first observed by Datz *et al*. through a measurement of the charge state distribution of transmitted ions [9]. Fig.1.1 shows one of their results, which is in the case of N^{6+} incidence along to Au <111> axis, and resonance dips for k = 4, 5, 6 are seen. Fujimoto *et al*. observed the 6th order RCE of Ne^{9+} ions through a measurement of de-excitation X-rays (Fig.1.2) [10]. Since then, many theoretical [11-15] and experimental [16,17] RCE investigations were performed. For instance, yield of convoy electrons emitted from C^{5+} ions channeled along <100> axis was measured to increase under the RCE condition [18], and the result is shown in Fig.1.3. Combination of ions and crystal in several RCE experiments and the indexes for the resonance are listed in Table1. The previous studies were limited only for low energy region, because accelerators for ions with relativistic energy were not available. With low energy ions, only high order RCEs, which have small transition probabilities, can be observed. Recently, we can obtain a heavy ion beam with relativistic energy by synchrotron accelerators, *e.g.*, in GSI (Germany). Heavy Ion Medical Accelerator in Chiba (HIMAC) is one of the accelerators which are capable of providing relativistic heavy ions. A picture of HIMAC is shown in Fig.1.4. Ions extracted from the ion source are first accelerated by a linear accelerator to several MeV/u. After that, they are introduced to a synchrotron accelerator, and several 100 MeV/u ions are supplied to an area for experiments. We can obtain C, Ne, Si, Ar, Fe, Kr and Xe ions with the energies from 100 to 800 MeV/u. This thesis treats investigations at HIMAC on the RCE of 390 MeV/u hydrogen-like Ar ions from 1s to n = 2 states.

Table1 Combinations of ions and crystals in several RCE experiments and indexes of the resonance. Δn = 2, 3 means excitations to n = 3 and 4 from the ground state.

Ion	Channel axis or plane	Indexes for resonance	Ref.
C^{5+}, N^{6+}, O^{7+}, F^{8+}	Au <100>, <110>, <111>	k = 2, 3, 4, 5, 6	[9]
Ne^{9+}	Au <111>	k = 6	[10]
C^{5+}	Au <100>	k = 2	[18]
Mg^{11+}	Au <100>	k = 4	[19]
N^{6+}, Mg^{11+}	Au (100), Ni (100)	(k,l) = (2,0)	[20]
Si^{13+}	Si <111>	k = 7, 8 (Δn = 2, 3)	[21]

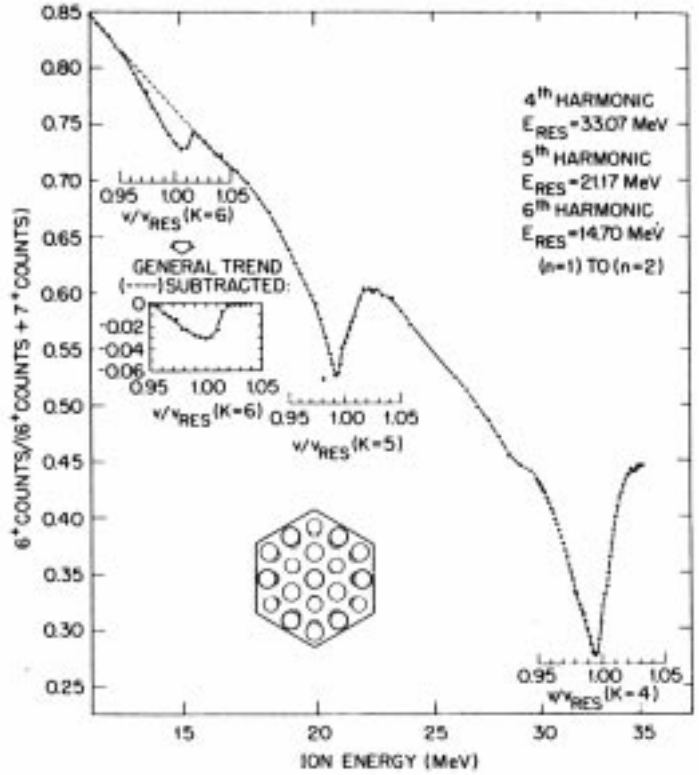

Fig.1.1 Survived N^{6+} fraction as a function of the incident energy for <111> axial channeling in Au [9].

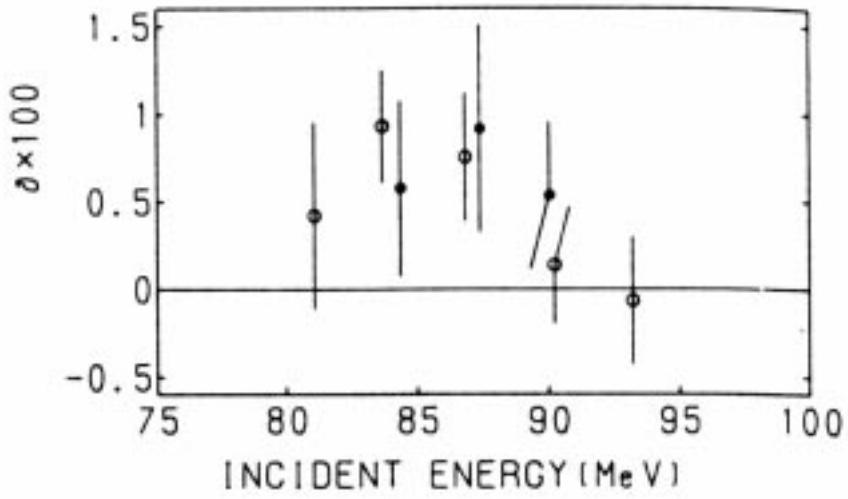

Fig.1.2 Difference of Ne^{9+} K α X-ray intensities normalized to Au M X-rays between <111> aligned and random incidence [10]. The resonance energy is 87.3 MeV.

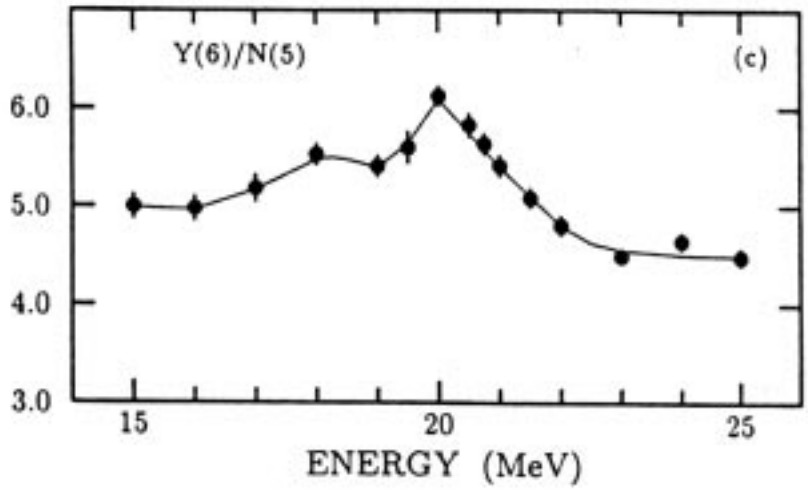

Fig.1.3 Yield of convoy electrons as a function of the incident energy normalized to the exit number of C^{5+} ions [18]. The resonance energy is 20.4 MeV.

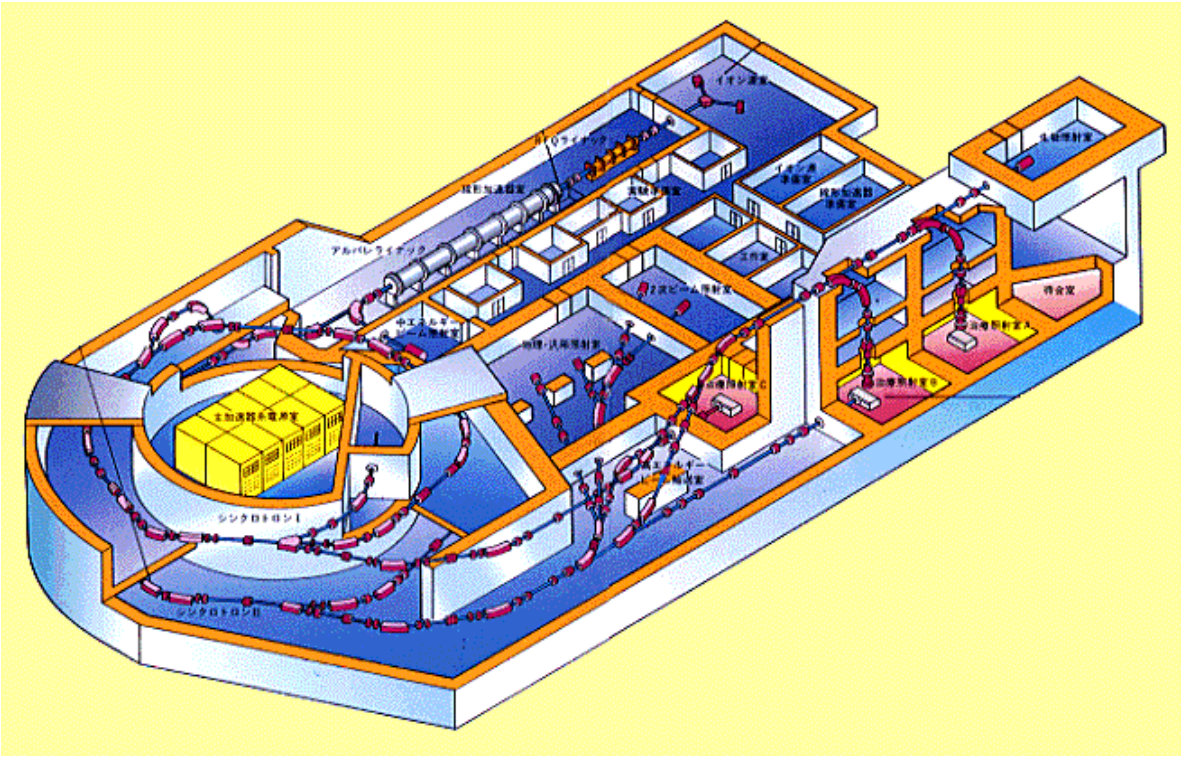

Fig.1.4 Picture of Heavy Ion Medical Accelerator in Chiba (HIMAC)

Channeled ions (also random incident ions) in a crystal experience several atomic processes, *i.e.*, excitation, electron loss (ionization) and electron capture, due to collisions with target atoms. In the case of hydrogen-like ions, a coherent excitation process from 1s to $n = 2$ states is added to the above incoherent processes under the RCE condition. Because a population of $n = 2$ states increases, both probabilities of ionization and radiative decay from $n = 2$ states become larger than that for off-resonance. Therefore, the RCE can be observed through three kinds of measurements, charge state of transmitted ions, convoy electrons and de-excitation X-rays. However, electron capture process, which is important in low energy regions, tends to obscure information on the initial charge state due to RCE. The advantages of using relativistic heavy ions for the RCE measurement are enumerated as follows.

1) Charge exchange processes are not so frequent, and the charge state of transmitted ions keep information on the RCE occurred in a crystal throughout the passage.
2) A thick crystal (several 10 μm) such as a totally depleted silicon detector (SSD) can be adopted as a target, which allows to study an impact parameter dependent RCE by measurements of the energy deposition of the channeled ion.
3) The first order RCE condition, which has the largest transition amplitude in most cases, can be realized.

In the present case, an ion path length per Rabi oscillation of coherent processes is nearly equal to a mean-free-path for ionization from $n = 2$ states. An ion path length per channeling oscillation is also comparable to the above two lengths. The crystal field for the channeled ion is a function of the ion position measured from the channel center. Accordingly, the energy eigenvalues and wave functions of the bound electron in the excited states vary at every moment. That is to say, the energy eigenvalue and the wave function of the bound electron change within mean-free-paths for incoherent ionization or coherent excitation. The purpose of this thesis is to obtain clear resonance profiles for the charge state, de-excitation X-rays and convoy electrons with 390 MeV/u Ar^{17+} ions, and is to study the atomic process of channeled ions under the RCE condition through the obtained three kinds of profiles.

In Sec.2.1, several key concepts on the ion-solid interaction related to the present experiment, such as stopping power and energy straggling, are introduced. The channeling effect and related phenomena are explained in Sec.2.2. Interpretations on the RCE, which is the main subject of the present investigation, are given in Sec.2.3. Results of the channeling experiments with 290 MeV/u C^{6+} ions and 390 MeV/u Ar^{17+} ions are reported in Chap.3. Energy depositions of the ions for random incidence and several channeling conditions were measured. A Monte Carlo simulation for the energy deposition was also performed, and the results were compared with the measured energy depositions. Results of the RCE experiment with 390 MeV/u Ar^{17+} ions are reported in Chap.4. Impact parameter dependent RCE phenomena were observed adopting an SSD as a target crystal through measurements of the charge state distribution of the transmitted ions. Resonance profiles for convoy electrons and de-excitation X-rays were also obtained. The difference between the resonance profiles for the charge state and de-excitation X-rays reflects natures of $n = 2$ states in the crystal field. Finally, a Monte Carlo simulation for the atomic processes of the channeled ion under the RCE condition was carried out, and the result supports discussions about experimentally obtained RCE profiles.

2. Theoretical

2.1. Interaction between ion and solid

2.1.1. Stopping power

When an ion is injected into a material, the ion loses its kinetic energy *via* collisions with the target atom. The energy loss per unit length is called "stopping power". The stopping power is related to the energy loss through

$$\Delta E = \int_0^{z_0} S(E)dz\,, \tag{2.1}$$

where ΔE is an energy loss of the ion through the target with the thickness z_0, and $S(E)$ is the stopping power for the ion with energy E, which is also a function of the path length z. In the case that the energy loss is much smaller than the incident energy, the stopping power can be written as

$$S = \Delta E / z_0\,. \tag{2.2}$$

The stopping power can be divided into two parts, "nuclear stopping power" and "electronic stopping power", which are originated from collisions with the target nuclei and the electrons, respectively. When the ion velocity is much lower than the average velocity of the target electrons, the nuclear stopping power is dominant. For the other velocity region, the contribution from the nuclear collision is negligibly small, and the electronic stopping power becomes dominant (see Fig.2.1).

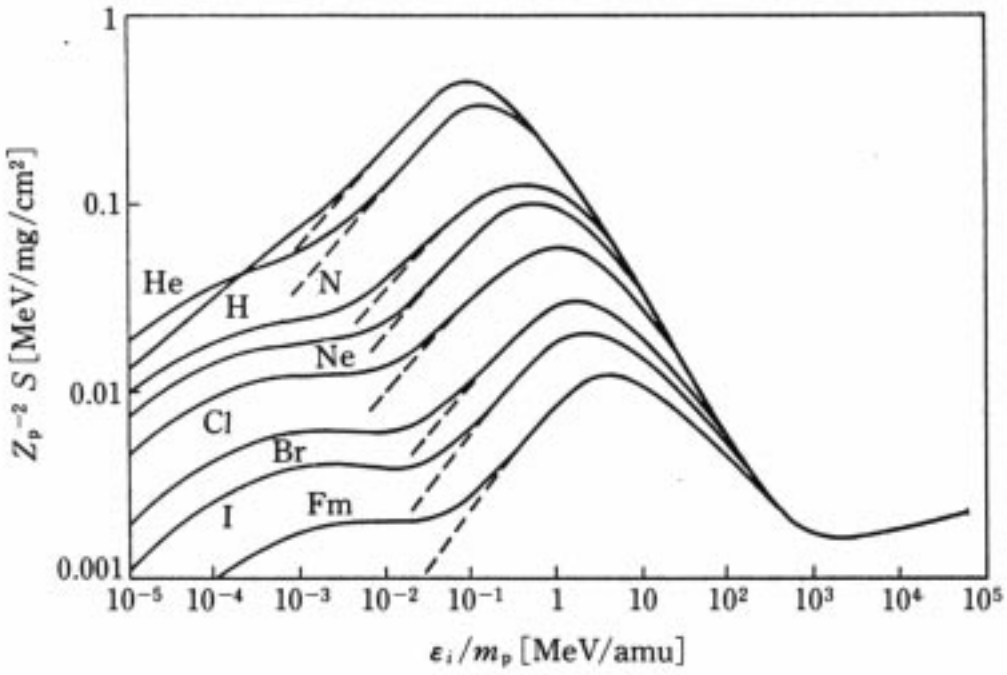

Fig.2.1 Electronic and nuclear stopping powers for several ions in Al target. Dotted lines indicate the electronic stopping power [22].

a. Bethe's formula

The electronic stopping power formula for high energy ions was given by Bethe [23]. He employed the first Born approximation to obtain the collision cross section. The differential cross section for the collision between a projectile ion and a target atom is given by

$$d\sigma_{\mathrm{FB}} = \frac{2\pi Z_1^2 e^4}{m\upsilon^2}\frac{\left|F_{n0}(\boldsymbol{K})\right|^2}{Q^2}dQ, \tag{2.3}$$

where Z_1 is the atomic number of the projectile, e and m are the charge and mass of electron, respectively, υ is the ion velocity, $\hbar\boldsymbol{K}$ is a momentum transfer from the ion to the target atom. The variable, Q, which has the same dimension as energy, and is related to the momentum transfer through

$$Q = \hbar^2 K^2/2m, \tag{2.4}$$

where $\hbar$ is the Planck's constant divided by 2π. For large-Q region, Q corresponds to the energy transfer from the ion to the target. $F_{\mathrm{n0}}(\boldsymbol{K})$ is a matrix element for the transition of the target atom from the ground state to the n-th excited state, which is given by

$$F_{n0}(\boldsymbol{K}) = \left\langle n\left|\sum_j \exp(i\boldsymbol{K}\cdot\boldsymbol{r}_j)\right|0\right\rangle, \tag{2.5}$$

where $\boldsymbol{r}_{\mathrm{j}}$ is a position of the j-th target electron. The factor, $2\pi Z_1^2 e^4/m\upsilon^2 Q^2$, in Eq.(2.3) is originated in the two body collision between the projectile and the free electron. On the other hand, $F_{\mathrm{n0}}(\boldsymbol{K})$ expresses that the electron is bound by the target nucleus. The maximum and the minimum Q are kinematically determined as

$$Q_{\max} = 2m\upsilon^2, \quad Q_{\min} = (E_{\mathrm{n}} - E_0)^2/2m\upsilon^2, \tag{2.6}$$

respectively. Using Eq.(2.3), the stopping power is written as

$$S = N\sum_n (E_n - E_0)\int_{Q_{\min}}^{Q_{\max}} \frac{2\pi Z_1^2 e^4}{m\upsilon^2}\frac{\left|F_{n0}(\boldsymbol{K})\right|^2}{Q^2}dQ, \tag{2.7}$$

where N is the atomic density of the target. To proceed with the calculation of Eq.(2.7), the integral is divided into two parts, *i.e.*, $Q_{\min} < Q < Q_0$ and $Q_0 < Q < Q_{\max}$, where

$$Q_0 = \frac{\hbar^2 K_0^2}{2m} \sim \frac{\hbar^2}{2mr_0^2}, \tag{2.8}$$

and a value larger than the mean orbital radius of the target electron is selected as the value of r_0.

For $Q < Q_0$, *i.e.*, the distant collision, the dipole approximation, $\exp(i\boldsymbol{K}\cdot\boldsymbol{r}) \sim 1 + i\boldsymbol{K}\cdot\boldsymbol{r}$, can be applied. The contribution to the stopping power from the region of $Q_{\min}<Q<Q_0$ is given by

$$S_{Q<Q_0} = N\sum_n (E_n - E_0)\int_{Q_{\min}}^{Q_0} \frac{4\pi Z_1^2 e^4}{\hbar^2\upsilon^2}\left|\left\langle n\left|\sum_j \boldsymbol{r}_j\right|0\right\rangle\right|^2 \frac{dQ}{Q}, \tag{2.9}$$

$$= \frac{2\pi N Z_1^2 Z_2 e^4}{m\upsilon^2}\ln\frac{2m\upsilon^2 Q_0}{I^2}, \tag{2.10}$$

where Z_2 is the atomic number of the target, I is the mean ionization energy, which is defined by

$$\ln I = \left(\frac{2m}{\hbar^2 Z_2} \right) \sum_n \left| \langle n | \sum_j \boldsymbol{r}_j | 0 \rangle \right|^2 (E_n - E_0) \ln(E_n - E_0) . \tag{2.11}$$

Here, the sum rule for the dipole oscillator strength is adopted for derivation of Eq.(2.10) from Eq.(2.9).

On the other hand, for $Q_0 < Q < Q_{\max}$, *i.e.* the close collision, the contribution to the stopping power from this range is calculated to be

$$S_{Q>Q_0} = N \int_{Q_0}^{Q_{\max}} \frac{2\pi Z_1^2 e^4}{m\upsilon^2} \frac{dQ}{Q} \sum_n (E_n - E_0) \left| \langle n | \sum_j \exp(i\boldsymbol{k} \cdot \boldsymbol{r}_j) | 0 \rangle \right|^2 , \tag{2.12}$$

$$= \frac{2\pi N Z_1^2 Z_2 e^4}{m\upsilon^2} \ln \frac{2m\upsilon^2}{Q_0} , \tag{2.13}$$

using the Thomas-Reiche-Khun's sum rule. Summing Eq.(2.10) and Eq.(2.13), the stopping power, S, is derived as

$$S = \frac{4\pi N Z_1^2 Z_2 e^4}{m\upsilon^2} \ln \frac{2m\upsilon^2}{I} . \tag{2.14}$$

The value, Q_0, introduced in this calculation is canceled in the sum. Eq.(2.14) is called "non-relativistic Bethe's formula".

In the case of electron incidence, the two-body collision between electrons is adopted for the close collision. The value of $Q_{\max}$ corresponding to the maximum energy transfer is given by $Q_{\max} = m\upsilon^2/2$. As a result, the stopping power for electron is given by

$$S = \frac{4\pi N Z_2 e^4}{m\upsilon^2} \ln \frac{m\upsilon^2}{I} . \tag{2.15}$$

For relativistic ions, the Bethe's formula, Eq(2.14), is extended to

$$S = \frac{4\pi N Z_1^2 Z_2 e^4}{m\upsilon^2} L_0 , \tag{2.16}$$

where $L_0 = \ln \frac{2m\upsilon^2\gamma^2}{I} - \beta^2$, $\beta = \upsilon/c$ and $\gamma = 1/\sqrt{1-\beta^2}$ [24,25]. A derivation of the relativistic Bethe's formula is given in Appendix1. Contributions from the distant and the close collisions, Eqs.(2.10) and (2.13), are modified to

$$S_{Q<Q_0} = \frac{2\pi N Z_1^2 Z_2 e^4}{m\upsilon^2} \left\{ \ln \frac{2m\upsilon^2 Q_0 \gamma^2}{I^2} - \beta^2 \right\} \tag{2.17}$$

and

$$S_{Q>Q_0} = \frac{2\pi N Z_1^2 Z_2 e^4}{m\upsilon^2} \left(\ln \frac{2m\upsilon^2\gamma^2}{Q_0} - \beta^2 \right), \tag{2.18}$$

respectively. It is worth to note that the relativistic correction term of $\ln\gamma^2 - \beta^2$ in Eq.(2.16) comes from both the distant and the close collisions, and these contributions are equal.

b. Bloch correction

The Bethe's formula is known to reproduce experimental results for light ions with high velocities which satisfy $Z_1 e^2/\hbar\upsilon << 1$. For $Z_1 e^2/\hbar\upsilon >> 1$, the Bohr's classical formula [26] shows a good agreement with experimental results. Bloch indicated that

the exact scattering amplitude (but non-relativistic) should be adopted for collisions with small impact parameter, and derived a correction term

$$\Delta L_{\mathrm{Bloch}} = \psi(1) - \mathrm{Re}\,\psi(1 + iZ_1\alpha/\beta) \tag{2.19}$$

to bridge the gap between the Bethe's quantum mechanical and Bohr's classical formulas. Here, ψ is the digamma function, α is the fine structure constant (~1/137). This term is mainly originated in the close collision with small momentum transfer, *i.e.* with small scattering angle [27], which is important for low velocity ions. For $Z_1 e^2/\hbar v \ll 1$, $\Delta L_{\mathrm{Bloch}}$ is approximated as

$$\Delta L_{\mathrm{Bloch}} \cong -1.202\left(Z_1\alpha/\beta\right)^2, \tag{2.20}$$

which is called "Z_1^4 correction term".

c. Barkas effect

Barkas *et al.* discovered that the range of positively charged pion is shorter than that of negatively charged pion [28]. The effect that the stopping power depends on the sign of Z_1 is called "Barkas effect". This can be explained by the polarization of the target atom. For negatively charged ions, target electrons are repelled from the projectile ion, and the collision probability is reduced. As a result, the energy loss of negatively charged ion becomes smaller than that of positively charged ion. Several theoretical formulas for Z_1^3 correction term were classically derived [29,30]. A simple empirical formula of the correction term, $\Delta L_{\mathrm{Barkas}}$, for $1 < v/Z_2^{1/2} v_{\mathrm{B}} < 10$ is given by

$$\Delta L_{\mathrm{Barkas}} \sim \left[\frac{0.95 - 0.28\ln\left[(v/Z_2^{1/2} v_{\mathrm{B}}) + 2\right]}{Z_2^{1/2}(v/Z_2^{1/2} v_{\mathrm{B}})^2}\right] Z_1 L_0, \tag{2.21}$$

where v_{B} is the Bohr velocity [31]. For ions with the velocity much higher than that of the target electron, this effect is not important.

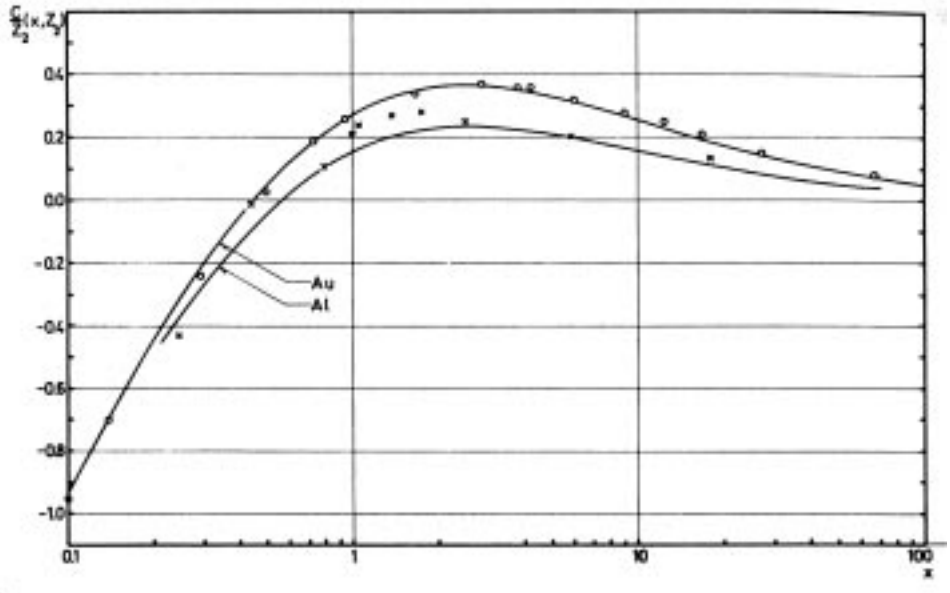

Fig.2.2 Shell corrections for Al and Au targets as a function of x ($= v^2/v_{\mathrm{B}}^2 Z_2$) [33].

d. Shell correction

The Born approximation gets less reliable as the binding energy of the electron in question is larger. Correction terms to take into account the binding effect have been proposed, which is

$$C = C_K + C_L + C_M \cdots, \tag{2.22}$$

where C_K, C_L, C_M $\cdots$ are the contributions from K, L, M, $\cdots$ shells to the correction, respectively. The values of C_K, C_L, C_M $\cdots$ were given using several theories [32,33]. Shell corrections for Ai and Au targets as a function of x ($= v^2/v_B^2 Z_2$) are shown in Fig.2.2.

e. Mott correction

For high-Z ions with relativistic energy, the first Born approximation with relativistic correction is no longer applicable. As for the close collision, the exact relativistic two body scattering cross section, the Mott cross section [34], should be adopted instead of the first Born approximation (Eq.(A.14)) [29], which is given by

$$d\sigma_{\text{Mott}} = \lambda\!\!\!^{-2}\left\{q^2(1-\beta^2)|F|^2 \csc^2(\theta/2) + |G|^2 \sec^2(\theta/2)\right\} d\Omega, \tag{2.23}$$

$$F = F_0 + F_1,$$

$$F_0 = \frac{i\Gamma(1-iq)}{2\Gamma(1+iq)} \exp\left[iq \ln \sin^2(\theta/2)\right],$$

$$F_1 = \frac{i}{2} \sum_{k=0}^{\infty} \left[kD_k + (k+1)D_{k+1}\right](-1)^k P_k(\cos\theta),$$

$$G = G_0 + G_1,$$

$$G_0 = -iq \cot^2(\theta/2) F_0,$$

$$G_1 = \frac{i}{2} \sum_{k=0}^{\infty} \left[k^2 D_k - (k+1)^2 D_{k+1}\right](-1)^k P_k(\cos\theta),$$

$$D_k = \frac{e^{-i\pi k}}{k+iq} \frac{\Gamma(k-iq)}{\Gamma(k+iq)} - \frac{e^{-i\pi\rho_k}}{\rho_k + iq} \frac{\Gamma(\rho_k - iq)}{\Gamma(\rho_k + iq)},$$

$$\rho_k^2 = k^2 - (\beta q)^2,$$

where $\lambda\!\!\!^{-}$ is the de Broglie wave length of the electron divided by 2π, Γ is the gamma function, P_k is the Legendre polynomial of order k, and $q = Z_1 e^2/\hbar v$, is the Sommerfeld parameter. Lindhard and Sørensen also derived the relativistic stopping power formula for heavy ions using a transport cross section employing a partial wave expansion method, and indicated that the deviation from the Bethe's formula converges to the Bloch correction in the non-relativistic limit [35]. Expanding D_k in Eq.(2.22) to the first order of q, we obtain

$$d\sigma_{\text{SB}} = \frac{Z_1^2 e^4}{4m^2 v^4 \gamma^2 \sin^4(\theta/2)} \left[1 - \beta^2 \sin^2(\theta/2) + \pi Z_1 \alpha\beta \sin(\theta/2)(1 - \sin(\theta/2))\right] d\Omega. \tag{2.24}$$

Using the relation between the energy transfer, T, and the scattering angle θ,

$$T = 2mv^2\gamma^2 \sin^2(\theta/2) = T_{\max} \sin^2(\theta/2), \tag{2.25}$$

Eq.(2.24) is transformed to

$$d\sigma_{\mathrm{SB}} = \frac{2\pi Z_1^2 e^4}{m\upsilon^2 T^2}\left\{1-\beta^2\frac{T}{T_{\max}}+\pi Z_1\alpha\beta\left(\frac{T}{T_{\max}}\right)^{1/2}\left[1-\left(\frac{T}{T_{\max}}\right)^{1/2}\right]\right\}dT\,. \tag{2.26}$$

Eq.(2.26) is identical to the cross section derived with the second Born approximation. Adopting Eq.(2.26) as the collision cross section, the close collision part of the stopping power is given by,

$$S_{Q>Q_0} = NZ_2\int_{Q_0}^{Q_{\max}} T d\sigma_{\mathrm{SB}}\,, \tag{2.27}$$

$$= \frac{2\pi NZ_1^2 Z_2 e^4}{m\upsilon^2}\left[\ln\frac{Q_{\max}}{Q_0}-\beta^2+\pi Z_1\alpha\beta\right]. \tag{2.28}$$

The first two terms of Eq.(2.28) are equal to the close collision part of the relativistic Bethe's formula, and the deviation from the relativistic Bethe's formula,

$$\Delta L_{\mathrm{Mott}} = \frac{\pi Z_1\alpha\beta}{2}, \tag{2.29}$$

is called the "linear Mott correction term". The second Born and the exact Mott differential cross sections divided by the first Born result are shown in Fig.2.3. For Z_1 = 18 with the energy of 390 MeV/u, the second Born calculation is seen to be a good approximation, however it deviates considerably from the exact Mott result for Z_1 = 82. Experimentally, stopping powers were measured for O, Ar, Kr and Xe in the energy range from 700 to 1000 MeV/u, and significant deviations from the relativistic Bethe's formula for high-Z ions were observed (see Fig.2.4) [36].

f. Density effect

At very high energy region, a screening effect by target electrons becomes important, and the energy transfer from the ion to an electron is less effective for distant collisions. This effect depends on the target density, and is called "density effect". Sternheimer *et al*. calculated the density effect, $\delta(\beta)$, for various targets, and derived a simple formula, which is

$$\delta(X) = 4.6052X + a(X_1 - X)^m + b \quad (X_0 < X < X_1), \tag{2.30}$$

$$\delta(X) = 4.6052X + b \quad (X > X_1), \tag{2.31}$$

where $X = \log_{10}(\beta\gamma)$, X_0, X_1, a, m and b are parameters which depend on a target [37].

In summary, the relativistic Bethe's formula with several correction terms is written as

$$S = \frac{4\pi NZ_1^2 Z_2 e^4}{m\upsilon^2}\left[L_0 + \Delta L_{\mathrm{Bloch}} + \Delta\,\mathrm{L}_{\mathrm{Barkas}} + \Delta L_{\mathrm{Mott}} - \frac{C}{Z_2} - \frac{\delta(\beta)}{2}\right]. \tag{2.32}$$

A contribution of ΔL_{Mott} is ~1.8 percent of L_0 for 390 MeV/u Ar ion in Si traget, and those of the other correction terms, $\Delta L_{\mathrm{Bloch}}$, $\Delta L_{\mathrm{Barlas}}$, C/Z_2, and $\delta(\beta)/2$ are ~0.5, ~0.3, ~0.3, and ~0.4 percent of L_0, and these four terms are neglected in the present thesis.

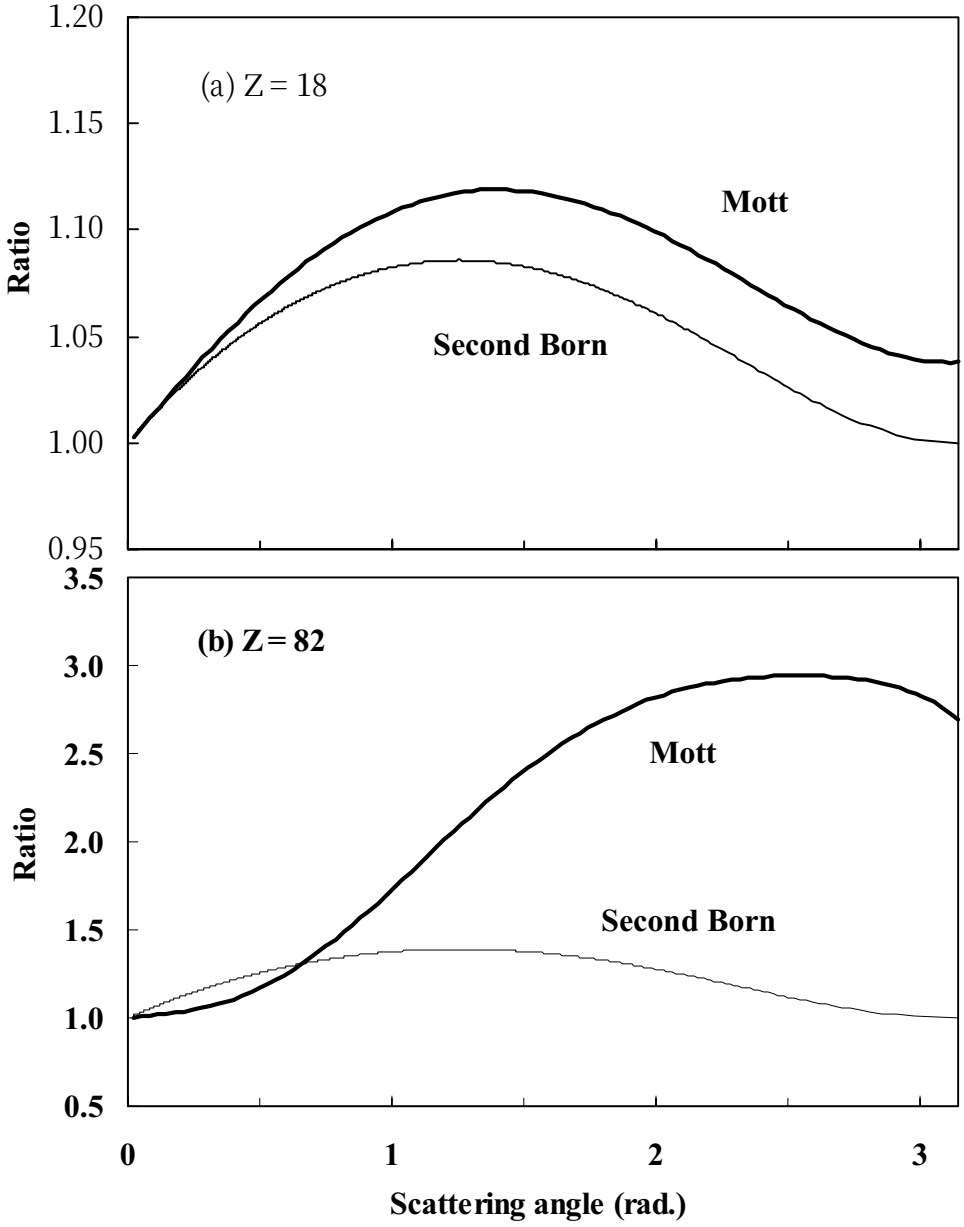

Fig.2.3 Comparison between the exact Mott differential cross section and the result with the second Born approximation. The ordinate is the ratio to the result with the first Born approximation.

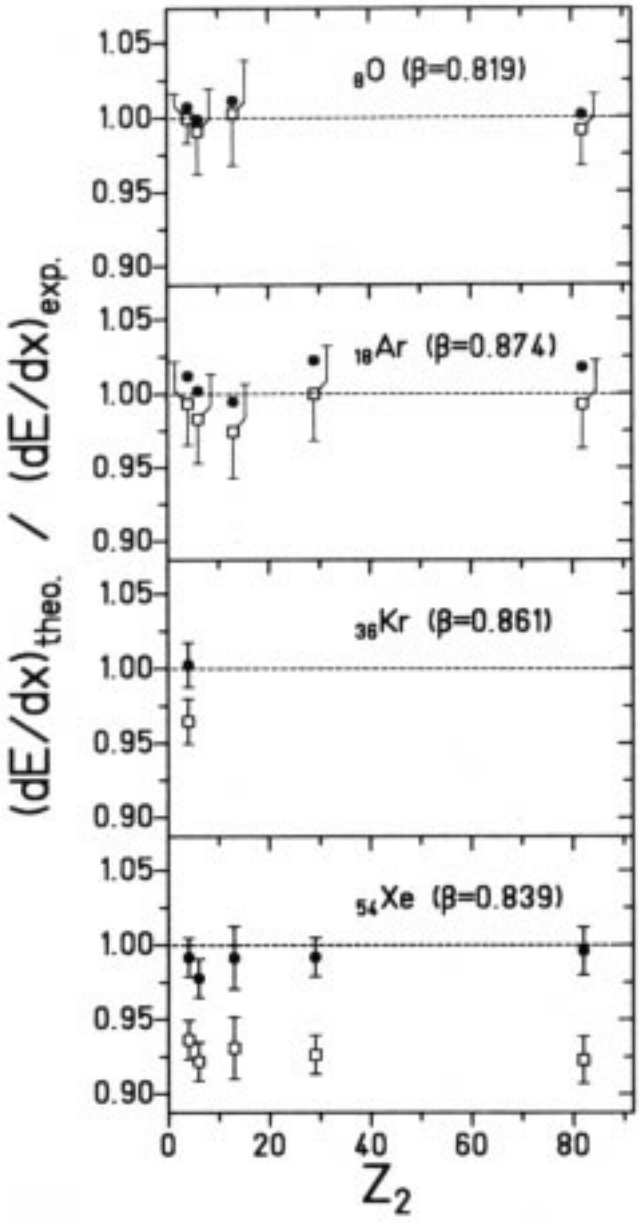

Fig.2.4 Ratio of calculated and measured stopping powers for several projectile-target combinations. The open squares and the full circles are the calculations by the Bethe's formula and that with the Mott and Bloch corrections [36].

2.1.2. Energy straggling

a. Gaussian distribution

An ion penetrating a target looses its kinetic energy *via* collisions with the target atoms, and the energy loss fluctuates statistically around the average value. This fluctuation of energy loss is called "energy straggling". For a thick target, which satisfies

$$\kappa = \frac{\xi}{T_{\max}} >> 1, \tag{2.33}$$

where

$$\xi = \frac{2\pi N Z_1^2 Z_2 e^4 z_0}{m v^2}. \tag{2.34}$$

The energy fluctuation mainly originates from a large number of collisions with small energy transfer, because the collision with large energy transfer is infrequent. In this case, the energy loss distribution becomes the Gaussian shape. Bohr calculated the energy straggling, $\Delta\varepsilon$, assuming that target electrons are free, and derived a formula,

$$\Delta\varepsilon^2 = N z_0 \int_{T_0}^{T_{\max}} T^2 d\sigma, \tag{2.35}$$

$$= 4\pi N Z_1^2 Z_2 e^4 z_0, \tag{2.36}$$

which is called Bohr's formula, where T_0 is the minimum energy transfer in the case that the binding effect of target electrons can be neglected, and the Rutherford differential cross section is assumed as the collision cross section, $d\sigma$. It is noted that the energy straggling is independent of the projectile energy, and is proportional to the square root of the target thickness. Adopting the relativistic collision cross section with the first Born approximation (Eq.(A.14)), Bohr's formula is extended to

$$\Delta\varepsilon^2 = 4\pi N Z_1^2 Z_2 e^4 z_0 \frac{1-\beta^2/2}{1-\beta^2}. \tag{2.37}$$

Fano took the binding effect of target electrons into account [25], and the result is given by,

$$\Delta\varepsilon^2 = 4\pi N Z_1^2 Z_2 e^4 z_0 \left(\frac{1-\beta^2/2}{1-\beta^2} + \frac{2}{3} \frac{\left\langle \left| \sum_j \boldsymbol{v}_j \right|^2 \right\rangle_0}{Z_2 v^2} \ln \frac{2mv^2}{I_1} \right), \tag{2.38}$$

where $\langle\ \rangle_0$ indicates the mean value in the ground state. When the ion velocity is higher, the second term in Eq.(2.38) is less important, and Eq.(2.38) converges to the relativistic Borhr's formula.

For high-Z ions with relativistic energy, the exact Mott cross section should be adopted, and Eq.(2.35) is modified to

$$\Delta\varepsilon^2 = N z_0 \int_{T_0}^{T_{\max}} T^2 d\sigma_{\text{Mott}}. \tag{2.39}$$

Scheidenberger *et al*. measured the energy straggling for O, Xe, Au and U ions in the energy range from 700 to 1000 MeV/u [38]. Calculations with Eq.(2.39) reproduced the experimental results much better than the relativistic Bohr's formula (see Fig.2.5).

Under the present experimental conditions, which are 290 MeV/u C ion and 390 MeV/u Ar ion, the relativistic Bohr's formula gives a good agreement with the

experimental result, and is adopted in this thesis.

b. Landau distribution

In the case of the thin target, which satisfies,

$$\kappa << 1, \tag{2.40}$$

the maximum energy transfer, T_{max}, is larger than the average energy loss, and a small number of collisions with large energy transfer has a significant effect for the energy fluctuation, consequently, the energy loss distribution has a tail to the higher energy side. The energy loss distribution for $\kappa << 1$ was given by

$$f_L(z_0, \Delta E) = \frac{1}{\pi\xi}\int_0^\infty \exp(-\pi t/2)\cos(t\ln t + \lambda t)dt, \tag{2.41}$$

which is called "Landau distribution", where

$$\lambda = (\Delta E - \overline{\Delta E})/\xi - 1 + \gamma_E - \ln\kappa - \beta^2, \tag{2.42}$$

and $\gamma_E = 0.577\cdots$ is the Euler's constant [39,40].

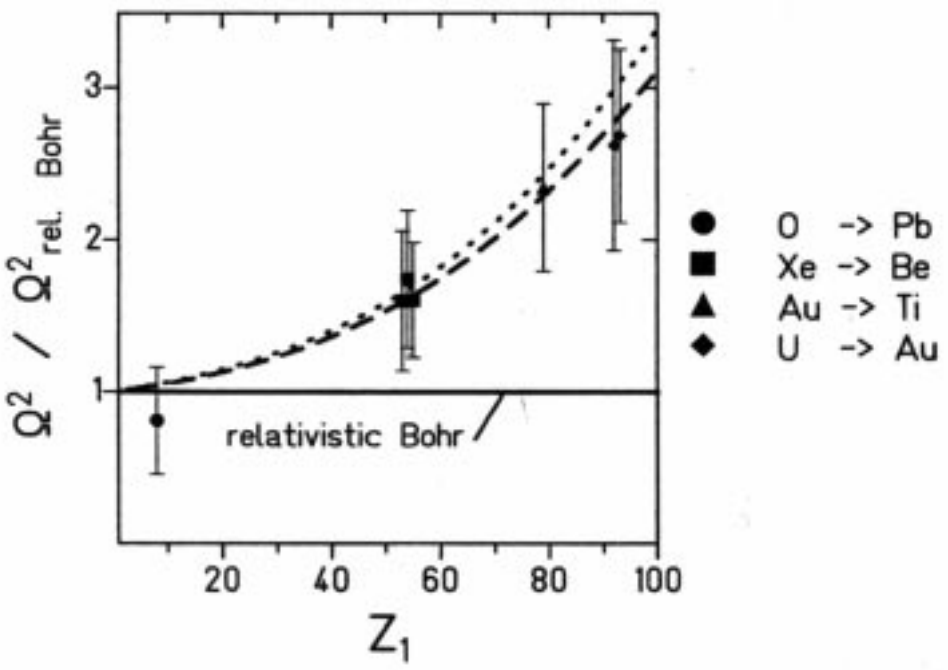

Fig.2.5 Ratio of measured energy straggling to the theoretical predictions of the relativistic Bohr's formula for several projectile-target combinations. The dashed and dotted lines are the results with the Mott cross section for β = 0.81 and 0.87, respectively [38].

2.1.3. Angular straggling

Ions transmitted through a material have finite angular spread due to multiple elastic collisions with the target nuclei, which is called "angular straggling". Collisions with target electrons scarcely contribute to the angular straggling because the mass of electron is much smaller than that of the ion. The mean square angle for single scattering is defined by

$$\left\langle \theta^2 \right\rangle = \int_{\theta_{\min}}^{\theta_{\max}} \theta^2 \frac{d\sigma}{d\Omega} d\Omega \Big/ \int_{\theta_{\min}}^{\theta_{\max}} \frac{d\sigma}{d\Omega} d\Omega \,. \tag{2.43}$$

where $\theta_{\max}$ and $\theta_{\min}$ are the maximum and the minimum scattering angles, which are determined from the minimum and maximum impact parameters comparable to radii of target nucleus and atom, respectively. Considering the scattering of a particle (mass M_1, momentum p and charge Z_1e) with target atom (mass M_2 and charge Z_2e), the differential cross section, $d\sigma/d\Omega$, is given by,

$$\frac{d\sigma}{d\Omega} = \frac{Z_1^2 Z_2^2 e^4}{4p^2 v^2 \sin^4(\theta/2)} \frac{\left[\cos\theta + \left\{1-(M_1/M_2)^2 \sin^2\theta\right\}^{1/2}\right]^2}{\left[1-(M_1/M_2)^2 \sin^2\theta\right]^{1/2}} \,. \tag{2.44}$$

Further considering that the small angle scattering is dominant, *i.e.*, $\sin\theta \sim \theta << 1$, Eq.(2.44) is written as

$$\frac{d\sigma}{d\Omega} \sim \frac{4Z_1^2 Z_2^2 e^4}{p^2 v^2 \theta^4} \,, \tag{2.45}$$

and Eq.(2.43) results in

$$\begin{aligned} \left\langle \theta^2 \right\rangle &= \frac{8\pi Z_1^2 Z_2^2 e^4}{p^2 v^2 \sigma} \int_{\theta_{\min}}^{\theta_{\max}} \frac{d\theta}{\theta} \,, \\ &= \frac{8\pi Z_1^2 Z_2^2 e^4}{p^2 v^2 \sigma} \ln \frac{\theta_{\max}}{\theta_{\min}} \,. \end{aligned} \tag{2.46}$$

The angular straggling of the transmitted ions through the target with the thickness z_0 is obtained as

$$\begin{aligned} \left\langle \Theta^2 \right\rangle &= n\left\langle \theta^2 \right\rangle = N\sigma \cdot z_0 \left\langle \theta^2 \right\rangle \\ &= \frac{8\pi N Z_1^2 Z_2^2 e^4 z_0}{p^2 v^2} \ln \frac{\theta_{\max}}{\theta_{\min}} \,, \end{aligned} \tag{2.47}$$

where n is the mean collision number during the passage through the target.

2.1.4. Range

The incident ion loses its kinetic energy, and finally stops in the target when the target is thick enough. The path length to stop along the incident direction is called "range", which is given by

$$R(E_0) = \int_0^{E_0} \frac{1}{S(E)} \left\langle \cos\theta \right\rangle dE \,, \tag{2.48}$$

where E_0 is the incident energy. Fig.2.6a shows the transmitted fraction of 110 MeV protons through Cu target. The range is experimentally defined as the target thickness where the transmitted fraction is 50 percent.

In the case of electrons, it is difficult to define the range, because the electron

trajectory extremely deviates from a straight line. Fig.2.6b shows the transmitted fraction of electrons with several energies through Al target. The transmitted fraction is a slowly decreasing function of thickness, and has no clear cut length. The thickness obtained by extraporating the curve (dotted line in Fig.2.6b) is often used, which is called "extraporated range". Several empirical formula of the extraporated range are proposed [41,42]. Tanabe *et al.* proposed an analytical formula for 0.3 keV−30 MeV electrons and for targets with $Z_2 = 6 - 92$, which is given by

$$R_{\mathrm{ex}}(E_0) = a_1\left[\frac{\ln(1+a_2E_0)}{a_2} - \frac{a_3E_0}{1+a_4E_0^{a5}}\right]. \tag{2.49}$$

They also gave the inverse relation formula for convenience, which is

$$E_0 = c_1\left[\exp\left\{R_{\mathrm{ex}}\left(c_2 + \frac{c_3}{1+c_4R_{\mathrm{ex}}^{c_5}}\right)\Big/c_1\right\} - 1\right], \tag{2.50}$$

where the parameter a_i and c_i (i=1−5) are simple functions of Z_2 [41].

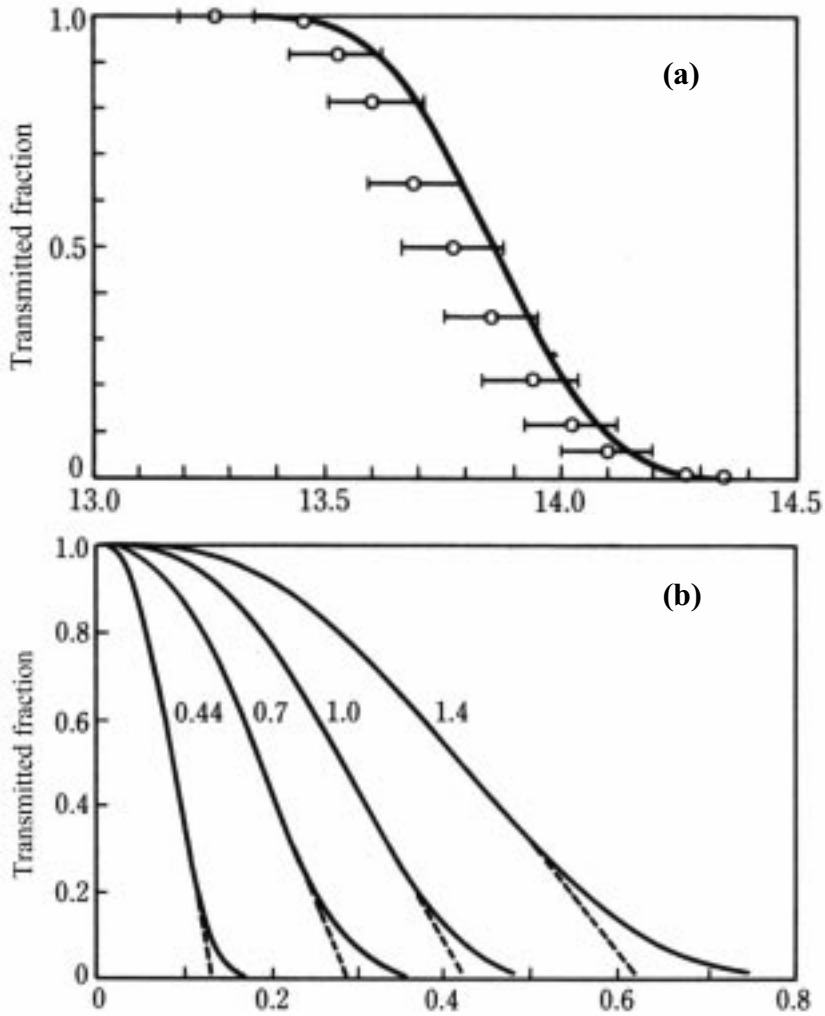

Fig.2.6 Transmitted fraction of (a)110 MeV proton in Cu target, and (b) electrons with several energies in Al target as a function of the target thickness. Numbers in (b) indicate incident electron energy in MeV [43,44].

2.1.5. Electron loss and capture

Ions passing through a target have a possibility of charge exchange, *i.e.*, electron loss and electron capture, due to collisions with the target atoms. At high energies, ionization cross section, σ_i, is approximated as

$$\sigma_i = Z_2\sigma_e + Z_2^2\sigma_p, \tag{2.51}$$

where σ_e and σ_p are the electron and proton impact ionization cross sections, respectively. The first term represents the electron impact ionization (EII) and the second one is the nuclear impact ionization (NII). The values of σ_e and σ_p were calculated using the plane wave Born approximation [45–48]. They were also determined by measurements of the one-electron loss cross section for 405 MeV/u U^{86+} and 100 and 380 MeV/u Au^{52+} in H_2 and He, and can be regarded as $\sigma_e \approx \sigma_p$ [49].

On the other hand, the total electron capture cross section, σ_c, is given by

$$\sigma_c = \sigma_{MEC} + \sigma_{REC}, \tag{2.52}$$

where σ_{MEC} and σ_{REC} are the cross sections for mechanical electron capture (MEC) and radiative electron capture (REC), respectively. A target electron can be transferred to the projectile ion when the momentum of the target electron matches to that of the bound electron of the projectile, *i.e.*,

$$p_t = p_p + mv_p, \tag{2.53}$$

where p_t and p_p are momenta of target electron and bound electron, respectively, and v_p is the projectile velocity. The cross section of MEC was calculated by the Oppenheimer-Brinkman-Kramers (OBK) approximation [50,51]. The REC is the electron capture process which accompanies the photon emission to compensate a momentum gap between the target and the projectile electrons [52]. The REC process is more important than the MEC process for high energy ions [53].

Charge exchange processes modify the stopping power. Kim and Cheng considered the electronic structure of the projectile ions as well as the target atom, and extended the Bethe's stopping power formula for partially stripped ions [54]. In the formula, the projectile charge, Z_1, and the mean ionization energy, I, are replaced as the effective charge, $Z_{eff,}$ and the effective mean ionization energy, I_{eff}, respectively. Cabrera-Trujillo *et al.* gave an analytical stopping power formula, which has two components related to the electronic structures of the projectile and the target atom, with a consideration of the velocity dependent number of bound electrons [55].

The energy straggling is also modified by the charge exchange effect. Sigmund derived an additional term of the energy straggling formula in the presence of charge exchange processes [56].

2.1.6. Convoy electrons

Velocity (energy) spectra of electrons produced by the ion-solid collision have a 'cusp' shaped peak at the ion velocity, and electrons in the peak are called "convoy electrons". The convoy electrons come from processes of electron loss to continuum (ELC) and electron capture to continuum (ECC). Generally, the velocity spectrum for the ELC electrons is nearly symmetric, and that for the ECC electrons is skewed toward the lower velocity side, because the electrons feel the force to the opposite direction to the ion velocity both before and after the collision. When partially stripped (the charge

is lower than the equilibrium charge) ions are used, the ELC process is dominant at high energy region, because σ_i is much larger than σ_c. Experimental studies of convoy electrons were extensively performed so far [57]. The angular distributions of the ELC convoy electrons with 36 MeV/u Ar ions were measured [58], and the results indicated that the transverse velocity of convoy electron increases as the target thickness increases. The cusp shape of the ELC convoy electrons was theoretically studied by Burgdörfer *et al*. [59]. The calculated energy spectra for ELC of He^+ at the acceptance angle for detection, $\theta_0 = 3 \times 10^{-2}$ rad., are shown in Fig.2.7. The cusp shapes of ELC from 2s and $2p_1$ are narrower than that from 1s (Fig.2.7a), because the momentum distribution of 2s and $2p_1$ in the direction of the projectile velocity is sharper than that of 1s. In the case of ELC convoy electrons from $2p_0$ state, the spectrum becomes 'anti-cusp' shape (Fig.2.7b). Experimentally, the cusp shape for hydrogen-like Ar ions with a relativistic energy on C-foil found to be sharper as the increase of the foil thickness from 25 to ~500 μg/cm^2 [60]. This unfamiliar result is due to the increase of the ionization from excited states as the increase of the foil thickness, and has never observed in the experiment for lower energy ions [61]

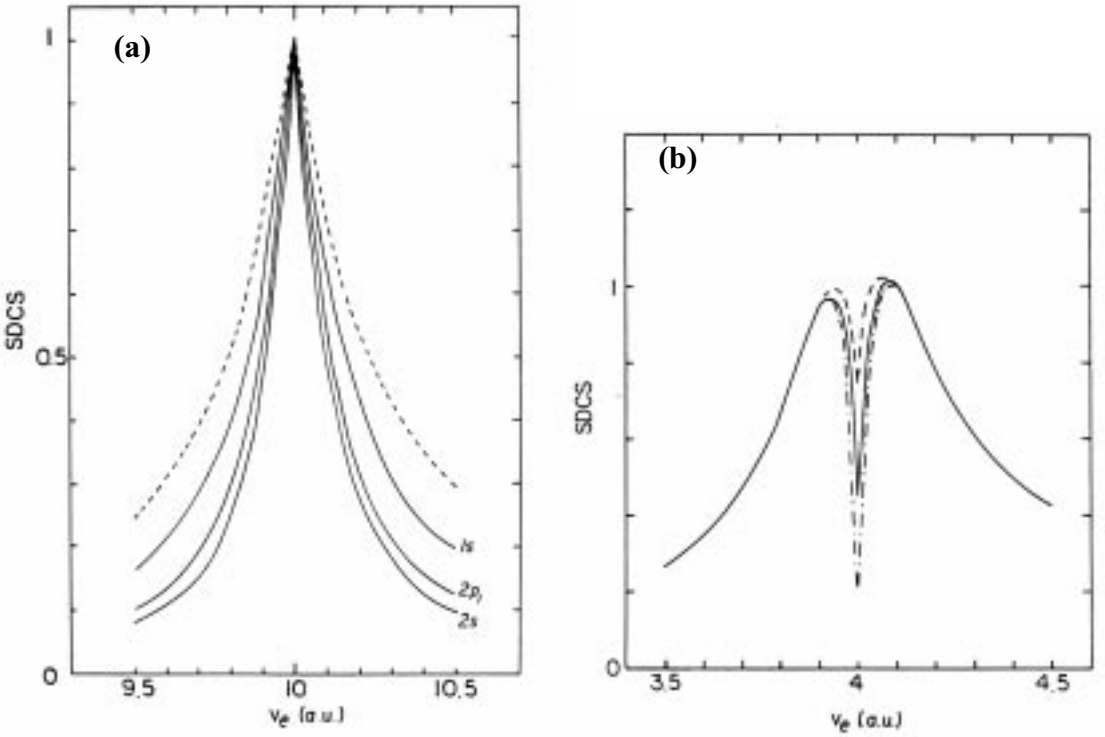

Fig.2.7 (a) Normalized singly differential cross section, $d\sigma/dv$, for ELC of He^+ from 1s, 2s and 2p states on H at the projectile velocity of 10 a.u. and $\theta_0 = 3 \times 10^{-2}$ rad., and (b) $d\sigma/dv$, for ELC of He^+ from $2p_0$ states on H (solid line), He (dashed line) and Ar (dot-dashed line) at the projectile velocity of 4 a.u. and $\theta_0 = 3 \times 10^{-2}$ rad. [59].

2.2. Channeling effect

2.2.1. Axial channeling and planar channeling

When ions are injected into a crystal parallel to the crystal axis or plane, the ions receive only small angle scatterings, and pass through the space where the target nuclei do not exist along the axis (axial channel) or the plane (planar channel) as shown in Fig.2.8. This effect is called "channeling", and was predicted by Stark in 1912. The channeling effect was first observed in 1960. Rol *et al.* reported that the sputtering yield for ion bombardment to a single crystal depends on the crystal orientation [62]. In the same year, Davies *et al.* found abnormally long ranges of heavy ions in polycrystalline aluminum and tungsten [63]. Since then, many experimental and theoretical studies on the channeling effect have been performed [1,2,64].

To describe the motion of channeled ions, the axial and the planar potentials, which are averaged along the axis and the plane, respectively, are useful. The axial potential by a single string is given by

$$U_{\mathrm{a}}^{(\mathrm{s})}(\rho) = \frac{1}{d}\int_0^\infty V(r)dz\,, \tag{2.54}$$

where d is the distance between atoms along the axis, $\boldsymbol{r}$ is the position of an ion from a target nucleus, z is a component of $\boldsymbol{r}$ in the direction of the ion velocity, and $\rho^2 = r^2 - z^2$, and $V(r)$ is an atomic potential at position $\boldsymbol{r}$. The potential for axial channeled ions is expressed as

$$U_{\mathrm{a}}(\boldsymbol{\rho}) = \sum_j U_{\mathrm{a}}^{(\mathrm{s})}(\boldsymbol{\rho} - \boldsymbol{\rho}_j)\,, \tag{2.55}$$

where the sum is taken for all strings surrounding the axial channel.

For the planar channeling case, the planar potential by a single plane is given by

$$U_{\mathrm{p}}^{(\mathrm{s})}(x) = 2\pi N d_{\mathrm{p}}\int_0^\infty V(r)\rho d\rho\,, \tag{2.56}$$

where d_{p} is the inter-planar distance, x is a components of $\boldsymbol{r}$ perpendicular to the channeling plane, and $\rho^2 = r^2 - x^2$. The potential for planar channeled ions is similarly expressed as

$$U_{\mathrm{p}}(x) = \sum_n U_{\mathrm{p}}^{(\mathrm{s})}(x - nd)\,, \tag{2.57}$$

where the sum is taken for all planes.

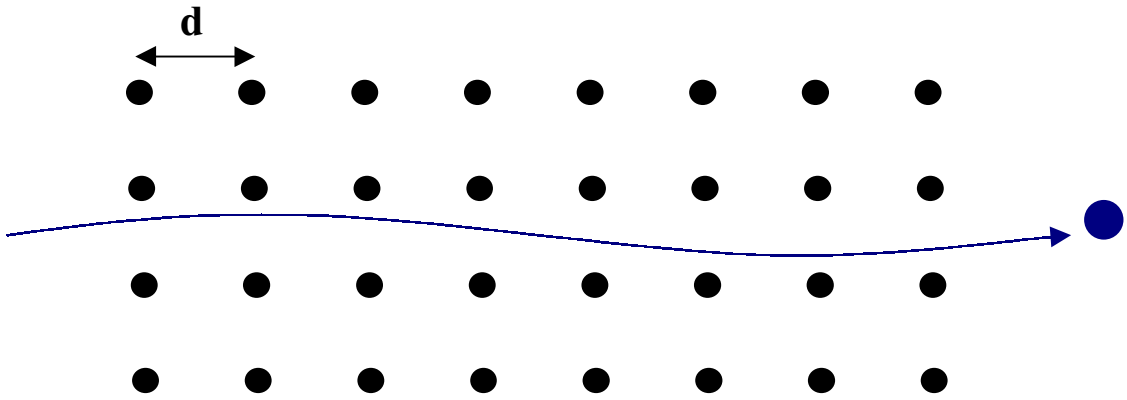

Fig.2.8 Trajectory of channeled particle in a crystal.

The target nuclei are screened by the target electrons, and a screened Coulomb potential should be adopted as the atomic potential. Several different types of screened Coulomb potentials have been proposed, which are explained below.

a. Thomas-Fermi potential

When the number of bound electrons is large, the electrons can be treated as an ensemble of fermions. Assuming that the electrons occupy the momentum space from 0 to p_0, the electron density in the real space is given by

$$n(r) = 2\frac{4\pi p_0^3(r)}{3}\Big/(2\pi\hbar)^3 = \frac{p_0^3(r)}{3\pi^2\hbar^3}, \tag{2.58}$$

where the factor 2 comes from the duality of the spin up and down states. The total energy of the electron,

$$E_0 = \frac{p_0^2(r)}{2m} - e\phi(r), \tag{2.59}$$

must be constant, where $\phi(r)$ is the electrostatic potential. By solving the Poisson equation with Eqs.(2.58) and (2.59), the potential for the ion with the charge, Z_1e, screened by the electrons is derived as

$$V(r) = Z_1 e\phi(r) = \frac{Z_1 Z_2 e^2}{r}\chi(r/a_{\mathrm{TF}}), \tag{2.60}$$

where $\chi(x)$ is called the Thomas-Fermi function, which satisfies

$$\frac{d^2\chi(x)}{dx^2} = \frac{\chi^{3/2}(x)}{x^{1/2}}, \tag{2.61}$$

and $a_{\mathrm{TF}} = 0.885Z_2^{-1/3}a_{\mathrm{B}}$ is called the Thomas-Fermi radius, where a_{B} is the Bohr radius.

b. Molière potential

The Thomas-Fermi function is fitted with a sum of exponential functions,

$$V(r) = \frac{Z_1 Z_2 e^2}{r}\sum_{n=1}^{3}\alpha_n \exp(-\beta_n r/a_{\mathrm{TF}}), \tag{2.62}$$

where α_n = (0.35, 0.55, 0.1), β_n = (0.3, 1.2, 6.0). Eq.(2.62) is called "Molière potential".

c. Lindhard potential

Lindhard also proposed a simple formula approximating the Thomas-Fermi function as $\chi(x) = 1 - x\Big/\sqrt{C^2 + x^2}$, which resulted in

$$V(r) = \frac{Z_1 Z_2 e^2}{r}\left(1 - \frac{r/a_{\mathrm{TF}}}{\sqrt{C^2 + (r/a_{\mathrm{TF}})^2}}\right), \tag{2.63}$$

where C^2 ~3 is a constant. The Lindhard potential is a good approximation of the Thomas-Fermi potential especially around $r = 2a_{\mathrm{TF}}$, and is suitable for describing a channeling motion, because the distance between a channeled ion and a target nucleus is of the order of a_{TF}.

The deviations of the Molière and the Lindhard potentials from the Thomas-Fermi potential are shown in Fig.2.9. The Molière potential agrees with the Tomas-Fermi potential comparatively for wide ranges. In the present calculation, the Molière potential was adopted to evaluate the planar potential, which is given by

$$U_{\mathrm{p}}(x) = 4\pi Z_1 Z_2 e^2 N d_{\mathrm{p}} a_{\mathrm{TF}} \sum_{n=1}^{3} \frac{\alpha_n}{\beta_n} e^{-\frac{\beta_n d_{\mathrm{p}}}{2a_{\mathrm{TF}}}} \cosh\left(\frac{\beta_n x}{a_{\mathrm{TF}}}\right), \tag{2.64}$$

where x is a distance from the channel center. Moreover, considering a fluctuation of the crystal lattice due to the thermal vibration, $U_{\mathrm{p}}(x)$ was modified to

$$U'_{\mathrm{p}}(x) = \frac{1}{\sqrt{2\pi}u_1} \int_{-\infty}^{\infty} e^{-\frac{u^2}{2u_1^2}} U_{\mathrm{p}}(x+u)du\,, \tag{2.65}$$

where u_1 is a one-dimensional amplitude of the thermal lattice vibration. Typical axial and planar potentials are shown in Fig.2.10. The axial potential has a saddle point between neighboring channels, and axial channeled ions have a possibility of moving to a next channel. When a transverse energy of the channeled ion, which is defined by Eq.(2.66), is small enough, the ion travels in a single channel, which is called “hyper channeling”. On the other hand, planar channeled ions always move in a single channel, because a planar potential has no saddle point.

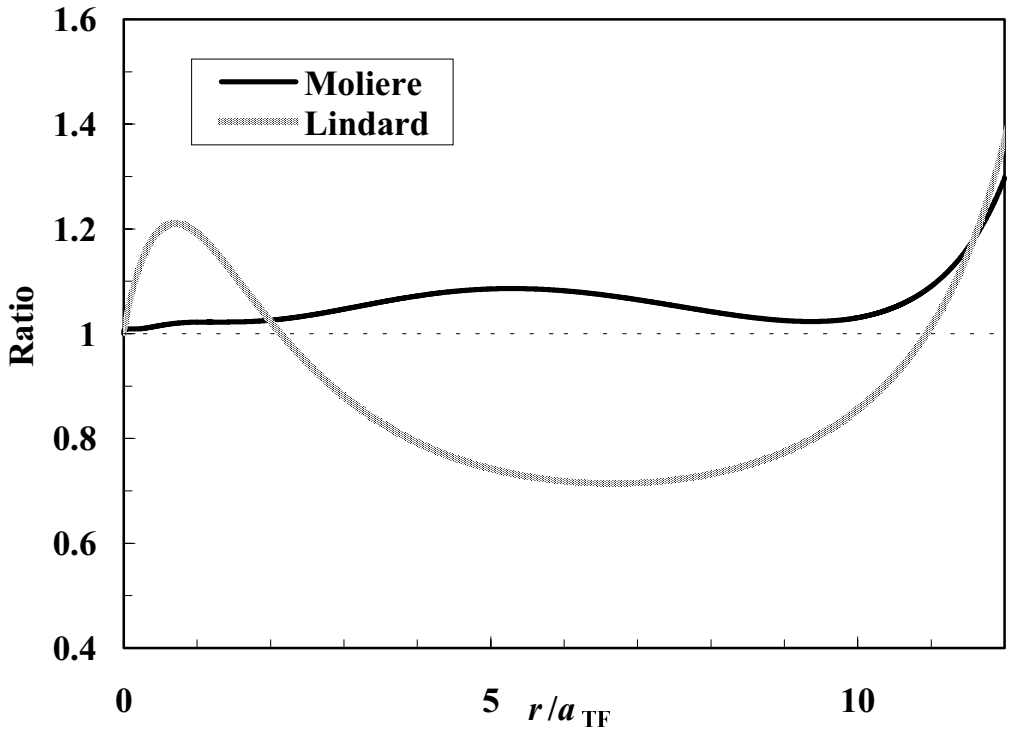

Fig.2.9 Ratios of the Molière and the Lindhard potentials to the Thomas-Fermi potential.

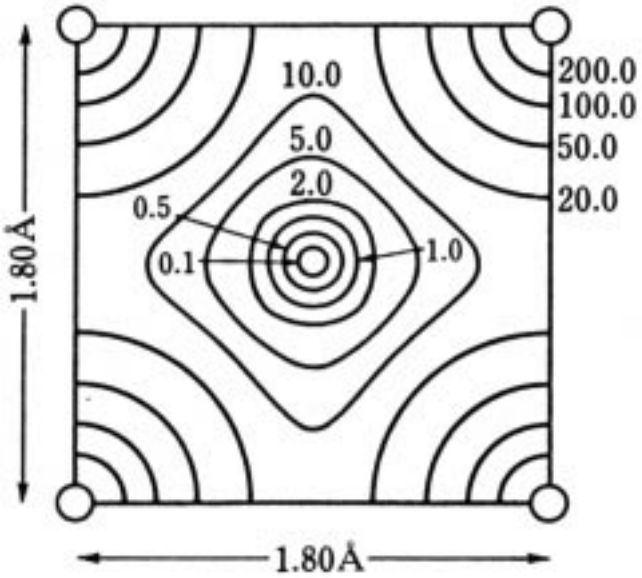

Fig.2.10a Axial potential for He ion in Cu <100> axial channel. Numbers indicate the potential height in eV.

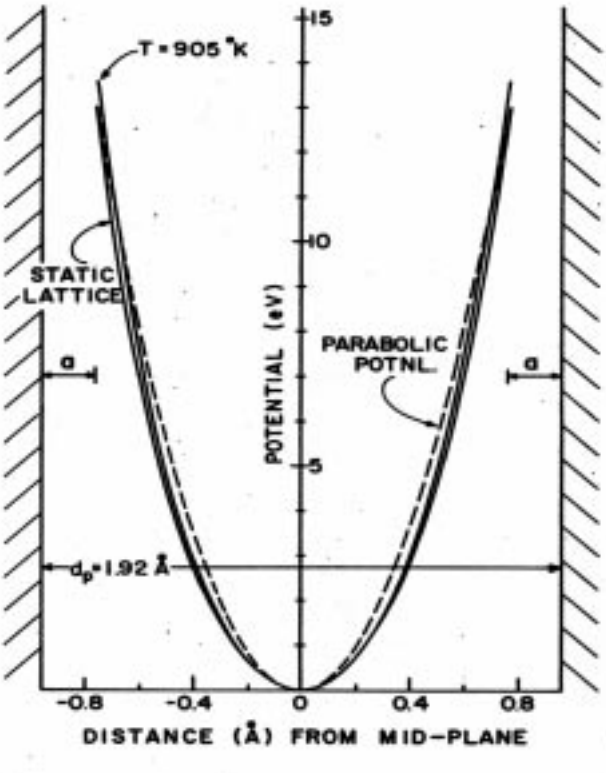

Fig.2.10b Planar potential for proton in Si (110) planar channel. The broken line is a parabolic potential.

2.2.2. Critical angles of channeling

Incident ions can be channeled only when the incident angle from the axis or plane is smaller than a certain angle. The maximum angle for channeling is called the "critical angle". The critical angle is estimated as follows. Considerations of two- and one-dimensional motions perpendicular to the beam direction are necessary for axial and planar channeling cases, respectively. The transverse energies of the ions with energy, E, for axial and planar channeling cases are given by

$$E_\perp = U_a(\rho) + E\sin^2\psi \cong U_a(\rho) + E\psi^2, \tag{2.66}$$

$$E_\perp = U_p(x) + E\sin^2\psi \cong U_p(x) + E\psi^2, \tag{2.67}$$

where ψ is an angle between the ion velocity and the channel axis or plane, and $U_a(\rho)$ and $U_p(x)$ are defined to be 0 at the channel center. Assuming that the ions are injected at the channel center with the critical angle ψ_c, relations

$$E\psi_c^2 = U_a^{(s)}(\rho_{min}), \tag{2.68}$$

$$E\psi_c^2 = U_p^{(s)}(x_{min}), \tag{2.69}$$

are satisfied, because the transverse energy, $E_\perp$, is constant, where ρ_{min} and x_{min} are the closest distances from the channel axis and plane, respectively. Adopting the Lindhard potential, the axial and planar potentials, $U_a^{(s)}(\rho)$ and $U_p^{(s)}(x)$, are given by

$$U_a^{(s)}(\rho) = \frac{1}{d}\int_0^\infty V(r)dz = \frac{Z_1 Z_2 e^2}{d}\ln\left[(Ca_{TF}/\rho)^2 + 1\right], \tag{2.70}$$

$$U_p^{(s)}(x) = 2\pi N d_p \int_0^\infty V(r)\rho d\rho = 2\pi N Z_1 Z_2 e^2 d_p\left[\sqrt{x^2 + C^2 a_{TF}} - x\right], \tag{2.71}$$

respectively. ρ_{min} and x_{min} are considered to be ~a_{TF}, so that Eqs.(2.68) and (2.69) are written as

$$E\psi_c^2 = U_a^{(s)}(\rho_{min}) \sim \frac{2Z_1 Z_2 e^2}{d} \equiv E\psi_1^2, \tag{2.72}$$

$$E\psi_c^2 = U_p^{(s)}(x_{min}) \sim 2\pi Z_1 Z_2 e^2 N d_p a_{TF} \equiv E\psi_p^2, \tag{2.73}$$

Therefore, the critical angle, ψ_c, for axial and planar channelings are represented by ψ_1 and ψ_p, which are obtained as

$$\psi_1 = \sqrt{\frac{2Z_1 Z_2 e^2}{Ed}}, \tag{2.74}$$

$$\psi_p = \sqrt{\frac{2\pi N Z_1 Z_2 e^2 d_p a_{TF}}{E}}. \tag{2.75}$$

For relativistic energy region, Eqs.(2.74) and (2.75) are modified to

$$\psi_1 = \sqrt{\frac{4Z_1 Z_2 e^2}{pvd}}, \tag{2.76}$$

$$\psi_p = \sqrt{\frac{4\pi N Z_1 Z_2 e^2 d_p a_{TF}}{pv}}, \tag{2.77}$$

by replacing E with $pv/2$, where p and v are the momentum and the velocity of the incident ion, respectively.

2.2.3. Stopping power for channeled ion

As explained in Sec.2.1.1, the stopping power can be divided into two components, *i.e.*, those originated from distant and close collisions with target electrons. Under the channeling condition, the probability of the close collision is reduced compared with that for the random incidence, because the channeled ions pass through a space where the local electron density is much lower than the mean electron density. As a result, the stopping power (*i.e.* energy loss) for the channeled ions becomes considerably smaller than that for the random incidence.

Lindhard proposed a simple formula for the stopping power for the channeled ion, which is given by

$$S(\boldsymbol{r}) = S_{\mathrm{r}}\left[(1-\alpha_{\mathrm{c}}) + \alpha_{\mathrm{c}}\frac{n_{\mathrm{e}}(\boldsymbol{r})}{Z_2 N}\right], \tag{2.78}$$

where S_{r} is the stopping power for random incident ions, $n_{\mathrm{e}}(\boldsymbol{r})$ is the local electron density at position $\boldsymbol{r}$, and α_{c} is a parameter between 1/2 and 1 [64]. The first term of Eq.(2.78) expresses the contributions from the distant collision, which is proportional to the mean electron density. The second term corresponds to the contribution from the close collision, which is proportional to the local electron density. The value of α_{c} is determined by the experimental result, and Lindhard argued that α_{c} becomes closer to 1/2 for larger velocity, and Eq.(2.78) results in

$$S_{\mathrm{L}}(\boldsymbol{r}) = S_{\mathrm{r}}\frac{Z_2 N + n_{\mathrm{e}}(\boldsymbol{r})}{2Z_2 N}. \tag{2.79}$$

Eq.(2.79) means that the distant collision part is a half of the total stopping power for random incidence, which is called “equipartition rule” [65]. The equipartition rule was confirmed by experiments on the energy loss of best channeled protons in silicon, while the deviation from Eq.(2.79) was reported as for the energy loss of best channeled protons in germanium [66,67], which are listed on Table2. Appleton *et al.* assumed that only valence electrons contribute to the stopping power of the “best channeled ion”, which passes straight in the channel center. The formula is expressed as

$$S = \frac{4\pi N Z_1^2 e^4}{m\upsilon^2}\left(Z_{\mathrm{val}}\ln\frac{\upsilon}{\upsilon_{\mathrm{F}}} + Z_{\mathrm{loc}}\ln\frac{2m\upsilon\upsilon_{\mathrm{F}}}{\hbar\omega_{\mathrm{p}}}\right), \tag{2.80}$$

where NZ_{val} and NZ_{loc} are the effective electron densities for plasmon and single-particle excitations, respectively, υ_{F} is the Fermi velocity, and ω_{p} is the plasma frequency. They adopted the formula to the case for a 3 MeV proton channeled in a Si (111) plane. The value of Z_{loc}= 3.8 was obtained from the experiment assuming Z_{val} = 4 for Si. [67].

Esbensen and Golovchenko attributed the deviation from Eq.(2.79) to the crystal lattice structure [68]. The stopping power formula as a function of the impact parameter $\boldsymbol{b}$ is given by

$$S(\boldsymbol{b}) = \frac{2\pi N Z_1^2 e^4}{m\upsilon^2}\left[\big(Z_2 + Z(\boldsymbol{b})\big)\ln\frac{2m\upsilon^2}{I} + C(\boldsymbol{b})\right], \tag{2.81}$$

where

$$C(\boldsymbol{b}) = \sum_{\boldsymbol{G}\neq\boldsymbol{0}} e^{i\boldsymbol{G}\cdot\boldsymbol{b}}\rho(\boldsymbol{G})\ln\frac{2mI}{\hbar^2 G^2}, \tag{2.82}$$

$NZ(\boldsymbol{b})$ is the local electron density at position $\boldsymbol{b}$, and $\boldsymbol{G}$ is the reciprocal lattice vector,

and $\rho(\boldsymbol{G})$ is the Fourier transform of the electron density in the target crystal. Eq.(2.81) was extended to the relativistic energy region as

$$S(\boldsymbol{b}) = \frac{2\pi N Z_1^2 e^4}{m\upsilon^2}\left[(Z_2 + Z(\boldsymbol{b}))\left(\ln\frac{2m\upsilon^2\gamma^2}{I} - \beta^2\right) - Z_2\delta + C(\boldsymbol{b})\right], \tag{2.83}$$

where δ is the correction term for the density effect. The formula shows a good agreement for the channeled particles along the <110> axial and the {111}, {110} and {100} planar directions in Si and Ge crystals (see Fig.2.11) [69].

Eq.(2.80) can be adopted only for best channeled ions, because an effect of core electrons becomes important for the stopping power of channeled ions with large oscillation amplitude. Eqs.(2.81) and (2.83) are the formulas for channeled ions with fixed impact parameter, *i.e.*, it is realistically limited for the best channeled ions. The Lindhard formula, Eq.(2.78), is applicable for evaluating the energy loss of channeled ions with various trajectories.

As for the planar channeling, the relation between the stopping power of channeled ions and the oscillation frequency was investigated [70]. A trajectory of the planar channeled ion is different from the sinusoidal curve because of the anharmonicity of the potential. The slope of the planar potential is steeper than the parabolic potential near the channel wall as shown in Fig.2.10b. Accordingly, the stopping power depends not only on the oscillation amplitude but also on the oscillation frequency, and was measured to be proportional to the oscillation frequency [71,72].

Table2 Measured energy loss, $\Delta E_{\{111\}}$, of {111} planar channeled proton with several energies, E_I, and predictions by equipartition rule, ΔE_{equip}, for silicon and germanium targets [67].

Crystal	E_I (MeV)	$\Delta E_{\{111\}}$ (MeV)	ΔE_{equip}(MeV)
Silicon	2.81	0.33	0.35
	4.83	0.22	0.24
	8.58	0.14	0.15
	11.00	0.12	0.12
Germanium	5.00	0.22	0.32
	7.00	0.17	0.26
	9.00	0.15	0.22
	11.00	0.12	0.18

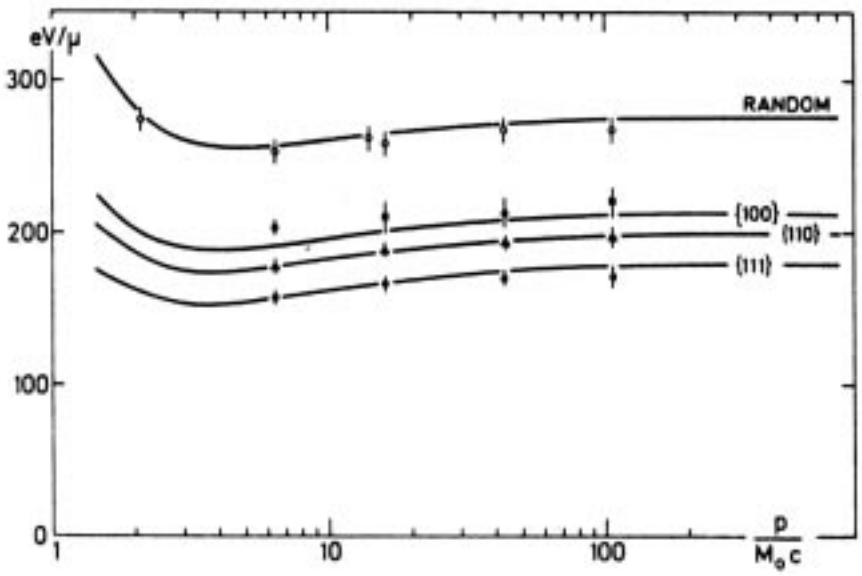

Fig.2.11 Comparison between theory, Eq.(2.83), and experimental results for three planar channelings and random incidence [69]. Stopping power is plotted as a function of $p/M_0c = \beta\gamma$.

2.2.4. Charge state of transmitted ions under channeling condition

Under the channeling condition, the charge exchange processes are also suppressed, and a condition of the "frozen-charge state", which means that the ion maintains the initial charge state throughout the passage, can be easily achieved. Datz *et al.* measured the stopping power of {111} planar channeled ions in Au crystal, which have not changed the charge state throughout the passage. The hydrogen-like and helium-like ions of $Z_1 = 5 - 9$ with the energies of 2 MeV/u were used in their experiment [73].

A charge state distribution of channeled ions transmitted through a crystal is quite different from that for random incidence, because of the impact parameter (transverse energy) dependence of the charge exchange probability. Fig.2.12 shows charge state distributions of 300 MeV/u U^{73+} ions after transmission through 120 μm thick Si crystal, which were measured under <110> axial channeling and random conditions. [74]. For random incidence, the charge state distribution has a peak at $q_{out} = 90$, however, the peak is shifted to $q_{out} \sim 76$ for the <110> axial channeling case, where q_{out} is the exit charge state. A peak at $q_{out} = 90$ under the channeling condition corresponds to non-channeled or de-channeled ions. The broad distribution for the channeling case is due to the transverse energy ($E_\perp$) dependence of q_{out} distribution, *i.e.*, q_{out} for channeled ions with a large oscillation amplitude (large $E_\perp$) becomes to ~90, although that for channeled ions near the channel center (small $E_\perp$) is ~ 73.

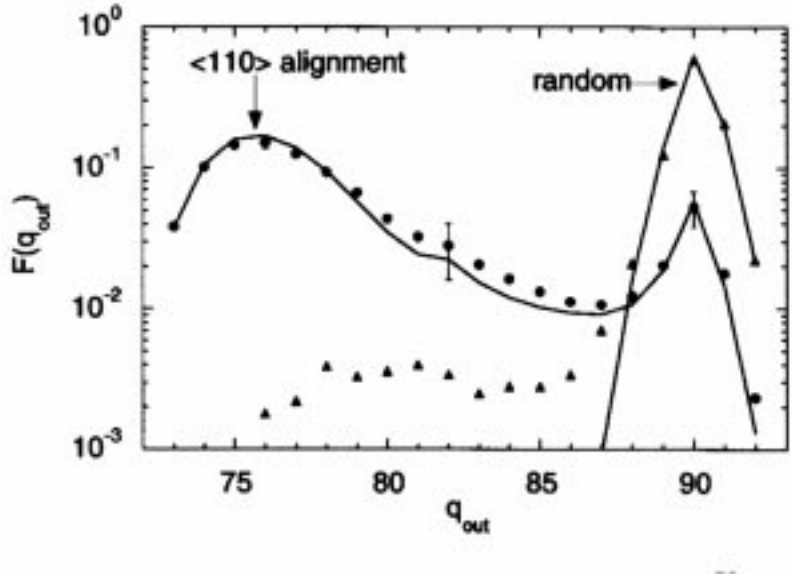

Fig.2.12 Charge state distributions of 300 MeV/u U^{73+} ions transmitted through 120 μm Si crystal. Closed circles and triangles are experimental results, and Solid lines are results of Monte Carlo simulation [74].

2.3. Resonant coherent excitation

2.3.1. Resonant coherent excitation of channeled ion

Channeled ions have a chance to be excited by the oscillating electromagnetic field caused by the periodic crystal potential, when one of the internal energy differences of the ion coincides with the photon energy of the corresponding field frequency. This effect was predicted by Okorokov in 1965 [8], and is called "Okorokov effect" or "resonant coherent excitation (RCE)". The original prediction by Okorokov is the RCE in nuclear levels, but the channeled ions can be coherently excited also in atomic levels. For the atomic RCE, the excited ions have a larger ionization probability compared with the ions in the ground state. The first observation of RCE in atomic levels was achieved with hydrogen-like and helium-like light ions of Z = 5 to 9 through the measurement of the charge state distribution of the transmitted ions [9]. The observation of RCE by another decay channel of the excited state, *i.e.*, de-excitation with the X-ray emission, was also made using the ions with smaller orbital radii of excited electrons [10,19]. The RCE process was also investigated theoretically [11,12], and the main purpose of recent works is to evaluate the coupled treatment of coherent process with incoherent (ionization, excitation and de-excitation) processes [13-15].

When the ion is channeled along an axis with its velocity v, the frequency of the periodic perturbation on the ion by the crystal potential is given by $\nu = \gamma v/d$, where $\gamma = 1/\sqrt{1-(v/c)^2}$, and d is the distance between atoms along the axis (Fig.2.8). If the internal energy difference of the ion, E_{trans}, matches $nh\nu$, the RCE occurs, *i.e.*, the condition of RCE for axial channeling is given by

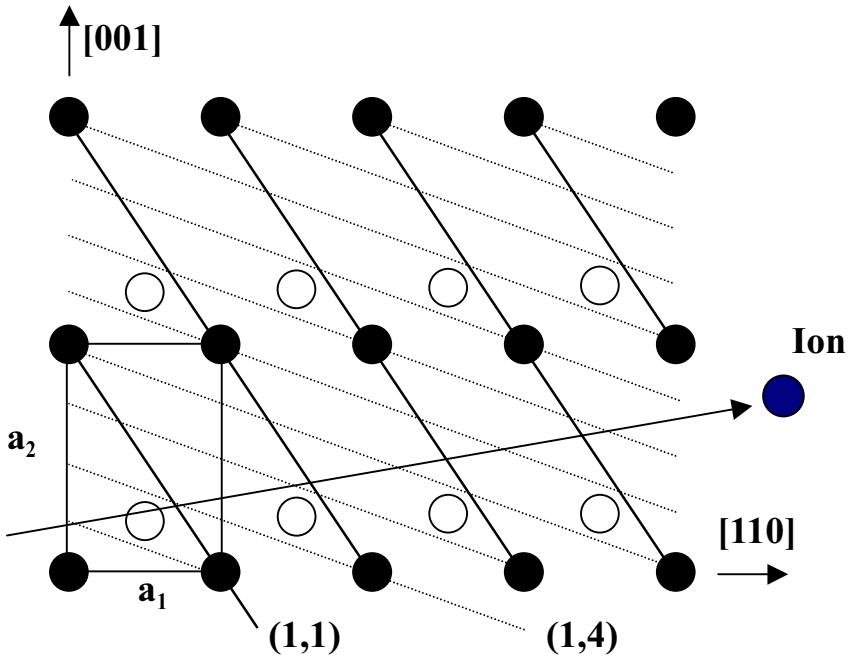

Fig.2.13 Arrangement of atomic strings on Si$(2\bar{2}0)$ plane. The solid and dotted lines indicate (1,1) and (1,4) strings, respectively.

$$E_{\text{trans}} = \frac{nh\upsilon\gamma}{d}. \qquad (n = 1,2,3,\cdots) \tag{2.84}$$

Under planar channeling conditions also, the RCE occurs by feeling the periodic arrangement of atomic strings lying on the channeling plane as shown in Fig.2.13. The RCE condition for planar channeling cases can be derived as follows.

The primitive translation vectors $\mathbf{a}_1$, $\mathbf{a}_2$ are defined so that $\mathbf{a}_1$ and $\mathbf{a}_2$ are parallel to the channel plane. In the case of Si crystal, sets of $\mathbf{a}_1$ and $\mathbf{a}_2$ can be written as

$$\begin{aligned}
&\mathbf{a}_1 = [110]a/2, \ \mathbf{a}_2 = [001]a \quad \text{for } (2\bar{2}0) \text{ plane,} \\
&\mathbf{a}_1 = [110]a/2, \ \mathbf{a}_2 = [1\bar{1}0]a/2 \quad \text{for (004) plane,} \\
&\mathbf{a}_1 = [110]a/2, \ \mathbf{a}_2 = [\bar{1}12]a/2 \quad \text{for (111) plane,}
\end{aligned} \tag{2.85}$$

where a is the lattice constant. The third primitive translation vector, $\mathbf{a}_3$, is taken to a lattice point on the neighboring plane. The reciprocal lattice vector is given by

$$\begin{aligned}
\boldsymbol{G}' &= k\mathbf{b}_1 + l\mathbf{b}_2 + m\mathbf{b}_3 \\
&= \boldsymbol{G}'(k,l) + m\mathbf{b}_3,
\end{aligned} \tag{2.86}$$

where

$$\begin{aligned}
&\mathbf{b}_1\cdot\mathbf{a}_1 = \mathbf{b}_2\cdot\mathbf{a}_2 = \mathbf{b}_3\cdot\mathbf{a}_3 = 1, \\
&\mathbf{b}_1\cdot\mathbf{a}_2 = \mathbf{b}_2\cdot\mathbf{a}_3 = \mathbf{b}_3\cdot\mathbf{a}_1 = \mathbf{b}_1\cdot\mathbf{a}_3 = \mathbf{b}_2\cdot\mathbf{a}_1 = \mathbf{b}_3\cdot\mathbf{a}_2 = 0.
\end{aligned} \tag{2.87}$$

The inter-planar distance d_{p} is given by $1/|\mathbf{b}_3|$. Hereafter, z-axis and x-axis are taken to be parallel to the ion velocity and perpendicular to the channel plane, respectively. The position of the ion moving with the velocity, $\boldsymbol{\upsilon}$, in the laboratory frame is given by

$$\boldsymbol{R}(t') = \boldsymbol{R}_\perp + \boldsymbol{\upsilon}t' = (X, Y, \upsilon t'). \tag{2.88}$$

Using Eqs.(2.85)-(2.88), the potential which the ion feels at position $\boldsymbol{R}(t')$ is expressed as

$$\begin{aligned}
\phi'(\boldsymbol{R}(t')) &= \sum_{G'} \phi_{G'} \exp\left[-i\boldsymbol{G}'\cdot\boldsymbol{R}(t')\right] \\
&= \sum_{k,l}\sum_{m} \phi_{klm} \exp\left[-i\left(\boldsymbol{G}'(k,l) + m\mathbf{b}_3\right)\cdot\left(\boldsymbol{R}_\perp + \boldsymbol{\upsilon}t'\right)\right] \\
&= \sum_{k,l} \phi_{kl}(X) \exp\left[-2\pi i\left(\boldsymbol{G}'(k,l)\cdot(\boldsymbol{R}_\perp + \boldsymbol{\upsilon}t')\right)\right],
\end{aligned} \tag{2.89}$$

where

$\phi_{G'}$ ($=\phi_{klm}$) is the Fourier component of the potential, and

$$\phi_{kl}(X) = \sum_{m} \phi_{klm} \exp(-2\pi i m X/d_{\text{p}}). \tag{2.90}$$

It is noted that the Fourier component of $(k,l) = (0,0)$, which is

$$\phi_{00}(X) = \sum_{m} \phi_m \exp(-2\pi i m X/d_{\text{p}}), \tag{2.91}$$

corresponds to the planar potential averaged along the plane.

The ion velocity is written as

$$\boldsymbol{\upsilon} = (\upsilon/\sin\Theta)\left[\boldsymbol{e}_1 \sin(\Theta-\theta) + \boldsymbol{e}_2 \sin\theta\right], \tag{2.92}$$

where Θ and θ are angles between $\mathbf{a}_1$ and $\mathbf{a}_2$ and between $\boldsymbol{\upsilon}$ and $\mathbf{a}_1$, respectively, $\boldsymbol{e}_1$ and $\boldsymbol{e}_2$ are unit vectors along $\mathbf{a}_1$ and $\mathbf{a}_2$. Therefore, the frequency for the ion to pass across the (k,l) atomic strings in the laboratory frame is

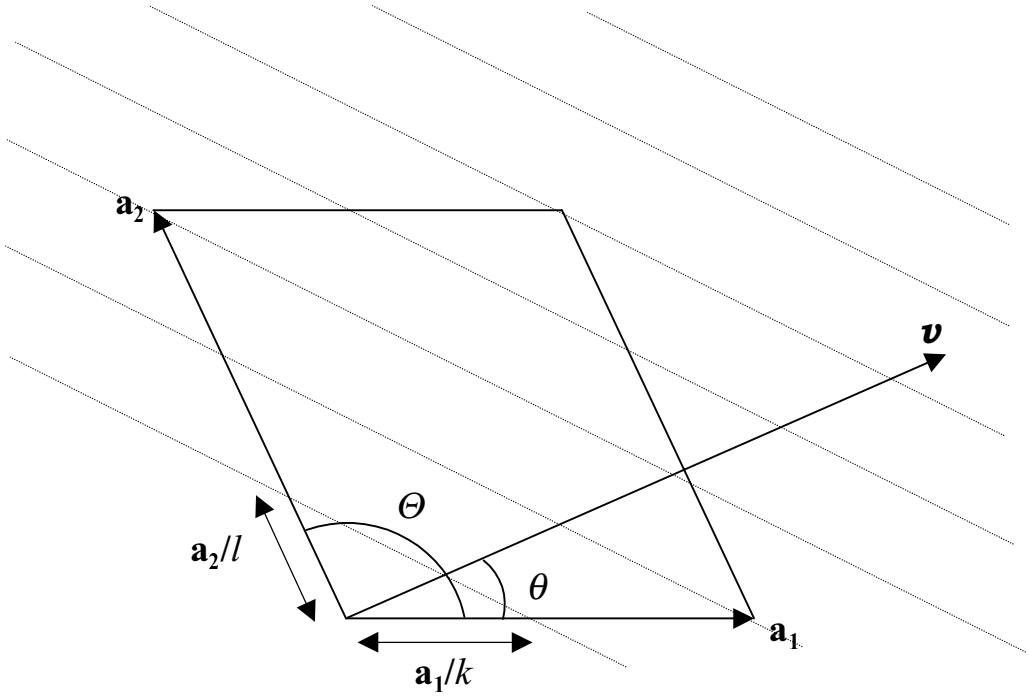

Fig.2.14 (k,l) atomic strings (dotted lines) which the ion with the velocity $\boldsymbol{v}$ passes. Angles between $\mathbf{a}_1$ and $\mathbf{a}_2$ and between $\boldsymbol{v}$ and $\mathbf{a}_1$ are represented as Θ and θ, respectively.

$$\begin{aligned} \nu'(\mathrm{k,l}) &= \boldsymbol{G}'(\mathrm{k,l})\cdot\boldsymbol{v} \\ &= (v/\sin\Theta)\left[k\sin(\Theta-\theta)/|\mathbf{a}_1| + l\sin\theta/|\mathbf{a}_2|\right]. \end{aligned} \tag{2.93}$$

The (k,l) atomic strings are parallel to a line, which intersects $\mathbf{a}_1$ and $\mathbf{a}_2$ at $\mathbf{a}_1/k$ and $\mathbf{a}_2/l$, respectively, as shown in Fig.2.14. The frequency in the projectile frame is transformed to

$$\nu(k,l) = \gamma\nu'(k,l) \tag{2.94}$$

Therefore, the (k,l) resonance condition results in

$$E_{\mathrm{trans}} = (\gamma\hbar v/\sin\Theta)\left[k\sin(\Theta-\theta)/|\mathbf{a}_1| + l\sin\theta/|\mathbf{a}_2|\right]. \tag{2.95}$$

For (004), (220) and (111) planar channeling cases in a diamond structure, $\mathbf{a}_1$ and $\mathbf{a}_2$ can be chosen perpendicular to each other, and Eq.(2.95) becomes

$$E_{\mathrm{trans}} = \frac{\gamma\hbar v}{a}\left(\frac{k\cos\theta}{A} + \frac{l\sin\theta}{B}\right), \tag{2.96}$$

where (A,B) are $(1/\sqrt{2},1/\sqrt{2})$, $(1/\sqrt{2},1)$ and $(1/\sqrt{2},\sqrt{3/2})$ for (004), (220) and (111) planar channeling cases, respectively.

2.3.2. Selection rule

As shown in Fig.2.13, in the case of $(k,l) = (1,4)$ resonance for (220) planar channeling, another set of atomic strings (open circles) exists just in the middle of the (1,4) strings (closed circle). The potential for ions is completely canceled by the interference between these two arrangements of the strings, and the resonant excitation does not occur. To obtain the (k,l) combinations for absences of the resonant excitation, only the unit cell is sufficient to be considered. The point of the open circle is expressed as

$$\boldsymbol{A}_{\mathrm{open}} = (1/2)\mathbf{a}_1 + (1/4)\mathbf{a}_2. \tag{2.97}$$

one of the points on the n-th (k,l) string, $\boldsymbol{A}_{\mathrm{n}}$, which is parallel to $\boldsymbol{A}_{\mathrm{open}}$, is written as

$$\boldsymbol{A}_n = n\left(\frac{2\mathbf{a}_1}{2k+l} + \frac{\mathbf{a}_2}{2k+l}\right). \tag{2.98}$$

The condition, $(\boldsymbol{A}_n + \boldsymbol{A}_{n+1})/2 = \boldsymbol{A}_{\mathrm{open}}$, is made when the (k,l) combination satisfies,

$$2k + l = 4n + 2. \tag{2.99}$$

For $(\bar{1}11)$ planar channeling, $\boldsymbol{A}_{\mathrm{open}}$ becomes

$$\boldsymbol{A}_{\mathrm{open}} = (1/2)\mathbf{a}_1 + (1/2)\mathbf{a}_2, \tag{2.100}$$

and the (k,l) combinations for absence of the resonant excitation should be

$$k + l = 2n + 1. \tag{2.101}$$

In the case of (004) channeling, there is only one atom in a unit cell, and all the (k,l) combinations are allowed.

2.3.3. Energy level splitting of excited states

Under the channeling condition, excited states of the ions are split into several levels by the Stark effect due to the crystal static potential. The non-perturbed Hamiltonian for an electron in a hydrogen-like ion is given by

$$H_0(r) = -c\,\boldsymbol{\alpha}\cdot\boldsymbol{p} - \beta mc^2 - \frac{Z_1 e^2}{r}. \tag{2.102}$$

A Hamiltonian for the charged particle in the electromagnetic field can be expressed by the replacements,

$$\boldsymbol{p} \rightarrow \boldsymbol{p} - \frac{e}{c}\boldsymbol{A}, \quad H \rightarrow H + e\phi, \tag{2.103}$$

where $\boldsymbol{A}$ and ϕ are vector and scalar potentials, respectively, and the Hamiltonian for the electron in the hydrogen-like ions passing in a crystal results in

$$\begin{aligned} H(\boldsymbol{r},t) &= -\boldsymbol{\alpha}\cdot\left[c\boldsymbol{p} + e\boldsymbol{A}(\boldsymbol{r},t)\right] - \beta mc^2 - \frac{Z_1 e^2}{r} - e\phi_{\mathrm{W}}(\boldsymbol{r}) - e\phi(\boldsymbol{r},t), \\ &= -c\,\boldsymbol{\alpha}\cdot\boldsymbol{p} - \beta mc^2 - \frac{Z_1 e^2}{r} - e\phi_W(\boldsymbol{r}) - e\gamma(1-\beta\alpha_z)\phi(\boldsymbol{r}',t). \end{aligned} \tag{2.104}$$

where $\phi_{\mathrm{W}}(\boldsymbol{r})$ is a wake potential, which is induced by a response of the material (crystal) to the moving ion, $\phi(\boldsymbol{r},t)$ is a crystal potential, the relations of the four-potential, $A_x(\boldsymbol{r},t) = A_y(\boldsymbol{r},t) = 0$, and $A_z(\boldsymbol{r},t) = -\beta\phi(\boldsymbol{r},\mathrm{t})$ are used, and the position $\boldsymbol{r}'$ in the laboratory frame is given by $\boldsymbol{r}' = \boldsymbol{R} + \boldsymbol{r} = \boldsymbol{R}_\perp + \boldsymbol{r}_\perp + \gamma(z\boldsymbol{e}_z + \boldsymbol{v}t)$, and $\boldsymbol{e}_z$ is an unit vector along z-axis. The perturbation terms of Eq.(2.104) are written as

$$H_1(\boldsymbol{r}) = -e\phi_W(\boldsymbol{r}), \tag{2.105}$$

$$H_2(x) = -e\gamma(1-\beta\alpha_z)\phi_{00}(X+x), \tag{2.106}$$

$$H_3(r,t) = -e\gamma(1-\beta\alpha_z)\sum_{k,l\neq 0}\phi_{kl}(X+x)\exp\left[-2\pi i\boldsymbol{G}'(k,l)\cdot(\boldsymbol{R}_\perp+\boldsymbol{r}_\perp+\gamma z\boldsymbol{e}_z)\right]$$
$$\times\exp\left[-2\pi i\nu(k,l)t\right]. \tag{2.107}$$

In the following calculation, a contribution from minor components in $H_2(x)$ and $H_3(\boldsymbol{r},t)$, $\beta\alpha_z$, is at most ~0.1, and is neglected as $1-\beta\alpha_z$ ~1, the wake potential is calculated from a dielectric function in the plasmon pole approximation, and the Doyle-Turner potential is adopted for the crystal potential [76]. The stationary Hamiltonian, $H_0 + H_1 + H_2$, gives eigenstates of the ion in the crystal, and the time-dependent Hamiltonian, H_3, induces the transition between the eigenstates. In this case, nuclear fields for electrons in $n = 2$ and 3 states are ~190 and ~40 V/Å, respectively. The difference between these two fields is larger than a typical static crystal field, for instance, ~20 V/Å at 0.5 Å distance from the channel center. Therefore, mixings between different n states are neglected. The wake field is ~0.5 V/Å, and plays little role in this energy region.

The unperturbed wave function is expressed as $|nLJ\mu\rangle$ with the principal quantum number, n, the orbital angular momentum, L, the total angular momentum, J, and the projection of J to the quantization axis, μ. The perturbed energy eigenvalue of the ground state is given by

$$E_1 = E_1^0 + \langle 1\mathrm{s}(1/2)\mu|H_1(r)+H_2(r)|1\mathrm{s}(1/2)\mu\rangle, \tag{2.108}$$

where E_1^0 is the unperturbed energy eigenvalue, and $|1\mathrm{s}(1/2)\mu\rangle$ is the wave function of the ground state. The eigenfunction of $n = 2$ state is expressed as a linear combination of the unpertubed wave functions of $n = 2$ sublevels, which is

$$\Psi_2 = \sum_{L,J,\mu} c_{LJ\mu}|2LJ\mu\rangle = c_{2\mathrm{s}}\Psi_{2\mathrm{s}} + c_{2\mathrm{px}}\Psi_{2\mathrm{px}} + c_{2\mathrm{py}}\Psi_{2\mathrm{py}} + c_{2\mathrm{pz}}\Psi_{2\mathrm{pz}}, \tag{2.109}$$

where Ψ are the non-relativistic wave functions with spin states. Energy eigenvalues of $n = 2$ states and the coefficients in Eq.(2.109) are obtained by solving the secular equation,

$$\det\left|\langle 2LJ\mu|H_0(\boldsymbol{r})+H_1(\boldsymbol{r})+H_2(\boldsymbol{r})-E|2L'J'\mu'\rangle\right| = 0. \tag{2.110}$$

The Lamb shift of the ground state, $\Delta E_{1\mathrm{s}}$= 1.14 eV, and that of 2s state, $\Delta E_{2\mathrm{s}}$= 0.16 eV [77], was included in the unperturbed energy eigenvalues in the present calculation.

The calculated energy levels of $n = 2$ states as a function of the ion position in the present experimental condition, 390 MeV/u Ar^{17+} in Si (220) channel, is shown in Fig.2.15. The $n = 2$ states are split into four levels due to the spin-orbit interaction and the Stark effect by the crystal static field. These four levels are hereafter named as Levels 1 – 4 in the order of increasing transition energy. The compositions of the wave functions of Levels 1 – 4, and schematics of the electron distribution, $\Psi_2^*\Psi_2$, in each level are shown in Fig.2.16. The level splitting into two parts at the channel center are originated in the spin-orbit interaction. Level 1, 2 and Level 3, 4 correspond to the states with $J = 1/2$ and $J = 3/2$, respectively. The 2s component is dominant in Level 1 and 2, and occupies the Level 2 rather than Level 1 in the vicinity of the channel center, because of the slightly larger transition energy to the 2s state due to the Lamb shift. The importance of the crystal field increases as the ion approaches the channel wall, and the

energy splitting between four levels becomes wider. The crystal field plays a major role for the Stark mixing between 2s and $2p_x$ in Level 1 and 4. It is noted that the larger wing of the electron cloud extends toward the channel wall in Level 1, however, it extends toward the channel center in Level 4.

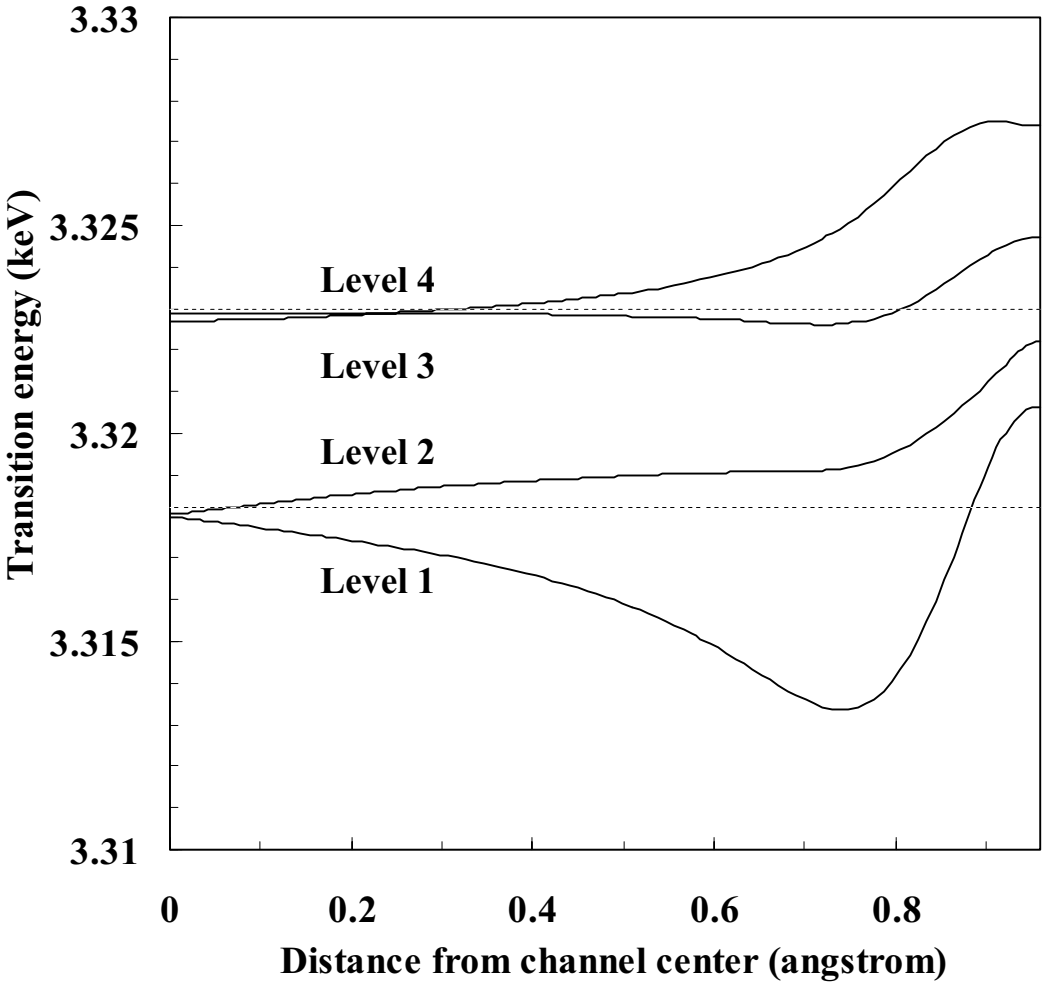

Fig.2.15 Calculated transition energy from 1s to $n = 2$ states of hydrogen-like Ar ion in vacuum as a function of the distance from channel center. Dotted lines indicate transition energies to $n = 2$ states (J = 1/2 and J = 3/2).

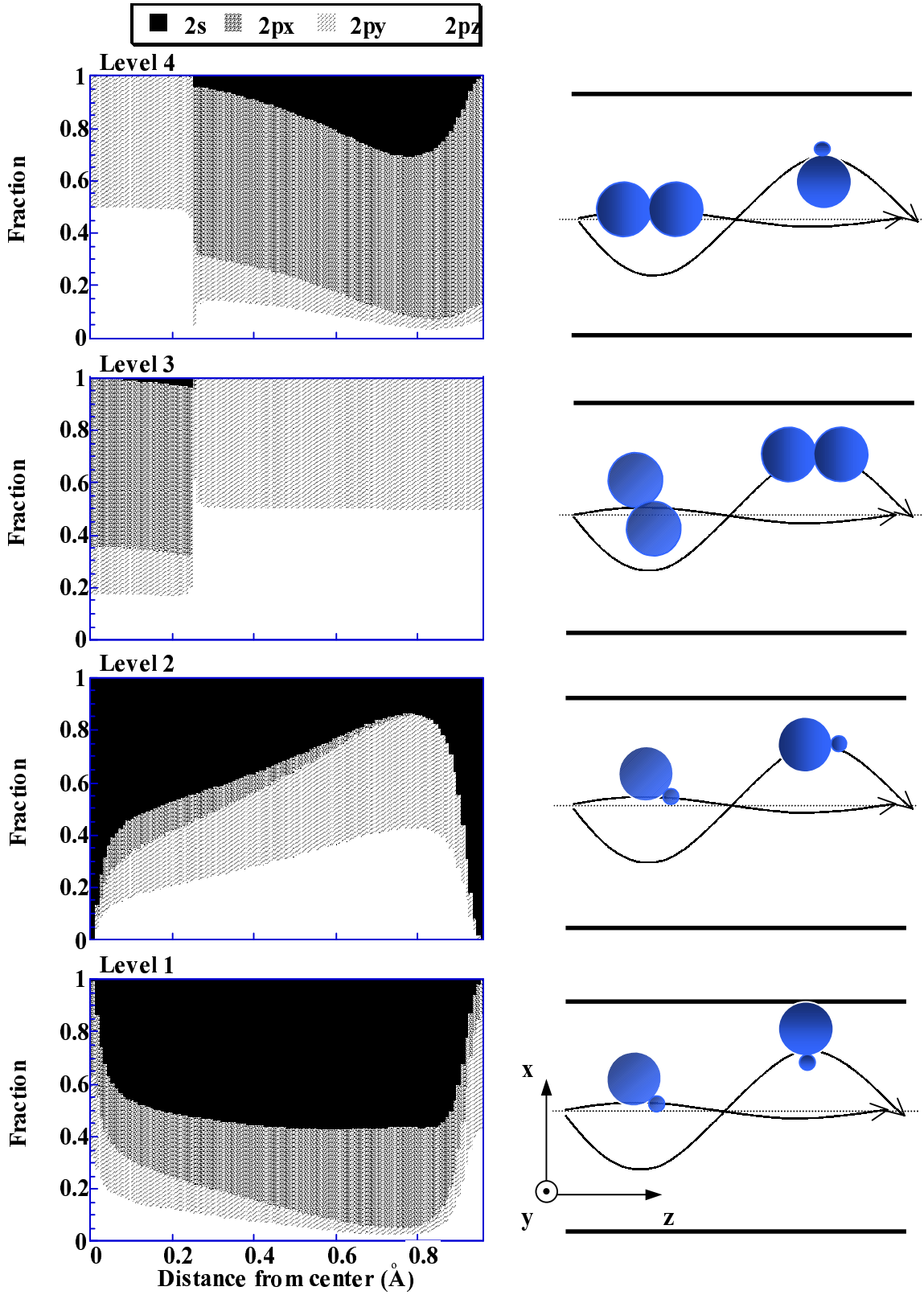

Fig.2.16 Compositions of 2s, $2p_x$, $2p_y$ and $2p_z$ states in Level 1 – 4 as a function of the distance from channel center, and the schematics of electron distribution in the respective levels.

2.3.4. Transition amplitude

The transition probability for RCE from the initial state Ψ_1 to the final state Ψ_2 is obtained by solving the time dependent Schrödinger equation, which is in the present case,

$$i\hbar\frac{\partial\Psi(\boldsymbol{r},t)}{\partial t}=\left[H_0(\boldsymbol{r})+H_1(\boldsymbol{r})+H_2(\boldsymbol{r})+H_3(\boldsymbol{r},t)\right]\Psi(\boldsymbol{r},t). \tag{2.111}$$

The solution of the time dependent Schrödinger equation can be written as

$$\Psi(\boldsymbol{r},t)=\sum_j a_j(t)\Psi_j(\boldsymbol{r})\exp(-iE_jt/\hbar), \tag{2.112}$$

where E_j is the energy eigenvalue of H_0 + H_1 + H_2. Substituting Eq.(2.112) into Eq.(2.111), we obtain

$$\begin{aligned}i\hbar\frac{\partial a_j(t)}{\partial t}&=\sum_{j'}a_{j'}(t)\left\langle j\left|H_3(r,t)\right|j'\right\rangle\exp\left[i(E_j-E_{j'})t/\hbar\right],\\&=-e\gamma\sum_{j'}\sum_{k,l\neq0}a_{j'}(t)\left\langle j\left|\phi_{kl}(X+x)\exp\left[-2\pi i\boldsymbol{G}'(k,l)\cdot\gamma z\boldsymbol{e}_z\right]\right|j'\right\rangle\\&\qquad\times\exp\left[i(E_j-E_{j'})/\hbar-2\pi i\nu(k,l)t\right].\end{aligned} \tag{2.113}$$

Considering the transition from the state Ψ_1 to the state Ψ_2, Eq.(2.109) becomes

$$\begin{aligned}i\hbar\frac{\partial a_2(t)}{\partial t}&=-e\gamma\sum_{k,l\neq0}a_1(t)\left\langle2\left|\phi_{kl}(X+x)\exp\left[-2\pi i\boldsymbol{G}'(k,l)\cdot(\boldsymbol{r}_\perp+\gamma z\boldsymbol{e}_z)\right]\right|1\right\rangle\\&\qquad\times\exp\left[i(E_2-E_1)/\hbar-2\pi i\nu(k,l)t\right]\\&=M_{21}(X)a_1(t)\exp\left[i(E_2-E_1)/\hbar-2\pi i\nu(k,l)t\right]\\&=M_{21}(X)a_1(t)\exp(i\Delta_{21}t),\end{aligned} \tag{2.114}$$

where

$$M_{21}(X)=-e\gamma\sum_{k,l\neq0}\left\langle2\left|\phi_{kl}(X+x)\exp\left[-2\pi i\boldsymbol{G}'(k,l)\cdot(\boldsymbol{r}_\perp+\gamma z\boldsymbol{e}_z)\right]\right|1\right\rangle, \tag{2.115}$$

and

$$\Delta_{21}=(E_2-E_1)/\hbar-2\pi\nu(k,l). \tag{2.116}$$

The squared transition matrix element, $\left|M_{21}(X)\right|^2$, for (k,l) = (1,1) from 1s state to Level 1 – 4 of 390 MeV/u Ar^{17+} ion channeled in a $\mathrm{Si}(220)$ planes are shown in Fig.2.17. They become larger as the ion approaches the channel wall because of the stronger crystal periodic potential. Similarly, in the case of resonant coherent de-excitation (RCD) from the state Ψ_2 to the state Ψ_1, Eq.(2.113) becomes

$$i\hbar\frac{\partial a_1(t)}{\partial t}=M_{21}^*(X)a_2(t)\exp(-i\Delta_{21}t). \tag{2.117}$$

Solving Eqs.(2.114) and (2.117) with an assumption that Δ_{21} and $M_{21}(X)$ are independent of t under a condition of $a_1(0)$ = 1, $a_2(0)$ = 0, we get

$$a_1(t)=\exp(-i\Delta_{21}t/2)\left(\cos\frac{\Omega}{2}t+\frac{i\Delta_{21}}{\Omega}\sin\frac{\Omega}{2}t\right), \tag{2.118}$$

$$a_2(t)=-\frac{2iM_{21}(X)}{\hbar\Omega}\exp(i\Delta_{21}t/2)\sin\frac{\Omega}{2}t, \tag{2.119}$$

where

$$\Omega = \sqrt{\Delta_{21}^2 + \frac{4\left|M_{21}(X)\right|^2}{\hbar^2}}, \tag{2.120}$$

is called "Rabi frequency". The population in the state Ψ_2, which is given by $\left|a_2(t)\right|^2$, oscillates with the frequency Ω. The oscillation is called "Rabi oscillation". The transition probability per unit time from the state Ψ_1 to the state Ψ_2 results in

$$w_{21} = \frac{d\left|a_2(t)\right|^2}{dt} = \frac{2\left|M_{21}(X)\right|^2}{\hbar^2 \Omega} \sin \Omega t . \tag{2.121}$$

The Rabi frequencies at a large distance (=0.72 Å: three-quarter of the distance between the channel center and wall) and at the channel center are 1.0×10^{15} and 1.4×10^{14} $\sec^{-1}$, respectively. In other words, the ion path lengths per Rabi oscillation, λ_R, in the laboratory frame are 1.8 and 13.5 μm for the above two cases.

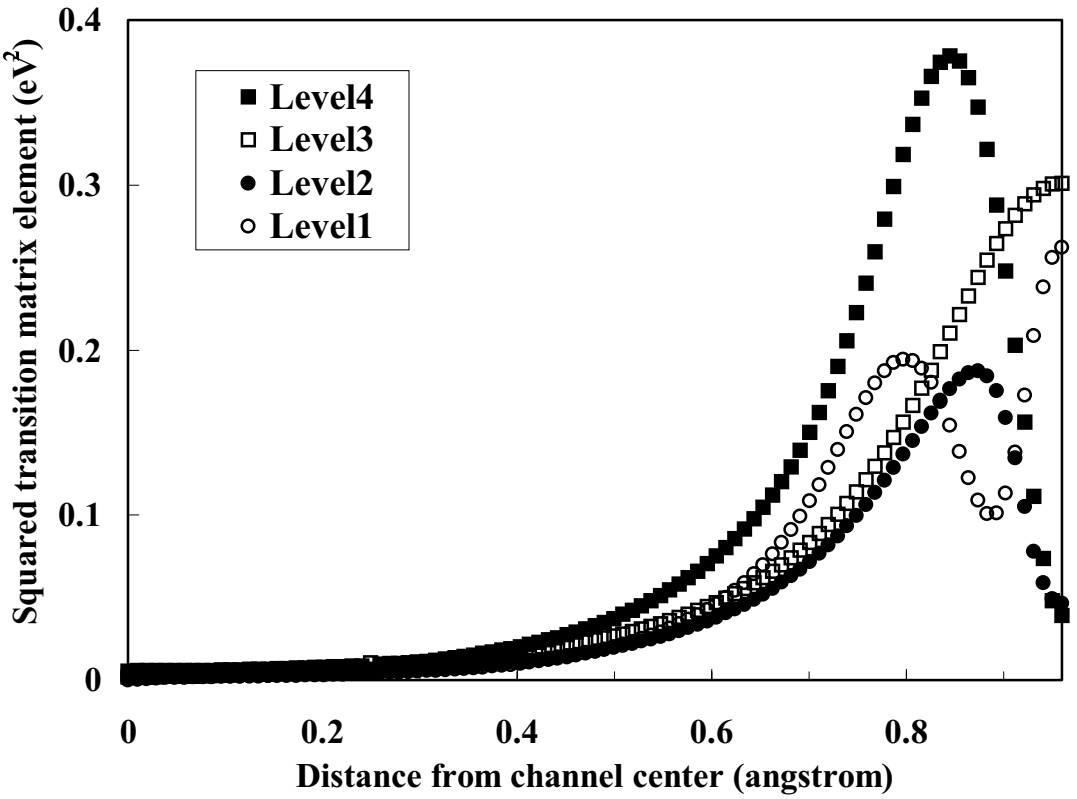

Fig.2.17 Calculated squared matrix element for $(k,l) = (1,1)$ transition from 1s state to Level 1 – 4 of 390 MeV/u Ar^{17+} ion channeled in Si $(2\bar{2}0)$ planes.

3. Channeling experiment

3.1. Parallel beam for relativistic channeling

At the beginning, channeling experiments, which are necessary for the RCE observation, were performed using 290 MeV/u C^{6+} and 390 MeV/u Ar^{17+} ions with Si crystal. The channeling phenomena were extensively investigated with lower energy ions so far [1,2]. A channeling experiment with relativistic heavy ions, however, is limited, because only a few accelerators are available [74,78]. The critical angles for 290 MeV/u C^{6+} and 390 MeV/u Ar ions channeled along Si (220) plane are evaluated to be 0.12 and 0.10 mrad, respectively, from Eq.(2.77). In general, two slits are adopted to make a parallel beam. However, the slit becomes one of the origins for producing the fragments of the projectile in such a high energy region. In the present experiment, a single iron-collimator with the thickness of 5 cm and the inner-diameter of 1 mm was adopted at 650 cm upstream of the target crystal (see Fig.3.2). The thickness of the iron-collimator is larger than the ranges of the incident C and Ar ions. The beam optics was tuned to be parallel, *i.e.*, not focused, before the beam passed through the collimator. Fig.3.1 shows a direct beam spot profile of 290 MeV/u C^{6+} beam detected by a 2D position sensitive detector (PSD) located at 8.5 m (the distance in C beam case is different from that in Fig.3.2) downstream from the collimator. The spot size (FWHM) was 1.5 mmϕ. From the spot size and the distance between the collimator and the PSD, the beam divergence (HWHM) was geometrically determined to be (1.5/2+1.0/2)/8500 ~0.15 mrad. In the case of 390 MeV/u Ar^{17+} ions, 1.8 mmϕ spot size was obtained, and the beam divergence becomes (1.8/2+1.0/2)/12100 ~0.12 mrad. These beam divergences are of the same order as the critical angles of channeling, and are small enough to observe channeling phenomena.

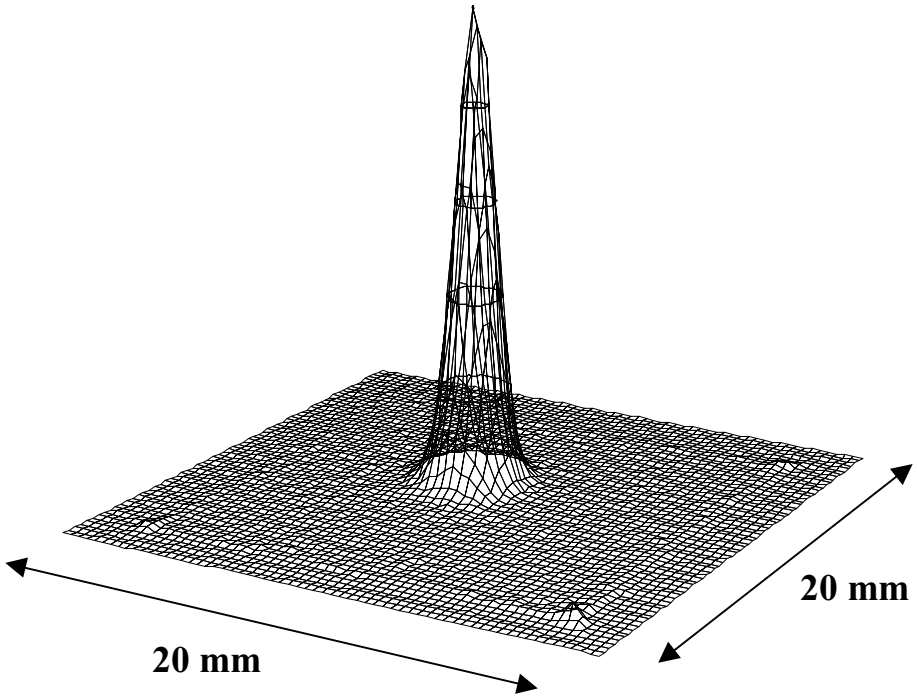

Fig.3.1 2D-spot size of collimated C beam at PSD.

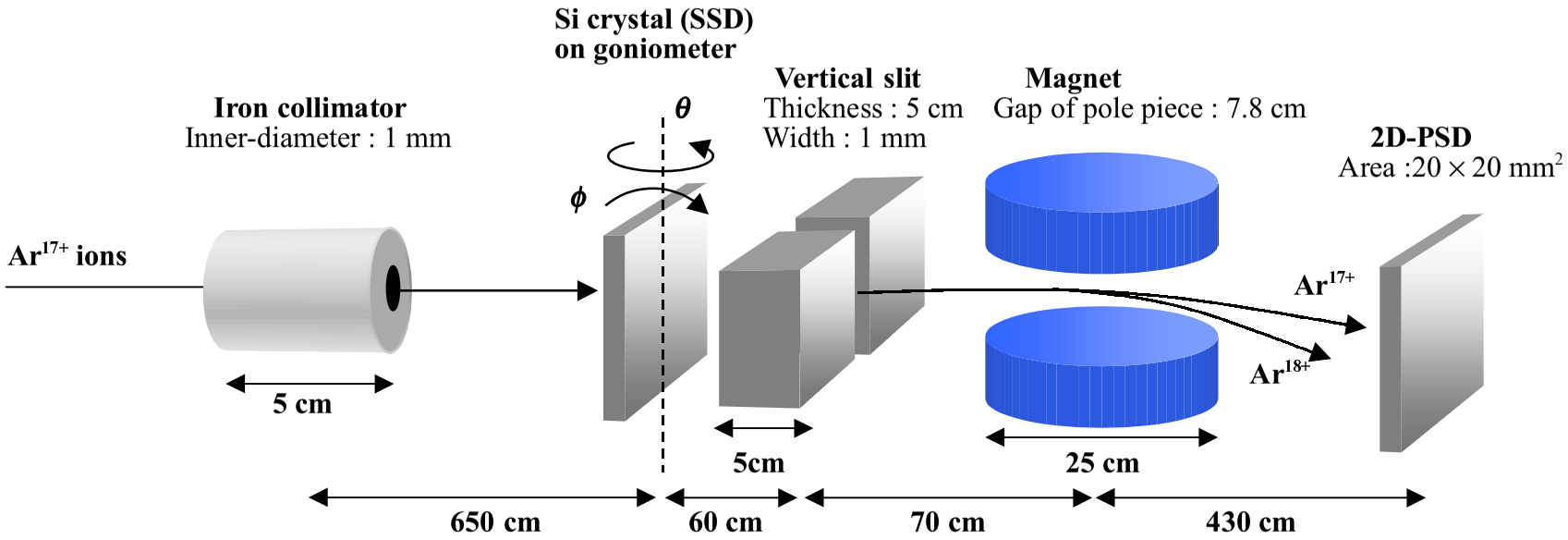

Fig.3.2 Schematic drawing of setup for channeling experiment

3.2. Experimental setup

A schematic drawing of the setup for the channeling experiment is given in Fig.3.2. The collimated Ar^{17+} (C^{6+}) beam was injected into a Si crystal. In the present experiment, a totally depleted silicon detector (SSD) was adopted as the target to measure the energy deposition in coincidence with the charge state distribution. The SSD was mounted on a three-axis goniometer with a precision of 0.001°. A schematic and a performance list of the goniometer are described in Fig.3.3. Photographs of the iron-collimator and the goniometer are shown in Fig.3.4 and Fig.3.5, respectively. The transmitted ions were charge-separated by a magnet, and were detected by the 2D-PSD at the end of the beam line. The diameter and the gap of the pole piece of the magnet were 25 and 7.8 cm, respectively. A distance between the magnet and the PSD was 430 cm. An active area of the PSD was 20×20 mm^2, and the thickness was 200 μm. The separation between Ar^{17+} and Ar^{18+} at the PSD was about 6 mm, when they were bent by ~0.023 rad from the incident direction. The role of the vertical slit before the magnet was to sharpen the beam spot in the horizontal direction at the PSD, because the tail of the angular distribution of the transmitted beam would have affected the neighboring distribution.

a. Silicon detector

The principle of the silicon detector (SSD) is shown in Fig.3.6. A semiconductor, like silicon, has a band gap between the conduction and the valence bands. When a particle is injected into the semiconductor and looses the energy in it, electrons in the valence band are excited to the conduction band across the band gap (energy gap : E_g), and holes are left in the valence band. The number of electron-hole pairs created by the particle incidence is given by

$$n = \Delta E/\varepsilon, \tag{3.1}$$

where ΔE is the energy deposition of the particle to the detector, and ε is the average energy which is necessary to create an electron-hole pair. These excited electrons are collected by a biased electrode, and we can know the energy deposition of the particle from the collected charge. SSDs with several thicknesses were adopted in the present study. We adopted SSDs with 19.4, 31.5, 78.5, 94.7 and 524 μm thick which have the energy resolutions of 30, 45, 50, 80 and 90 keV for 5.5 MeV α-particle, respectively. These detectors are covered by 40.5 μg/cm^2 Au on the entrance surface and 40 μg/cm^2 Al on the exit surface. The energy loss in the Au region was ~0.5 percent of the total energy loss even in the case of the 19.4 μm SSD, and can be neglected.

b. Position sensitive detector (PSD)

The PSD used in the present experiment is a silicon detector which has four equally biased electrodes on the four corners. When electric charges, Q_1, Q_2, Q_3 and Q_4 are collected to the electrodes E_1, E_2, E_3 and E_4 shown in Fig.3.7, the injected position of the particle is obtained by

$$\begin{cases} X = \dfrac{(Q_3+Q_4)-(Q_1+Q_2)}{Q_1+Q_2+Q_3+Q_4} \\ Y = \dfrac{(Q_1+Q_4)-(Q_2+Q_3)}{Q_1+Q_2+Q_3+Q_4} \end{cases}, \tag{3.2}$$

It is noted that when several particles are injected at the same time, the PSD recognizes

the position of their center of mass as the injected position. When the particle is injected around the center of the PSD, an electric noise component is much smaller than the real signals. On the other hand, when the particle is injected near one of the electrodes (e.g. E_1), real signals of the other electrodes, $Q_2 - Q_4$ become small enough to be comparable to the noise component. Therefore, the position resolution of the PSD depends on the injected position, and is worse near the edge than around the center. The resolutions of the PSD are about 0.1 mm × 0.1 mm and 0.8 mm × 0.8 mm around the center and near the edge, respectively.

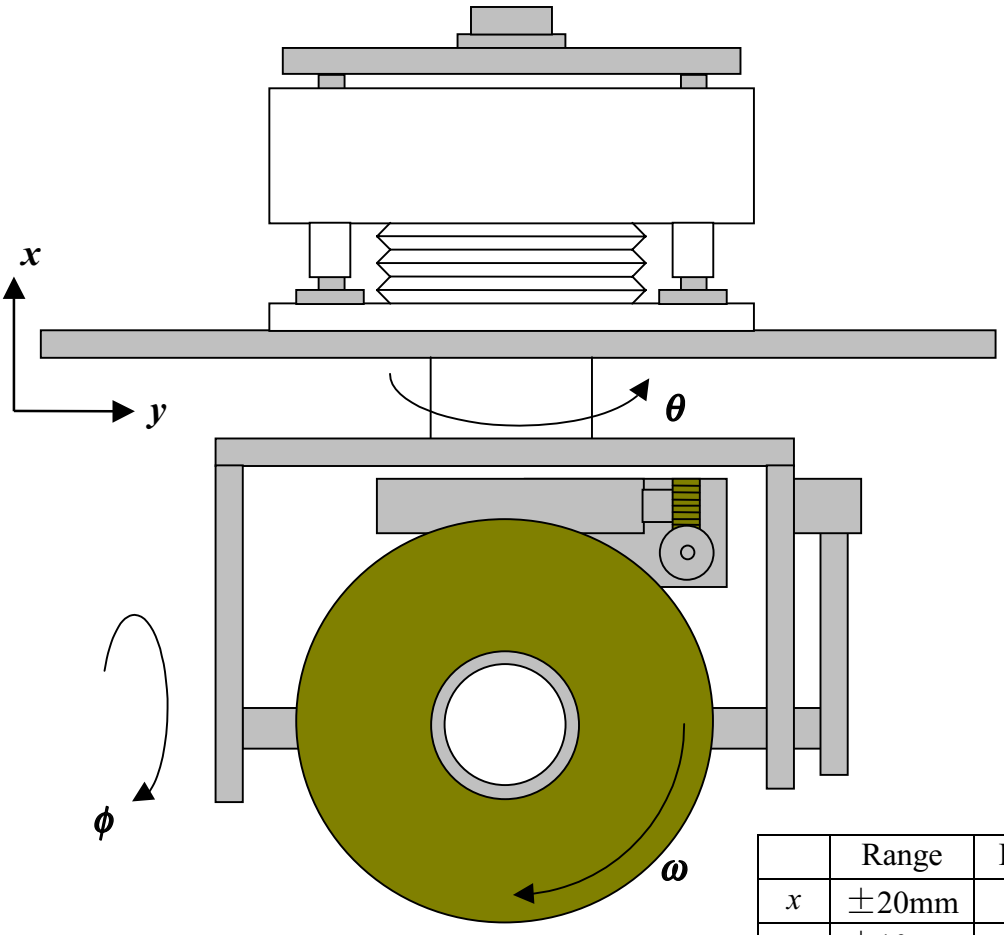

	Range	Precision
x	±20mm	0.1mm
y	±10mm	0.1mm
θ	±360 °	0.001 °
ϕ	±5 °	0.001 °
ω	±360 °	0.001 °

Fig.3.3 Schematic and performance of three-axis goniometer.

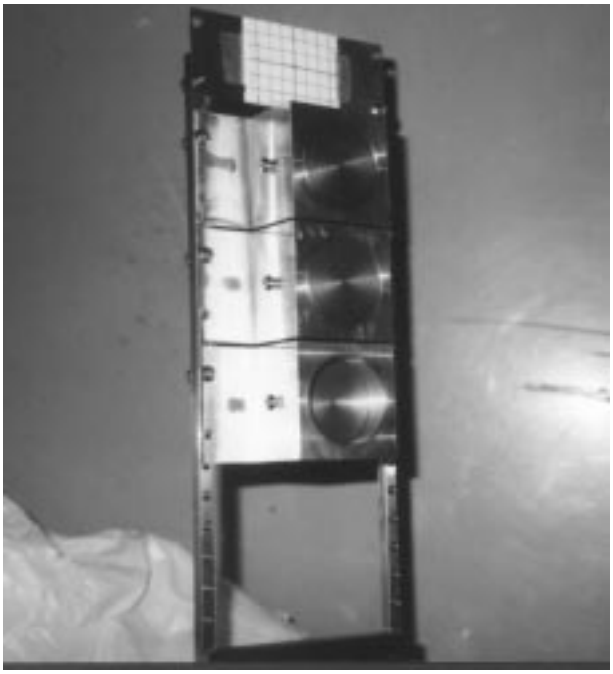

Fig.3.4 Photograph of iron-collimator.

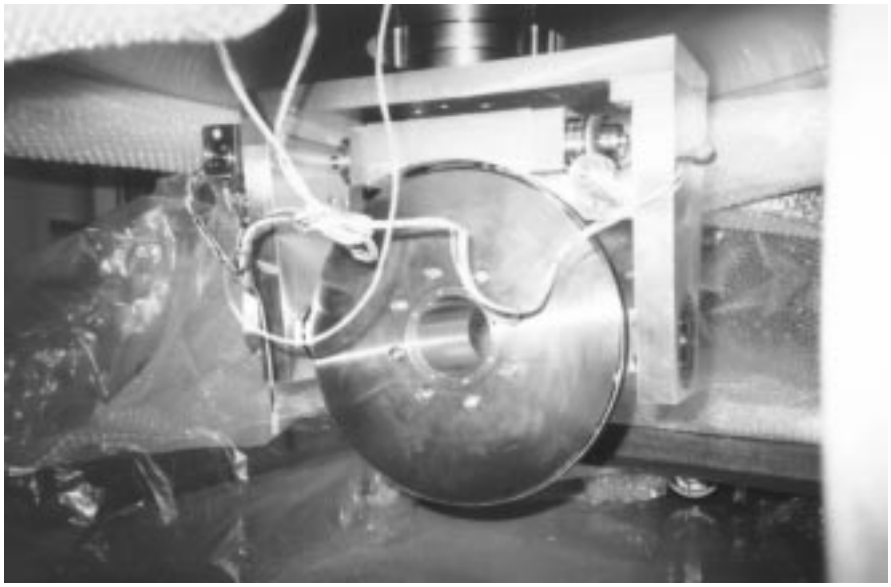

Fig.3.5 Photograph of goniometer.

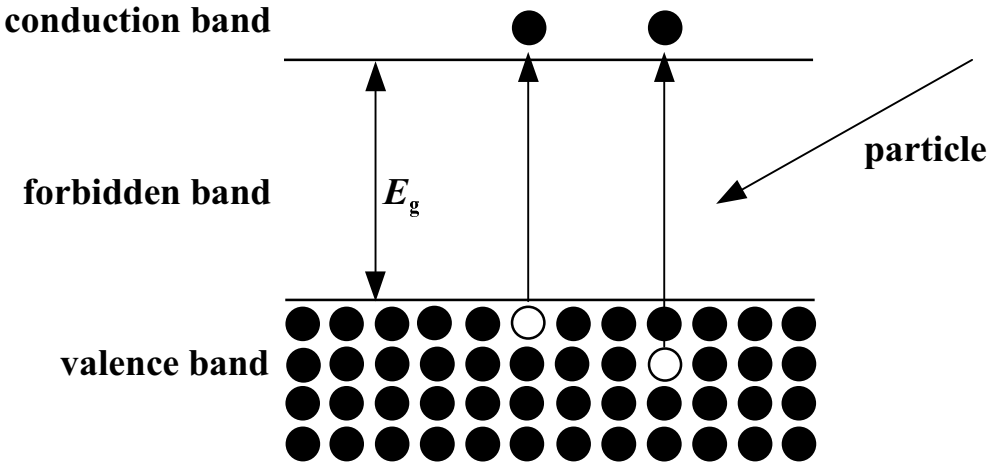

Fig.3.6 Principle of semiconductor detector.

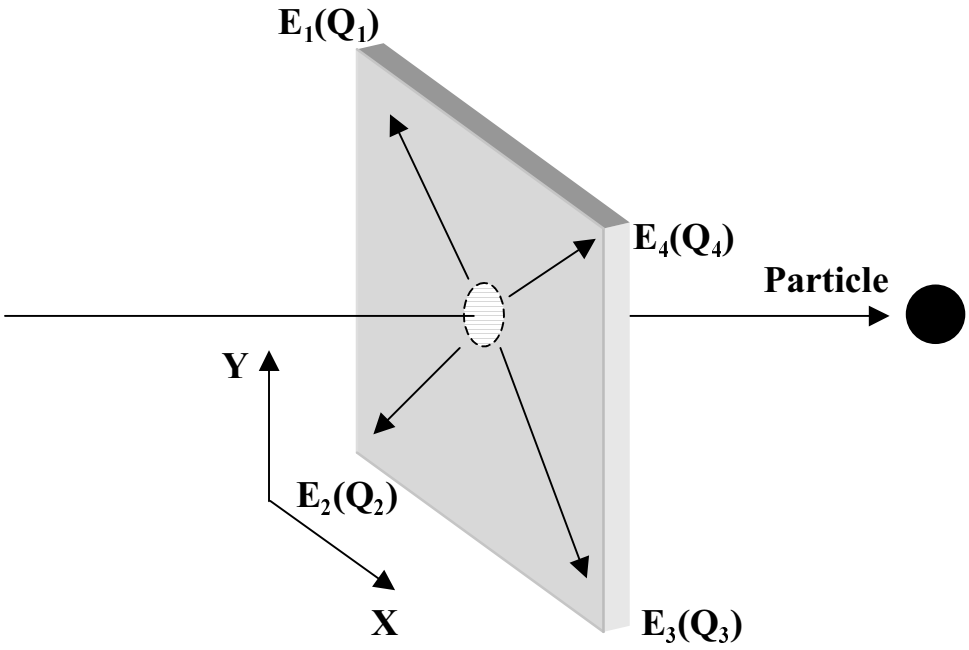

Fig.3.7 Principle of position sensitive detector to determine the injected position of the particle.

c. Electronic circuit

For the purpose of measuring the energy deposition of ions in coincidence with the charge state distribution of transmitted ions, a following electronic circuit for the measurement was made, and signals from the SSD and the PSD were taken event by event. A diagram of the electronic circuit is described in Fig.3.8. The electric charges collected from the SSD and the PSD were converted into voltages by pre-amplifiers, and their output pulses were amplified by spectroscopy amplifiers. The SSD signal was put into a timing-SCA (single channel analyzer). The timing-SCA gives a logic pulse when the input signal is higher than a certain level, and the noise component can be discriminated from the real signal. The output signal of the timing-SCA was connected to “timing in” of a peak-holder. The analog signals from the SSD and the PSD were delayed by 4.75 μs with delay amplifiers because the output signal of the timing-SCA was delayed ~3 μs from the input time. These analog signals were put into respective channels of the peak-holder. The peak-holder is active when the timing pulse gets in, and keeps pulse heights of the signals put into the respective channels of the peak-holder. Output signals of the peak-holder were connected to the analog-digital conversion (ADC)-board, and the digitized signals were taken into a personal computer. The pulse heights of the analog signals have to be kept by the peak-holder so that the analog-digital transformation is performed correctly. The data were recorded in a “list mode”.

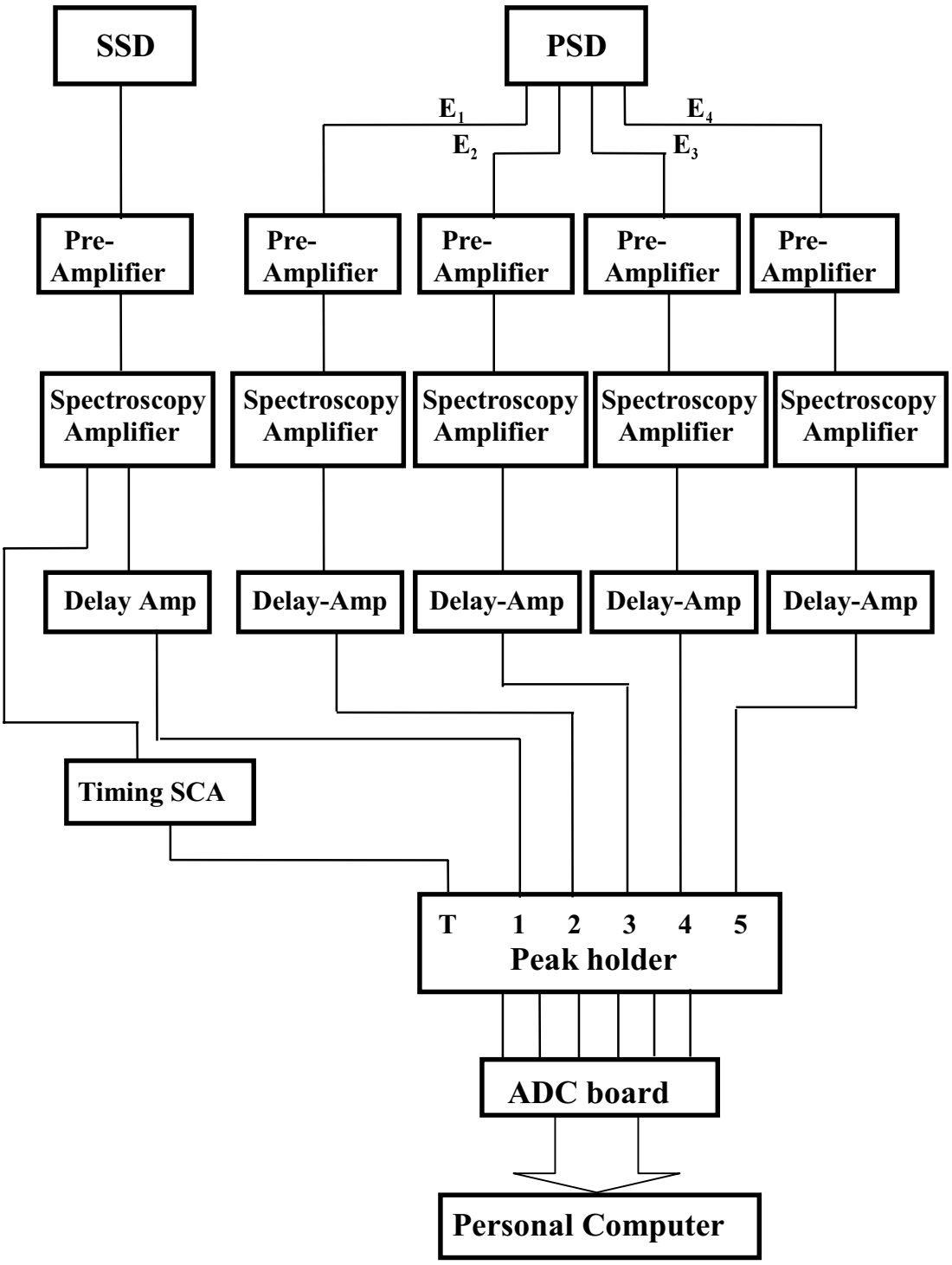

Fig.3.8 Electric circuit system for the coincidence measurement of the energy deposition to the SSD and the charge state distribution of transmitted ions by the PSD.

3.3. Random incidence

3.3.1. Energy deposition for random incidence

Before the channeling experiment, the energy loss and the energy deposition of random incident ions should be considered. The energy deposition to a Si target (SSD) was measured in the case of random incidence. For low energy ion, the energy deposition can be regarded as equal to the energy loss. In the case of the relativistic energy, however, the energy deposition deviates from the energy loss, because some energetic electrons produced by "binary collision" with the ion escape from the detector. A typical energy deposition spectrum for 390 MeV/u Ar^{17+} ion in the 19.4 μm thick Si target is shown in Fig.3.9. The average energy deposition amounts to 3.14 MeV. The mean-free-path for the electron loss in this case was estimated to be 3.3 μm [79], which is much smaller than the target thickness. Assuming that Ar^{17+} ions are ionized within 20 percent of the target thickness from the entrance surface, and the stopping power is proportional to the square of the charge, the difference of energy losses between Ar^{17+} and Ar^{18+} incidences in this target is estimated to less than 2 percent. The energy deposition of Ar^{17+} ion is considered to be almost equal to that of Ar^{18+} ion. The theoretical value of energy loss calculated with Eq.(2.32) for $Z_1 = 18$ is 3.73 MeV. To evaluate the energy loss from the energy deposition, the fraction of escaped electrons and their energies are necessary. Therefore, it is necessary to estimate the effect of the escaped electrons in order to compare the measured energy deposition with the theoretical energy loss.

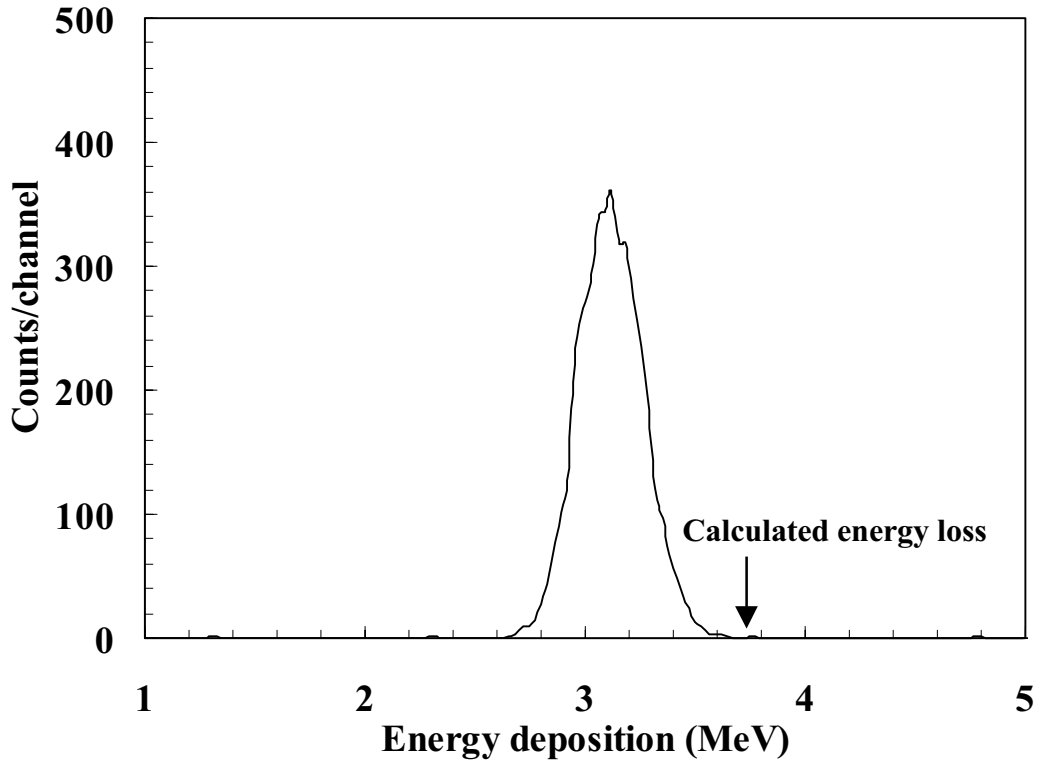

Fig.3.9 Spectrum of experimental energy deposition for 390 MeV/u Ar^{17+} incidence in the Si target with the thickness of 19.4 μm. The arrow indicates the value of the calculated energy loss.

Fig.3.10 shows measured energy depositions and theoretical energy losses for Si targets with several thicknesses. The difference tends to be larger as the target thickness increases, and must saturate for the thickness larger than the range of the scattered electron with the maximum energy (~1 MeV) in Si, which is ~1.7 mm.

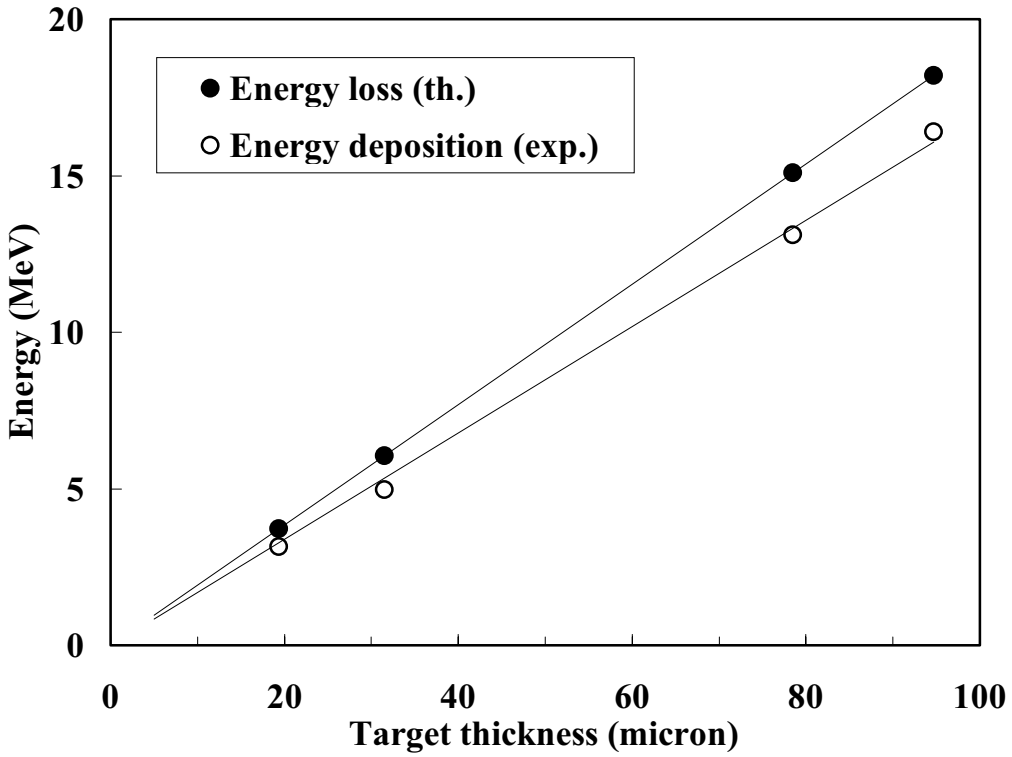

Fig.3.10 Comparison between theoretical energy loss and experimental energy deposition as a function of the target thickness.

3.3.2. Monte Carlo simulation

The difference between the energy loss and energy deposition was evaluated by a Monte Carlo simulation [80,81]. As discussed in Sec.2.1.1, the stopping power can be divided into two parts, which are originated in the distant and the close collisions. As for the distant collision, ($K<1/a_{TF}$), the energy loss was calculated by Eq.(A.10). The experimental value of the mean ionization energy listed in ref.[82] was adopted as the *I*-value in the calculation. The distant collision does not contribute to the electron escape because of the small energy transfer. Therefore, the energy loss due to the close collision was calculated by the Monte Carlo method. A distribution of the probability for transferring the energy, *T*, to a target electron was determined by the Mott differential cross section in Eq.(2.23), and the scattering angle, θ, was related to the energy transfer by Eq(2.25). The scattering angle in the center of mass frame, θ, was transformed to that in the laboratory frame, θ', through the relation

$$\cos^2\theta' = \frac{\gamma^2 \sin^2(\theta/2)}{1+(\gamma^2-1)\sin^2(\theta/2)}. \quad (3.3)$$

The decrease of the ion velocity was not taken into account, because the energy loss is less than 0.3 percent of the incident energy even in the case of 390 MeV Ar^{18+} ions in 200 μm Si target. When the extraporated range of the scattered electron, $R_{ex}(T)$, is larger than the distance between the collision point and the target surface, l, shown in Fig.3.11, the electron escapes from the target with energy, E_{out}, which satisfies

$$R_{ex}(E_{out}) = R_{ex}(T) - l. \quad (3.4)$$

The total energy of the escaped electron, E_{es}, was obtained by summing the energy, E_{out}, for each collision. The energy deposition of the ion was obtained by

$$\Delta E_D = \Delta E_L - E_{es}, \quad (3.5)$$

where ΔE_L is the energy loss.

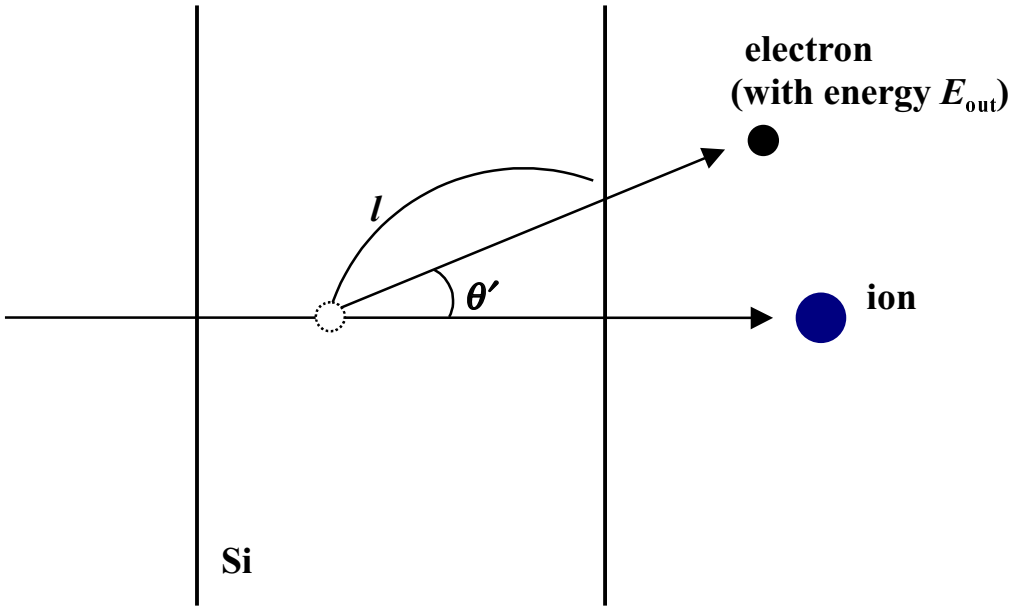

Fig.3.11 Energetic electron escaped from the target.

3.3.3. Results and discussion

Simulated spectra of the energy loss (thin line) and the energy deposition (thick line) for 390 MeV/u Ar^{18+} ions in Si targets with thicknesses of 1.0, 19.4 and 200 μm are shown in Fig.3.12. The abscissa is the energy (loss and deposition) divided by the target thickness. There are some interesting features in these results. In the case of 1.0 μm target, both the energy loss and the energy deposition spectra have a tail in the higher energy side, which have a feature of the Landau distribution. The energy loss remains a high energy tail for 19.4 μm target, but the energy deposition gets more like symmetric Gaussian shape. In the case of 200 μm, both distributions look symmetric. These sequential changes of the energy loss distribution more or less correspond to the variation of the parameter, κ, defined in Eq.(2.33), which is 0.012, 0.23 and 2.3 for 1.0, 19.4 and 200 μm target, respectively. As for the energy deposition distribution, the

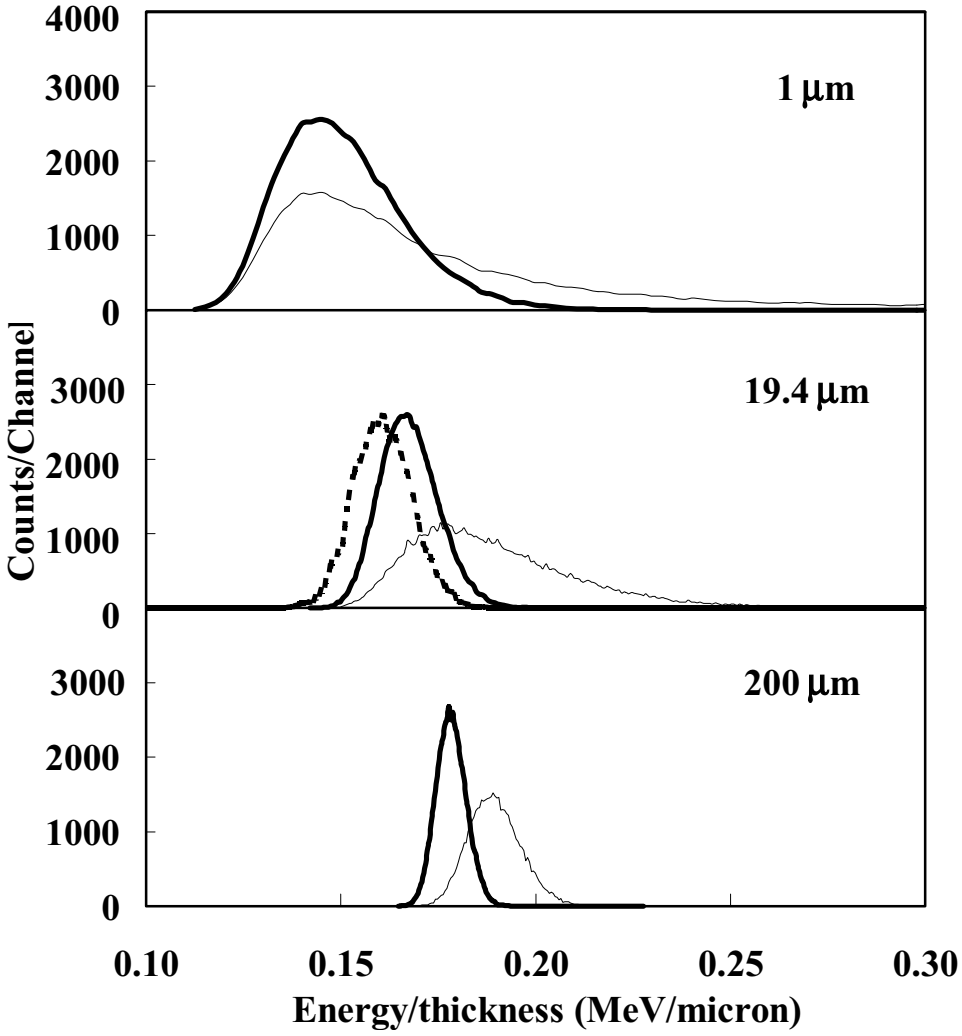

Fig.3.12 Simulated spectra of energy loss (thin line) and energy deposition (thick line) of 390 MeV/u Ar^{17+} incidence in Si target with the thicknesses of 1, 19.4 and 200 μm. The dotted line represents the experimental energy deposition.

maximum energy transfer, T_{max}, in Eq.(2.33) has to be replaced with an effective energy transfer, T^*_{max}, because the electrons with the energy close to T_{max} escape from the target. The effective maximum energy transfer, T^*_{max}, is estimated from the extrapolated range of electron, $R_{ex}(T^*_{max})$, which should be equal to the target thickness. Replaced parameters, $\kappa^* = \xi / T^*_{max}$, for 1.0, 19.4 and 200 μm cases are 1.1, 3.5, and 9.4, respectively. Therefore, the energy deposition spectrum for 19.4 μm case is seen to be more like the Gaussian shape, which is different from the energy loss spectrum at the same thickness. The dotted line represents the experimental energy deposition. The peak position of the simulated spectrum is slightly different from the experimental one, however, the shape and width reproduce the experimental result very well.

3.3.4. Δ*E*-counter for relativistic particle with high precision

Fig.3.13 shows the target thickness dependence of simulated $\sigma_L/\Delta E_L$ and $\sigma_D/\Delta E_D$, where σ_L and σ_D are standard deviations of the energy deposition and the energy loss distributions, respectively. Both $\sigma_L/\Delta E_L$ and $\sigma_D/\Delta E_D$ become smaller with the increase of the target thickness. In the thinner region than 20 μm, $\sigma_L/\Delta E_L$ increases drastically. On the other hand, $\sigma_D/\Delta E_D$ does not show a drastic increase in the thinner region. If the SSD is adopted as a Δ*E*-counter, *e.g.*, for the particle identification from the energy deposition, the relative resolution is determined by $\sigma_D/\Delta E_D$. Fig.3.13 indicates that

1) The relative energy resolution is better for larger SSD thickness, when the energy loss of the incident particle can be neglected.
2) Even in the case of thin SSD, however, the resolution is comparatively high for particles with relativistic energies.

The SSD thickness which gives a comparatively high resolution, *i.e.*, whose energy deposition distribution becomes the Gaussian shape, is estimated from the value of parameter κ^*. Fig.3.14 shows the thickness dependence of parameters κ and κ^* for 390 MeV/u Ar ions in a Si traget. It suggests that the SSD with several 10 μm thichness ($\kappa^* >> 1$) can be used as a high resolution Δ*E*-counter, although the energy loss distribution has a higher energy tail, *i.e.* $\kappa << 1$.

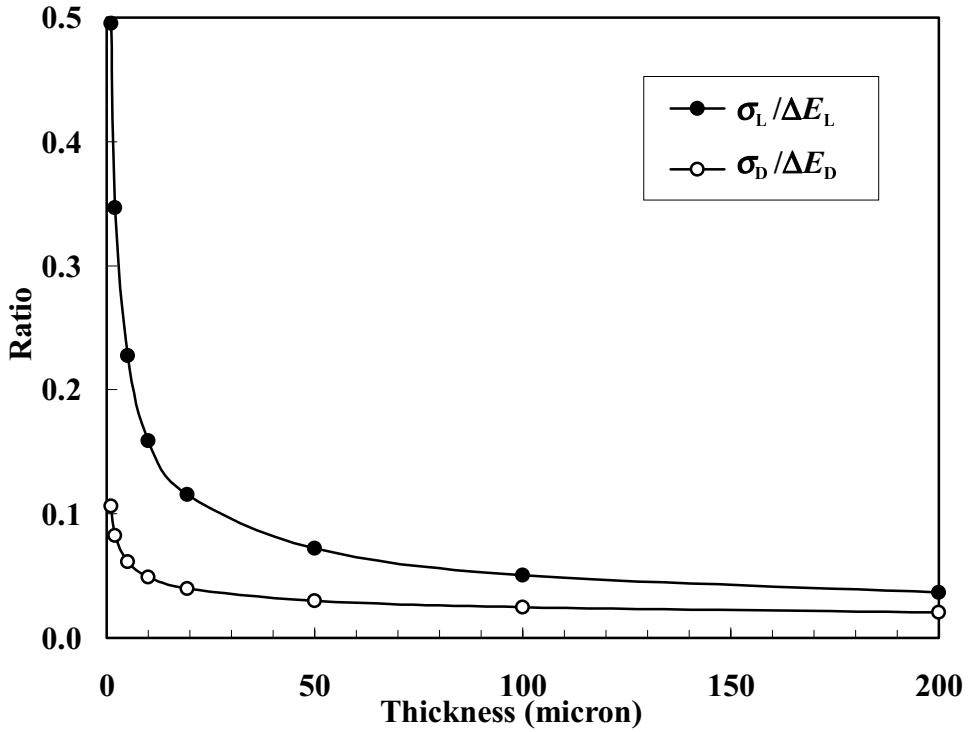

Fig.3.13 Ratio of the standard deviation, σ_L, to the energy loss, ΔE_L, and that of the standard deviation, σ_D, to the energy deposition, ΔE_D, as a function of the target (Si) thickness for 390 MeV/u Ar^{18+} ions.

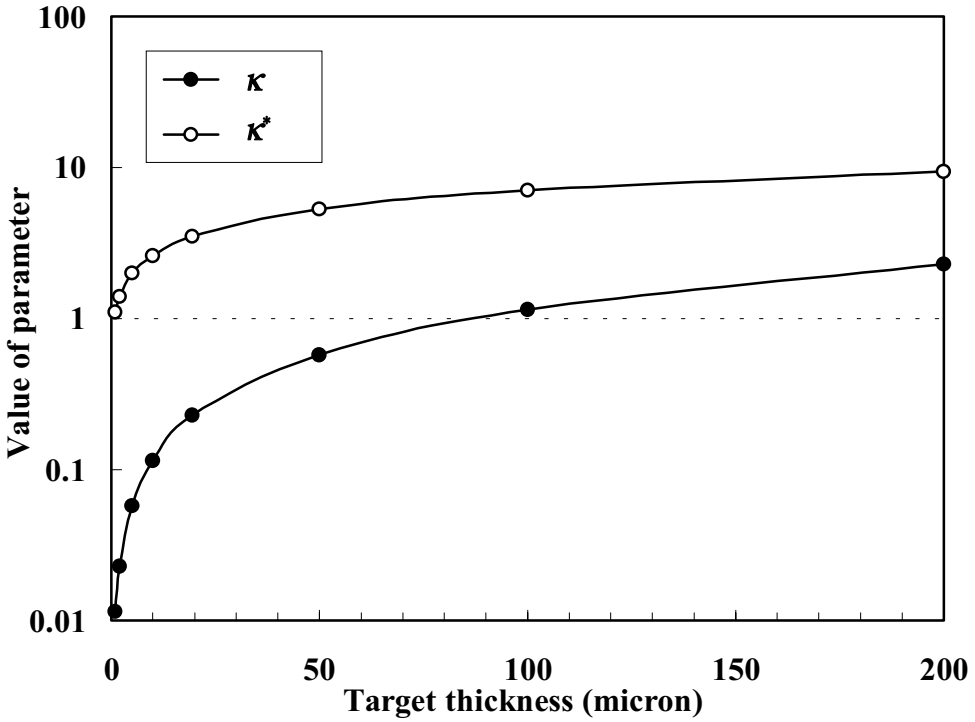

Fig.3.14 Parameters, κ and κ^*, as functions of the target thickness.

3.4. Channeling case

3.4.1. Determination of crystal orientation

The crystal orientation was determined with a precision of 1° by X-ray diffraction in advance, and the quality of the crystal was evaluated through the X-ray topography. The crystal (SSD) mounted on the goniometer was rotated on two orthogonal axes, while the energy deposition and the charge state distribution were monited. Under the channeling condition, the energy deposition shifted to lower side, and the survived Ar^{17+} ions increased. An example of the fraction of Ar^{17+} ions as a function of the tilt angle is shown in Fig.3.15. Several peaks are seen which correspond to planar channeling conditions. Scanned paths in the experiment are indicated by dotted lines with the arrow in Fig.3.16. Circles are positions of planar channeling conditions found in the scans. The thick line represents the scan shown in Fig.3.15. This shows how several planar directions were found and the [110] axial direction was determined.

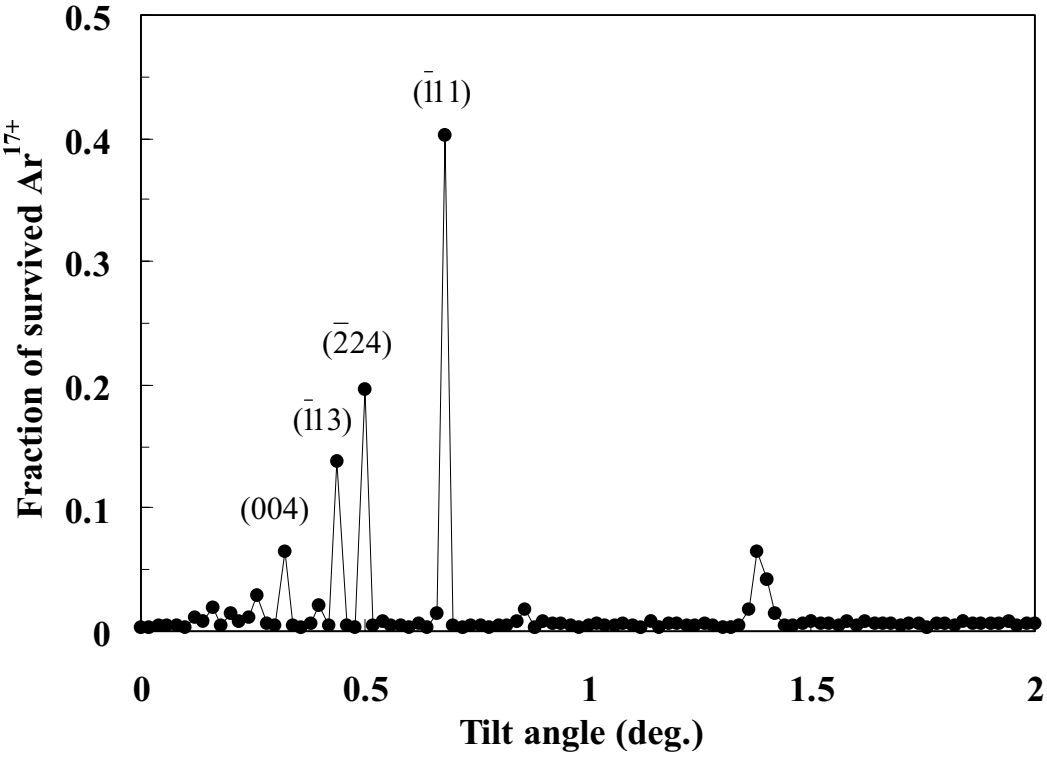

Fig.3.15 Fraction of survived Ar^{17+} ions as a function of the tilt angle θ.

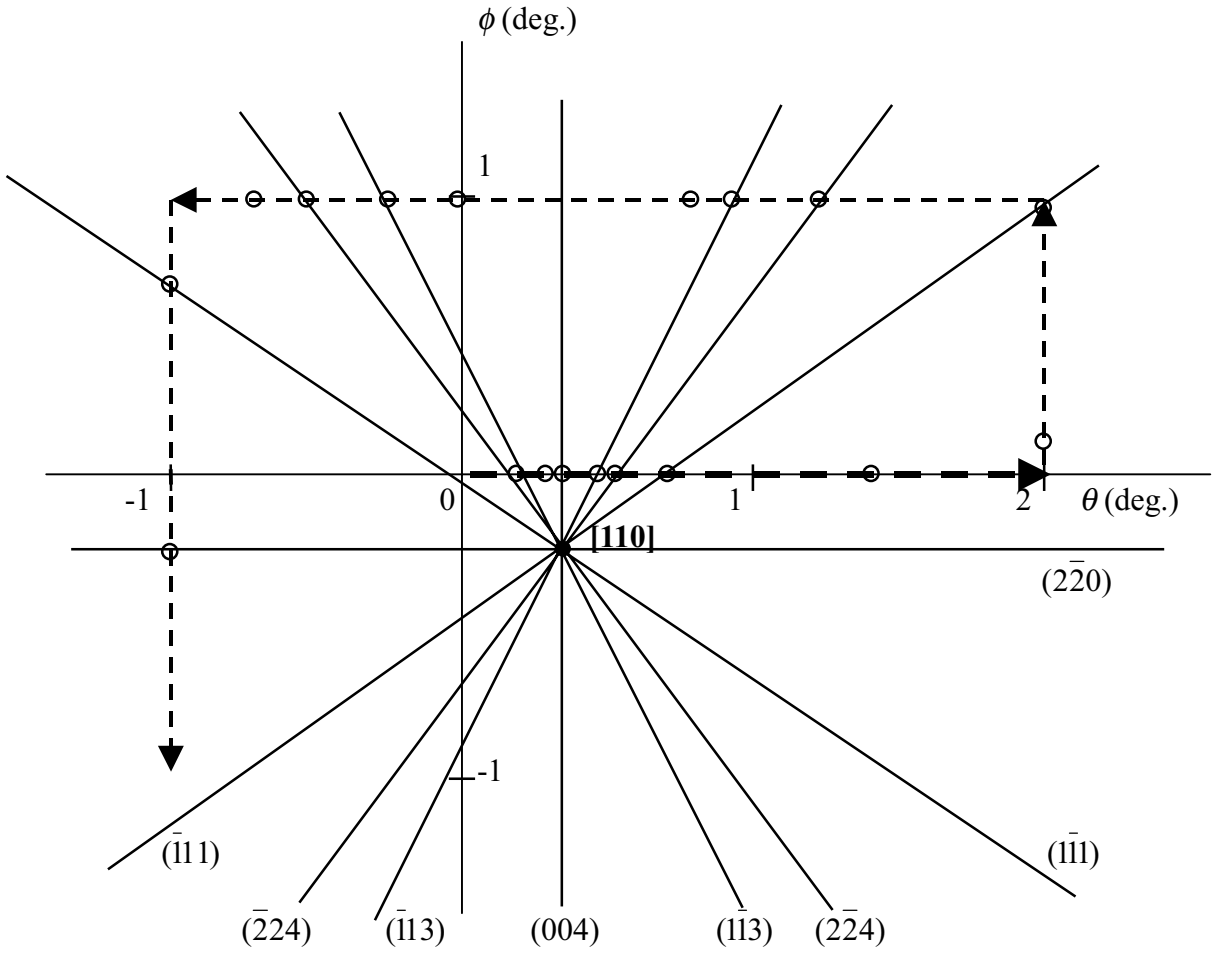

Fig.3.16 Direction of the [110] axis and several planes of Si crystal. The dotted lines with the arrow represent scanned paths. The thick line is the scan shown in Fig.3.15. The circles are positions under planar channeling conditions.

3.4.2. Angular distribution of channeled ions

The beam spot profiles of 290 MeV/u C^{6+} ions transmitted through 524 μm Si crystal for random and the [110] axial channeling cases are shown in Fig.3.17. From the spot size measured by the PSD and the geometrical configuration, the angular spreading due to passage through the target was estimated to be 1.4 mrad (HWHM) for random incidence. Assuming that the minimum impact parameter, b_{min}, is about the nuclear size, and the maximum impact parameter, $b_{max} \sim a_{TF}$, the angular straggling evaluated from Eq.(2.47) is ~1.5 mad. The measured value agrees with the theoretical value. On the contrary, the [110] axial channeling condition does not show any significant angular broadening, because the probability of large angle scattering is quite small.

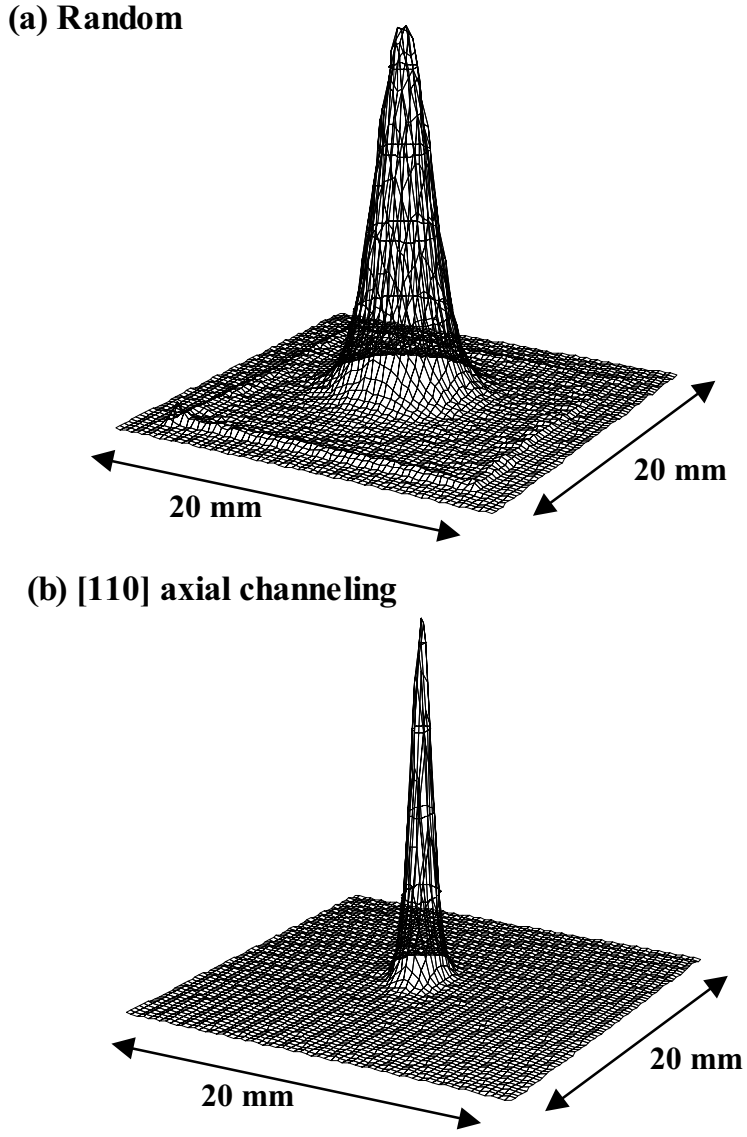

Fig.3.17 2D-spot size of 290 MeV/u C^{6+} ions at PSD for (a) random incidence and (b) under the [110] axial channeling condition.

3.4.3. Energy deposition under channeling condition

The energy depositions of 290 MeV/u C^{6+} ions and 390 MeV/u Ar^{17+} ions channeled in a Si crystal were measured in coincidence with the exit charge state. The energy deposition spectra of 290 MeV/u C^{6+} ions in 524 μm target for random incidence and [110] axial and several planar channelings are shown in Fig.3.18. In this energy region, all the exit charge state is 6+, because the electron capture cross section is negligibly small. The abscissa is normalized to the mean energy deposition for a random incidence. Under the [110] axial channeling condition, the peak of the energy deposition was reduced to 5.8 MeV from that for random incidence, which was 11.8 MeV. A small peak in the higher energy region corresponds to the non-channeled component. Under the (004), (220) and $(1\bar{1}1)$ planar channeling conditions, the energy deposition spectrum also has two components corresponding to channeled and non-channeled. The inter-planar distances, d_p, of the (004), $(2\bar{2}0)$ and $(1\bar{1}1)$ planes are 1.36, 1.92 and 3.14 Å, respectively. The peak positions for the channeled component were 7.7, 6.6 and 5.2 MeV for (004), (220) and $(1\bar{1}1)$ planar channeling cases, respectively, and the peak shape depended on the channel plane.

In the case of 390 MeV/u Ar^{17+} ions in 94.7 μm target, almost all ions were ionized for random incidence, because the target thickness is much larger than the ionization mean-free-path of 3.3 μm. Under the (220) planar channeling condition, the fraction of ionized Ar^{18+} ions was about 80 percent, and about 20 percent of incident Ar^{17+} ions maintained the initial charge states throughout the passage. The energy deposition spectra for final charge states of 18+ and 17+ are shown in Fig.3.19. The spectrum for Ar^{18+} ions (Fig.3.19a) also consists of two components. The dotted line shows the energy deposition spectrum for random incident case, which has a peak at 16.4 MeV. It is remarkable that the peak position of non-channeled component under the channeling condition is 7 percent higher than that for random incidence. This can be attributed to "quasi-channeled ions", which spend quite a long time near the channel wall, where the averaged electron density along the trajectory becomes larger than the mean electron density of the target. Therefore, the energy loss (also energy deposition) becomes larger than that for random incidence. The fraction of non-channeled component is considerably smaller than the case of C^{6+} ions. This can be attributed to the thinner crystal, which gives the channeled ions less chances for de-channeling. A small difference of the beam angular divergence between C (~0.15 mrad) and Ar (~0.12 mrad) can be another reason for changing the fraction of non-channeled component. On the other hand, the spectrum for Ar^{17+} ions (Fig.3.19b) has only the channeled component. It means that only the ions which have passed through near the channel center can keep their incident charge state (*i.e.*, charge-frozen). The peak position is ~10 percent smaller compared with that of channeled component for Ar^{18+} case, because the stopping power is proportional to the square of the effective charge of the projectile, Z_{eff}, and the trajectory of Ar^{17+} can concentrate more around the channel center. In the case of random incidence with 4.1 μm Si traget, Z_{eff} for charge-frozen Ar^{17+} is 17.36 [81]. For the best channeled ions, Z_{eff} is expected to be closer to 17, because the distant collision is more dominant compared with the random case. The reduction of energy deposition of best channeled Ar^{17+} ions from that of Ar^{18+} ions is roughly estimated to $(18^2-17^2)/18^2$ = 10.8 percent, which agrees with the experimental result.

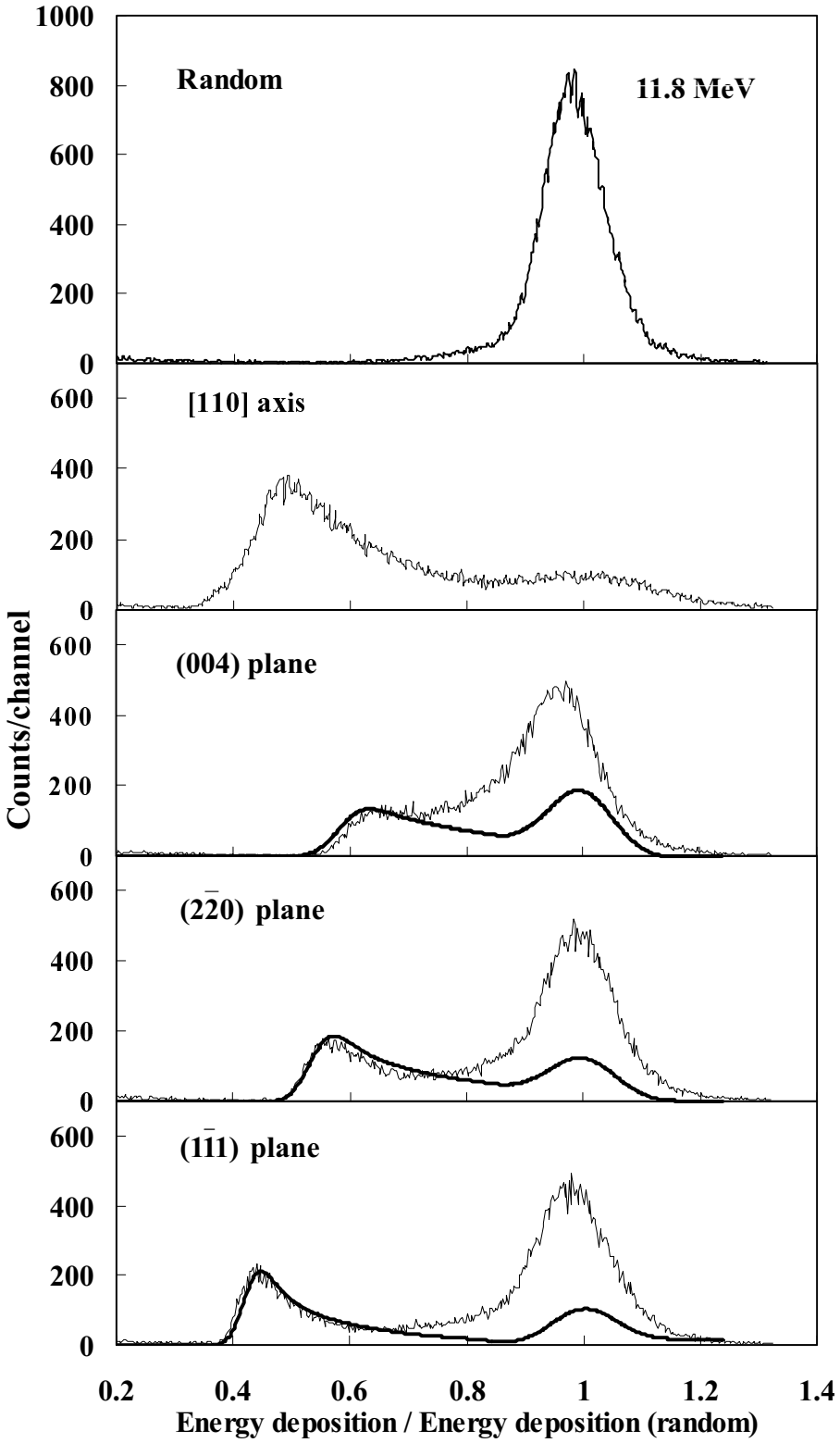

Fig.3.18 Energy deposition spectra of 290 MeV/u C^{6+} ions in 524 μm Si crystal for random incidence and several channeling cases. The thick lines indicate the results of the simulation. The abscissa is the ratio to the energy deposition for random incidence.

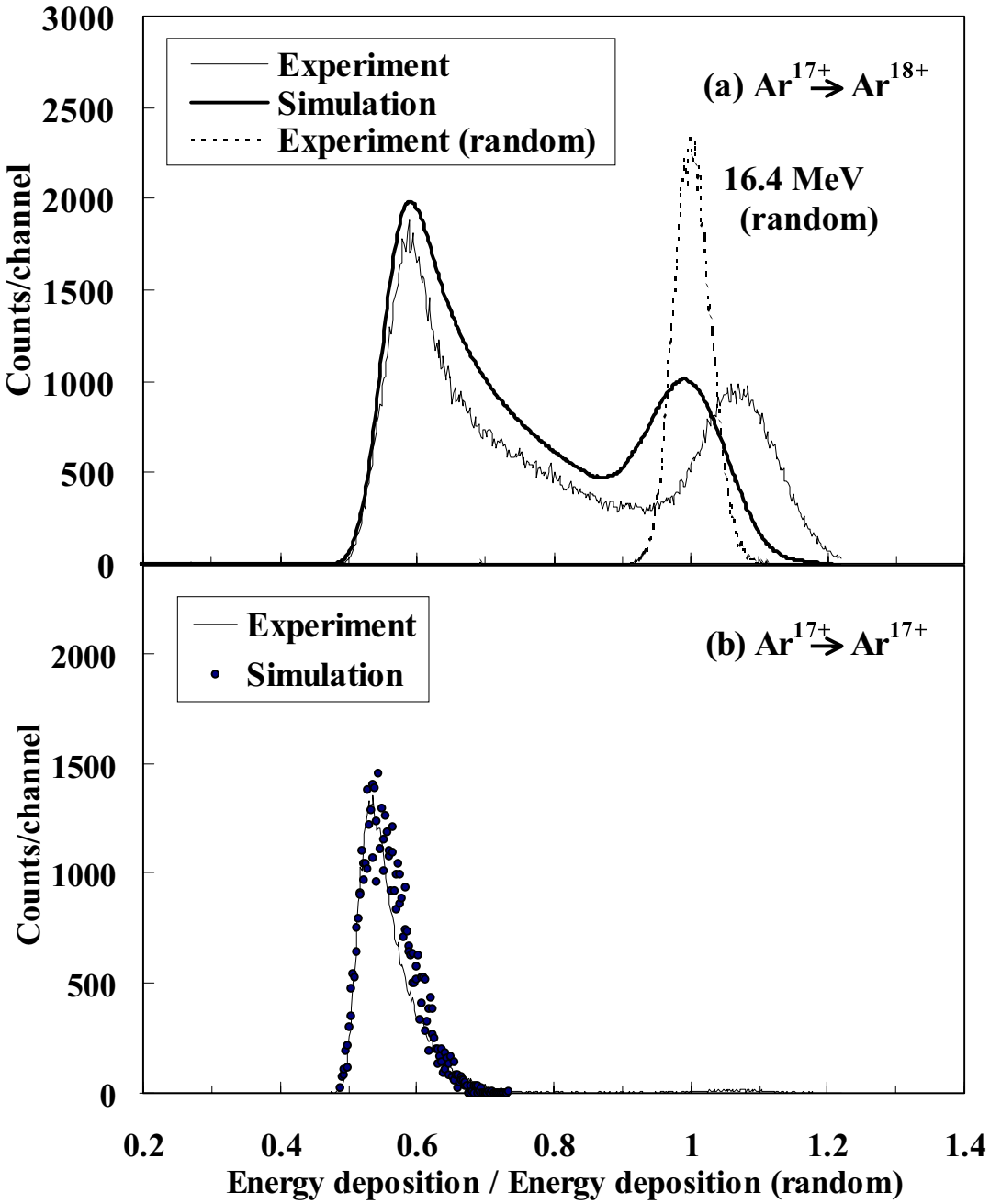

Fig.3.19 Energy deposition spectra for 390 MeV/u Ar^{17+} ions under (220) planar channeling condition in 94.7 μm Si crystal. (a) The experimental result for the exit charge of 18+ (thin line). The dotted line represents the energy deposition for random incidence. The thick line is the result of the simulation. (b) The experimental result for the exit charge of 17+. The closed circles show the result of the Monte Carlo simulation. The abscissa is a ratio to the energy deposition for random incidence.

3.4.4. Simulation of energy deposition under channeling condition

The energy deposition of the planar channeled ion depends on the oscillation amplitude. To obtain a relation between the energy deposition and the oscillation amplitude, the energy depositions of channeled ions were simulated by calculating the local electron density along the ion trajectory, and the results were compared with the experimental energy deposition. A flow chart of the simulation is given in Fig.3.20. The calculation is based on the Lindhard's formula in Eq.(2.78), which consists of the distant and the close collision parts. The stopping power was divided into two parts by a momentum transfer,

$$\hbar K_0 = f\hbar/a_{\mathrm{TF}}, \tag{3.6}$$

where f is a fitting parameter. The formula of the local stopping power for channeled ions is expressed as

$$S(x) = \frac{4\pi e^4}{m\upsilon^2}\left[q_1^2 Z_2 N\left(\ln\frac{\hbar K_0 \upsilon\gamma}{I} - \frac{\beta^2}{2} \right) + Z_1^2 n_{\mathrm{e}}(x)\left(\ln\frac{2m\upsilon\gamma}{\hbar K_0} - \frac{\beta^2}{2} + \frac{\pi Z_1 \alpha\beta}{2} \right)\right], \tag{3.7}$$

where q_1 is a charge of the incident ion, and $n_{\mathrm{e}}(x)$ is the local electron density. The value of $f = 1$ in this formula roughly corresponds to $\alpha_{\mathrm{c}} = 1/2$ in the Lindhard formula, *i.e.*, the contribution from the distant collision is about a half of the random stopping power (equipartition rule). The local electron density was derived from the planar potential in Eq.(2.65) using the Poisson equation. The averaged stopping power along the ion trajectory with the oscillation amplitude x_0 is obtained by

$$\overline{S}(x_0) = \frac{4}{T_{\mathrm{osc}}(x_0)}\int_0^{x_0} \frac{S(x)}{\upsilon_\perp(x)}dx, \tag{3.8}$$

where $T_{\mathrm{osc}}(x)$ is a period of the oscillation, which is given by

$$T_{\mathrm{osc}}(x_0) = 4\int_0^{x_0} \frac{dx}{\upsilon_\perp(x)}, \tag{3.9}$$

and $\upsilon_\perp(x)$ is the ion velocity perpendicular to the channel plane, which satisfies

$$\frac{\gamma}{2}M_1\upsilon_\perp^2(x) + U_{\mathrm{p}}(x) = U_{\mathrm{p}}(x_0). \tag{3.10}$$

When the target thickness, z_0, is more than several times larger than the ion path length per oscillation, $\lambda = \upsilon T(x_0)$, the total energy loss throughout the path can be written as

$$\Delta E_{\mathrm{L}}(x_0) = \overline{S}(x_0)\cdot z_0. \tag{3.11}$$

The energy deposition of channeled ions was evaluated by modifying Eq.(3.5) to,

$$\Delta E_{\mathrm{D}}(x_0) = \Delta E_{\mathrm{L}}(x_0) - \frac{\overline{n}_{\mathrm{e}}(x_0)}{NZ_2}E_{\mathrm{es}}, \tag{3.12}$$

where $\overline{n}_{\mathrm{e}}(x_0)$ is the averaged local electron density along the ion trajectory, which is given by

$$\overline{n}_{\mathrm{e}}(x_0) = \frac{4}{T_{\mathrm{osc}}(x_0)}\int_0^{x_0} \frac{n_{\mathrm{e}}(x)}{\upsilon_\perp(x)}dx. \tag{3.13}$$

The energy loss and the energy deposition were calculated for each trajectory.

The incident beam divergence was taken to be the same as the experimental condition. The ions whose nearest distance to the channel wall was smaller than the one-dimensional amplitude of the thermal lattice vibration, u_1(=0.075 Å for Si at 25°C), were treated as random incident ions, *i.e.*, the energy loss was calculated by Bethe's

formula with the linear Mott correction [83]. The de-channeling effect during the travel in the crystal was not taken into account.

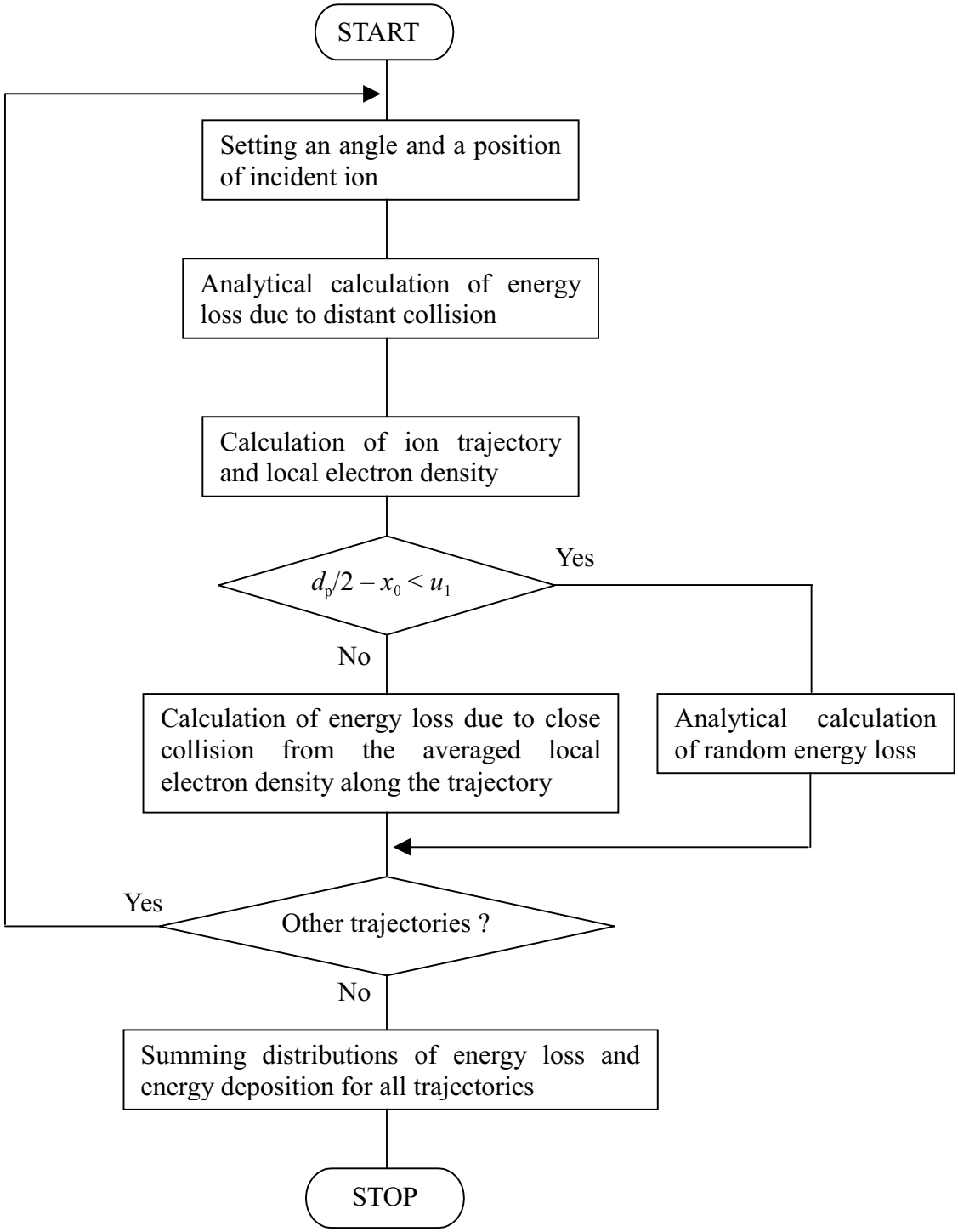

Fig.3.20 Flow chart of the simulation for energy loss and energy deposition of channeled ions.

3.4.5. Results and discussion

Simulated energy depositions for the case of C^{6+} ions with 524 μm Si crystal are shown in Fig.3.18 by thick lines. The fitting parameters, f, were selected as 0.45, 0.45 and 0.30 for (004), (220) and (111) channelings, respectively, so that the peak position of the channeled component agrees with the experimental one. It has to be noted that the (111) planar channel has two different inter-planar distances as shown Fig.3.21, which may be the reason of smaller value of f for the (111) planar channeling case. The maximum impact parameter for the close collision is given by $\sim 1/K_0$. The value of f = 0.45, *i.e.*, the cut-off momentum transfer (divided by $\hbar$) $K_0 = 0.45/a_{TF}$, means that the impact parameter for the close collision is effectively about two times larger than the case where the stopping power can be expressed by the equipartition rule. The smaller fraction of non-channeled component in the simulation compared with the experimental result can be attributed to the lack of the de-channeling effect in the simulation. The shape of the channeled component reproduced the experimental result very well for all planar channeling cases.

Simulated results for 390 MeV/u Ar^{17+} ions (220) planar channeled in 94.7 μm Si crystal are shown in Fig.3.19 by thick lines. The parameter, f = 0.45, was also used for Ar ions. When the final charge state is 18+, the simulation was performed assuming the charge state was 18+ throughout the passage. This is not a bad assumption, because the mean-free-path for ionization, λ_i ~60 μm, is smaller than the target thickness even in the channeling case, and the screening effect by the bound electron has an influence only for the distant collision. Not only the shape of the spectrum but also the fraction of non-channeled component are in good agreement with the experimental results, because the de-channeling effect is smaller than the case of C ions where the crystal was ~5.5 times thicker. In the case of Ar^{17+} ions with frozen-charge state, the representation of the energy deposition by the Gaussian shape is no longer appropriate, because these channeled ions are expected to travel near the channel center, where the number of collisions with the target electron is quite small. The value of κ in Eq.(2.33) for the best channeled ions becomes 0.29, which satisfies the condition for Landau distribution rather than the Gaussian shape. The closed circles in Fig3.19b are the result of the Monte Carlo simulation, when the incident distance of the channeled Ar^{17+} ions from the channel center is less than $d_p/4$. The distance was roughly selected, since the mean-free-path for 1s-ionization of channeled ions with the oscillation amplitude larger than $\sim d_p/4$ is smaller than the target thickness, *i.e.*, these channeled ions are regarded not to be ionized. The result of the Monte Carlo simulation shows a good agreement with experimental result.

From this calculation, a relation between the energy deposition and the oscillation amplitude of the channeled ions was obtained, which is shown in Fig.3.22a for 290 MeV/u C^{6+} ions in 524 μm Si crystal under (004), (220) and (111) planar channeling conditions. The energy deposition slowly increases with the growth of the oscillation amplitude near the channel center, and then it rises rapidly at the vicinity of the channel wall and exceeds the energy deposition for random incidence. Fig.3.22b shows local electron densities in (004), (220) and (111) planes as functions of the distance from the channel center. The relation between the energy deposition and the oscillation amplitude of (220) planar channeled Ar^{17+} and Ar^{18+} ions are shown in Fig.3.23a. A

relation between the ion path length per oscillation and the oscillation amplitude was also obtained from the simulation, and the result is shown in Fig.3.23b. The ion path length per oscillation, λ_{osc}, is ~3 μm in this case. The survived Ar^{17+} fraction as a function of the oscillation amplitude is obtained from the experimental result of the charge state distribution measured in coincidence with the energy deposition, which is shown by open circles in Fig.3.24. Here, the simulated relation between the energy deposition and the oscillation amplitude is used. The vertical and horizontal error bars were evaluated from the statistical fluctuation and the energy straggling, respectively. For the best channeled ions, about 80 percent of the incident Ar^{17+} ions survived after transmission through the 94.7 μm crystal. On the contrary, channeled ions with the oscillation amplitude larger than 0.7 Å hardly survived. The solid line shows a reesult calculated from the 1s-ionization cross section and from the target electron and nuclear (plane) densities. The local electron density was calculated with the Molière potential, and a one-dimensional nuclear density originating from the thermal lattice vibration was represented by

$$N(x) = \frac{N_0}{1+\exp\{(x-R)/a\}}. \tag{3.14}$$

A long dashed line shows the results when the nuclear distribution is represented by the Gaussian shape with the standard deviation of u_1 (=0.075 Å), and the dotted line indicates the result without nuclear impact ionization. In the present case, selecting both R and a as 0.075 Å, the calculation well reproduced the experimental result. The same nuclear effect for ionization or excitation is used in the Monte Carlo simulation on RCE in Chap.4.

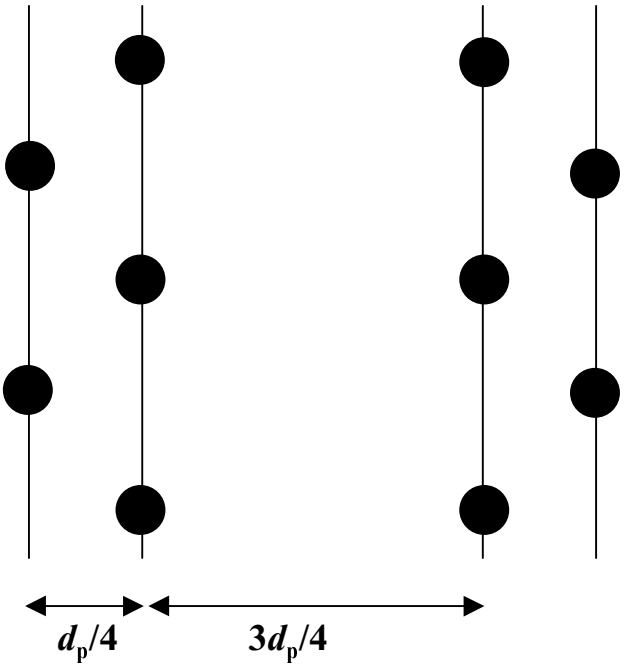

Fig.3.21 Real Si $(1\bar{1}1)$ planar channel : d_p = 3.14 Å.

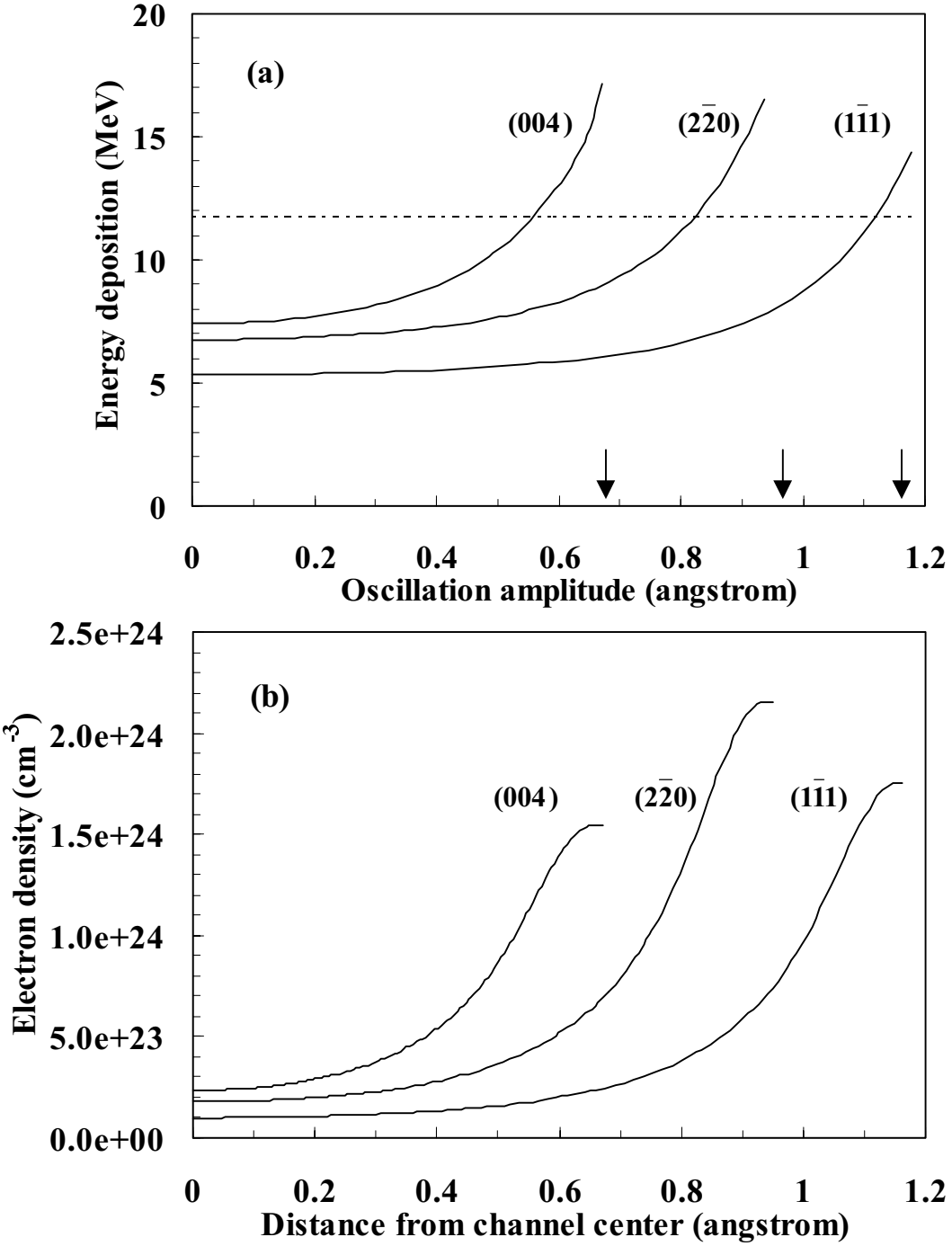

Fig.3.22 (a) Relation between the energy deposition and the oscillation amplitude of 2 90 MeV/u C^{6+} ions channeled in the (004), (220) and (111) planes. The dotted line is the experimental energy deposition for random incidence. The arrows indicate the position of the channel walls. (b) Local electron densities in (004), (220) and (111) planar channels as functions of the distance from channel center.

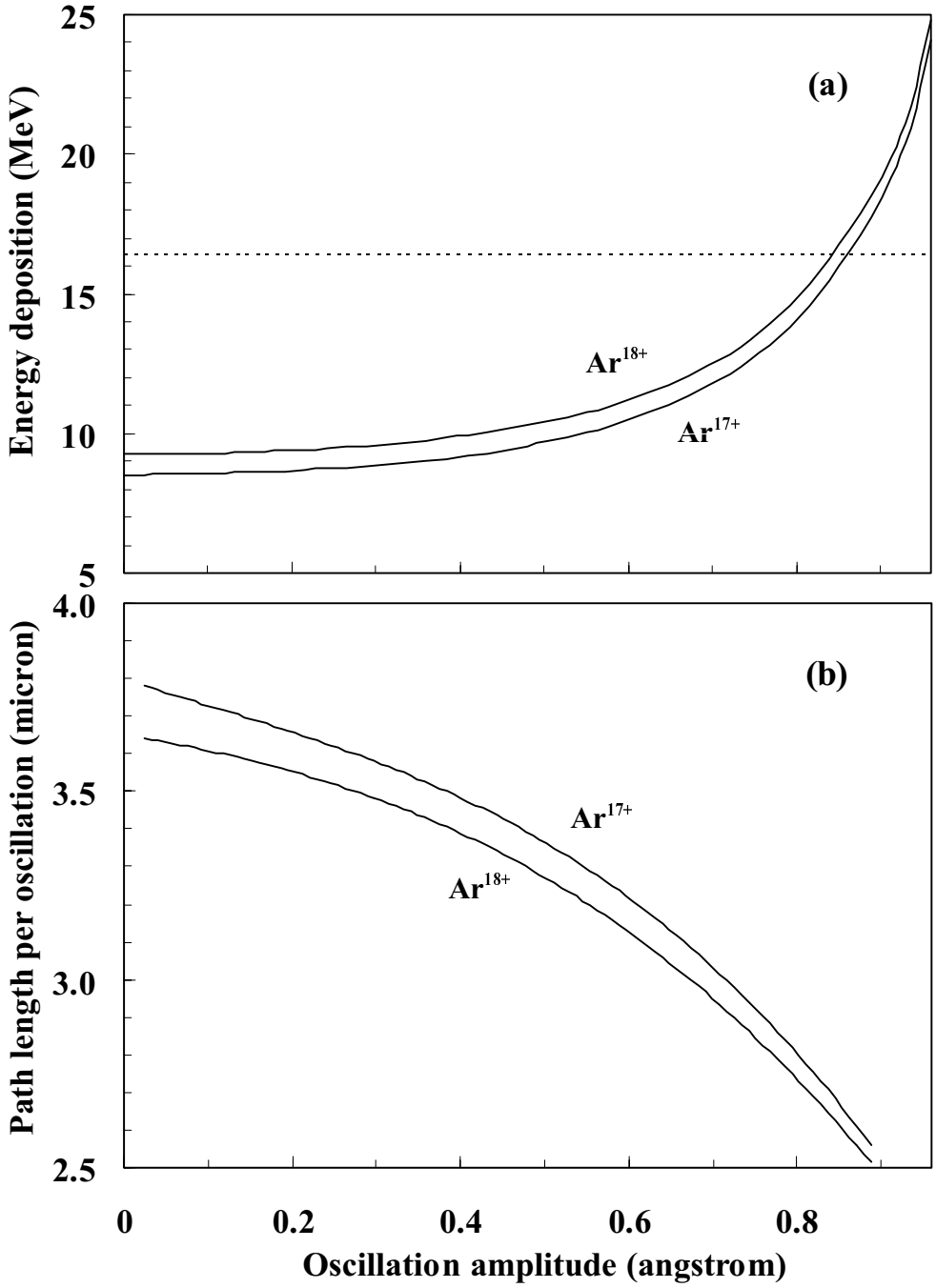

Fig.3.23 (a) Relations between the energy deposition and the oscillation amplitude for 390 MeV/u Ar^{17+} and Ar^{18+} ions channeled in the (220) plane. The dotted line is the experimental energy deposition of Ar ions with q_{in} = 17 and q_{out} = 18 for random incidence. (b) Relations between the path length of ion per oscillation and the oscillation amplitude.

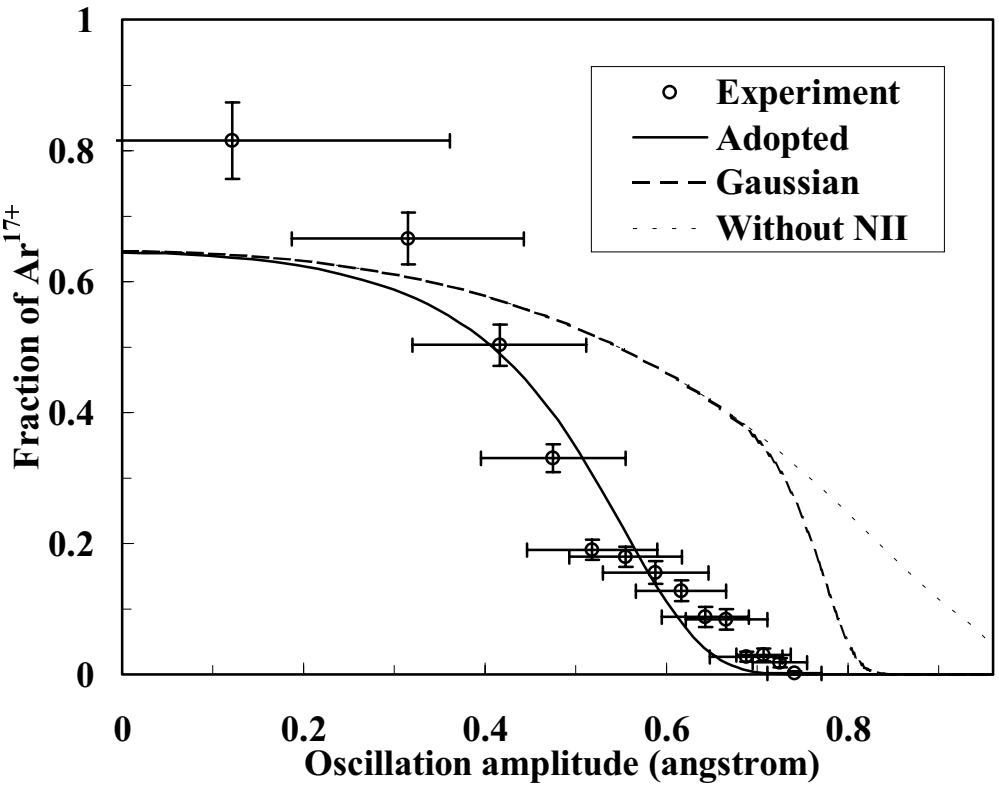

Fig.3.24 Fraction of survived Ar^{17+} ions as a function of the oscillation amplitude. The open circles indicate the experimental results. Calculated results with the nuclear distribution represented by Eq.(3.14) (solid line), by the Gaussian shape (long dashed line) and without nuclear impact ionization (dotted line) are shown.

4. Observation of resonant coherent excitation

4.1. How to observe RCE

Fig.4.1 shows ion energies, which satisfy the RCE conditions for the 1s-2p transition of hydrogen-like Ar^{17+} ions channeled in the Si (220) planes, as functions of the tilt angle from the [110] axis. The numbers in parentheses indicate indexes of the resonance, (*k*,*l*), given in Eq.(2.96). Using 390 MeV/u Ar^{17+} ions, several resonant excitations can be realized by scanning the tilt angle (dotted line). Channeled ions with bound electrons are excited or ionized primarily through collisions with target electrons as shown in Fig.4.2. Under the 1s-2p RCE condition, the relative fraction of the ionization *via* $n = 2$ states increases. Therefore, we can observe the RCE through measurements of the charge state distribution of transmitted ions and the yield of convoy electrons. [9,18]

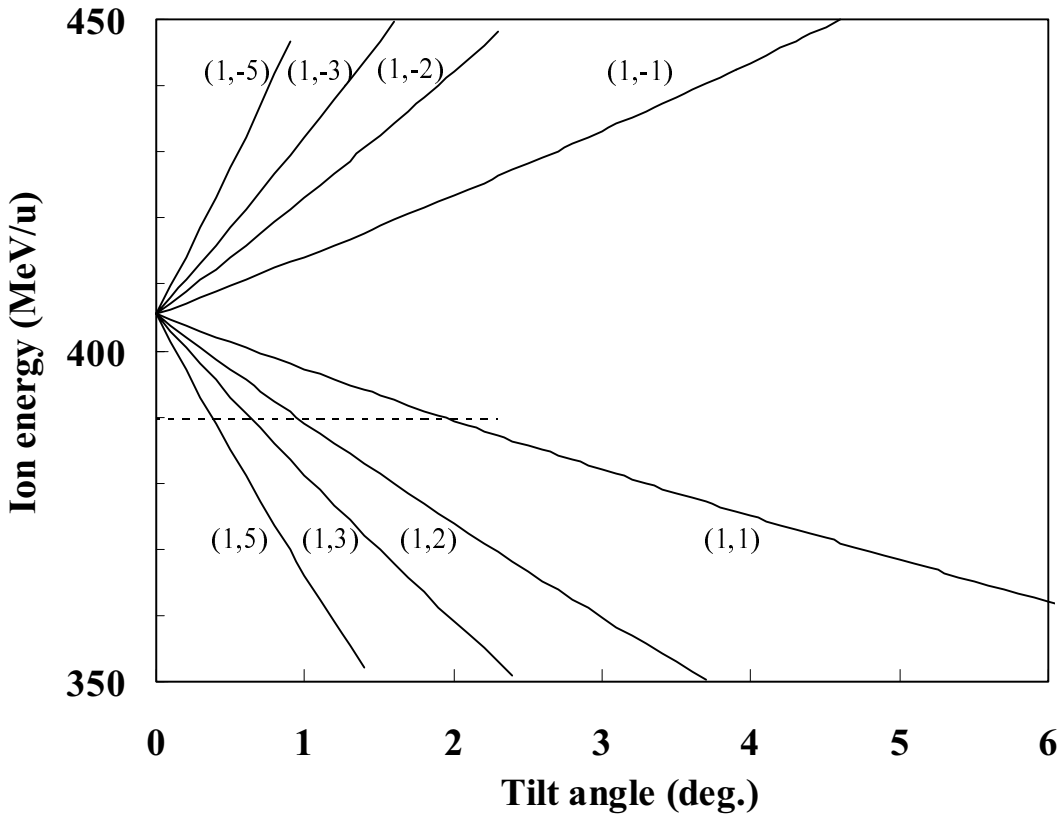

Fig.4.1 Ion energies, which satisfy the 1s-2p RCE condition for (220) planar channeled Ar^{17+} ions as functions of the tilt angle from [110] axis. The numbers in parentheses mean the indexes of the resonance. The dotted line indicates the scan in the present experiment.

The electrons excited to the n = 2 states have another decay cannel, which is the de-excitation accompanied by the X-ray emission. In the case of Ar^{17+} ion, the 2p-1s transition energy is ~3.3 keV, and the wavelength of the corresponding X-ray, λ, is ~3.8×10^{-8} cm. The mean orbital radius of the 2p electron of Ar^{17+} ion, r, is ~1.6×10^{-9} cm. In this case, $k \cdot r = (2\pi r/\lambda)$, is ~0.2 < 1, which indicates that the dipole (E1) transition is dominant. The radiative lifetime of the 2p state of Ar^{17+} is 1.53×10^{-14} s [84], which corresponds to the ion path length of 4.6 μm in the present case. When the quantization axis is selected as x-axis, the angular distribution of the X-ray emission for E1 transition from $2p_x$ is given by

$$\frac{dI}{d\Omega} = \frac{3}{8\pi}\sin^2\theta, \tag{4.1}$$

where θ is the angle from the quantization axis. Each n = 2 state, which is named Levels 1 – 4 in Sec.2.3, has different fractions of $2p_x$, $2p_y$ and $2p_z$ components (Fig.2.16). Therefore, an anisotropy of the X-ray emission from the ions excited to the level in which $2p_x$, $2p_y$ and $2p_z$ components are not equally contained is expected to be observed [20]. On the other hand, X-rays from 2s state can not be observed although the state decays by two-photon dipole (2E1) transition with a lifetime of 3.5 ns [85], because the ion path length corresponding to the lifetime is much larger than the mean-free-path for 2s-ionization. Accordingly, the measurement of the de-excitation X-rays gives us not only an evidence of the RCE but also a more detailed understanding of the n = 2 excited states of the channeled ions, for instance, whether the excited ions maintain their initial composition of 2s, $2p_x$, $2p_y$ and $2p_z$ components or not.

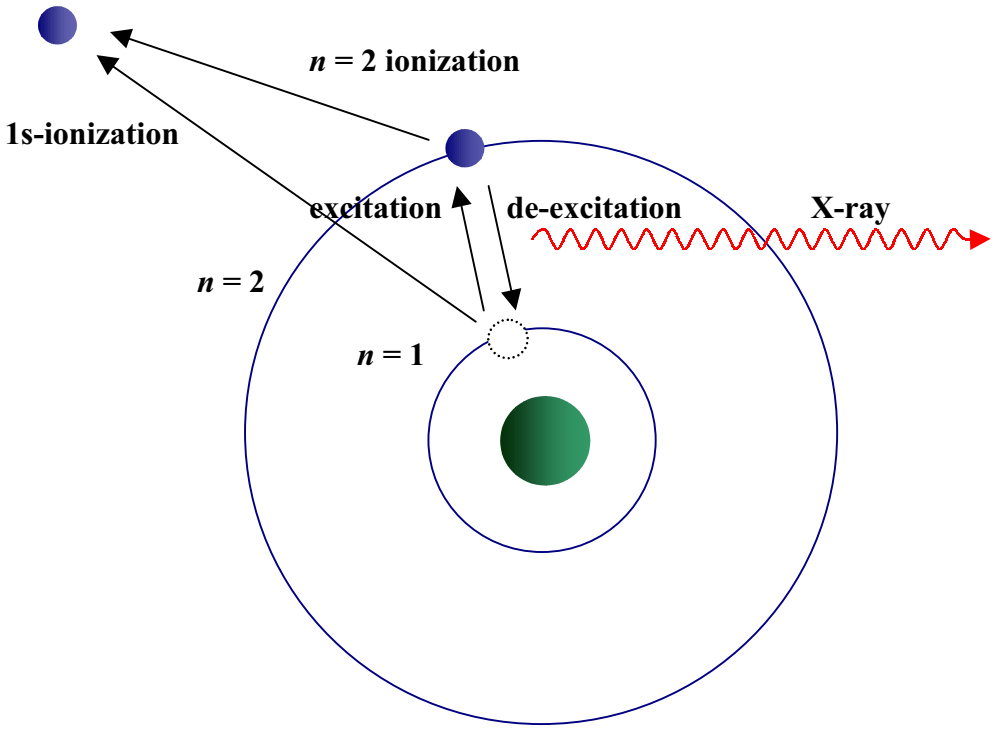

Fig.4.2 Processes of the hydrogen-like ion traveling in the target.

4.2. Experimental setup

A schematic drawing of experimental setup for the RCE observation through measurement of the charge state of transmitted ions and the convoy electrons is given in Fig.4.3. A 390 MeV/u Ar^{17+} ion beam was injected into a Si crystal mounted on the three-axis goniometer. The transmitted ions were charge-separated by a magnet, and were detected by a 2D-PSD. The convoy electrons were bent by a magnetic analyzer, and were detected by an SSD with a depletion layer of 5 mm. The range of convoy electron (214 keV) is about 200 μm in aluminum. Two aluminum slits with the thickness of 5 mm and with the inner-diameter of 5 mm were placed at the exit of the magnetic analyzer and in front of the SSD. The electrons within the forward angle of 1° were detected by the SSD. The momentum spectrum of convoy electrons was obtained by scanning the magnetic field of the analyzer. A typical energy spectrum detected by the SSD for a fixed magnetic field is shown in Fig.4.4. Because the SSD is energy sensitive, it is useful to select the signal of the convoy electrons from the energetic background electrons and/or γ-rays.

A schematic drawing of experimental setup for the RCE observation through the measurement of the de-excitation X-rays is given in Fig.4.5. In the X-ray measurement, the $\mathrm{Si}(220)$ plane is kept horizontal, and the angle θ defined in Fig.3.3 is altered. Two Si(Li)-detectors were placed at 41° from the beam direction on the horizontal and vertical planes, which are named "Detector (H)" and "Detector (V)" hereafter. The angle 41° in the laboratory frame corresponds to 84.4° in the projectile frame, and the de-excitation X-ray from $2p_z$ can be measured with almost the maximum intensity as well as that from $2p_x$. Here, *x* and *z*-axes are defined as perpendicular to the channel plane and parallel to the beam direction, respectively. Geometrical efficiencies for the detectors were $\sim 1.8\times10^{-4}$. Aluminum foils with the thickness of 2 μm were located in front of the detectors to reduce the background in the lower energy region. Transmitted fraction of de-excitation X-rays from Ar ions through the aluminum foil was about 90 percent. To monitor the beam intensity, another Si(Li) detector was placed with a Cu-foil of 50 μm thickness at the end of the beam line, and Cu K_α X-rays were detected. The maximum beam intensity for measuring the charge state distribution was $\sim 10^3$ particle/sec, because the 2D-PSD did not work for higher beam intensity. On the other hand, measurement of X-rays or convoy electrons needed the beam intensity of $\sim 10^6$ particle/sec. The relation between the number of particles detected by the 2D-PSD and the intensity of Cu K_α X-rays were obtained in advance.

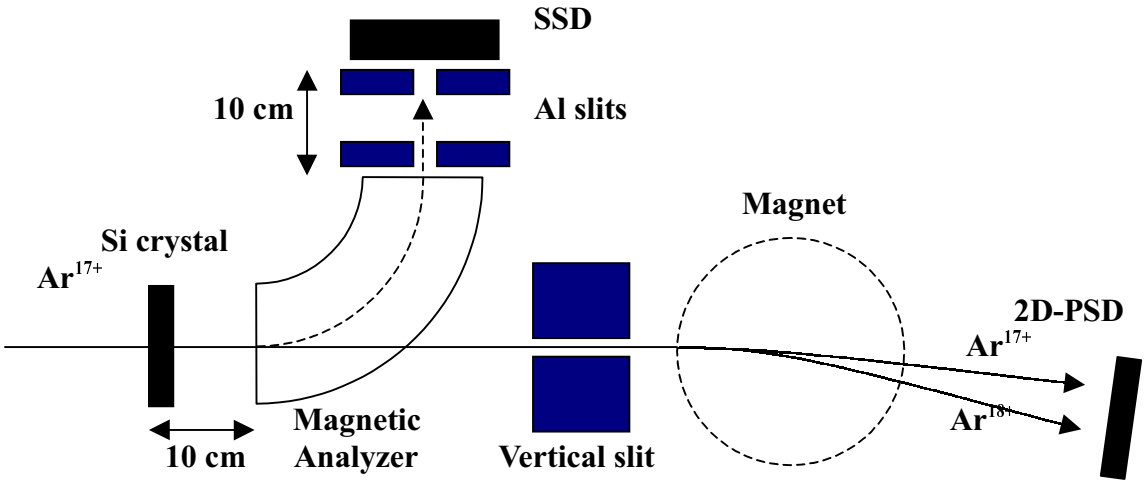

Fig.4.3 Schematic drawing of experimental setup for RCE observation through the measurement of convoy electrons.

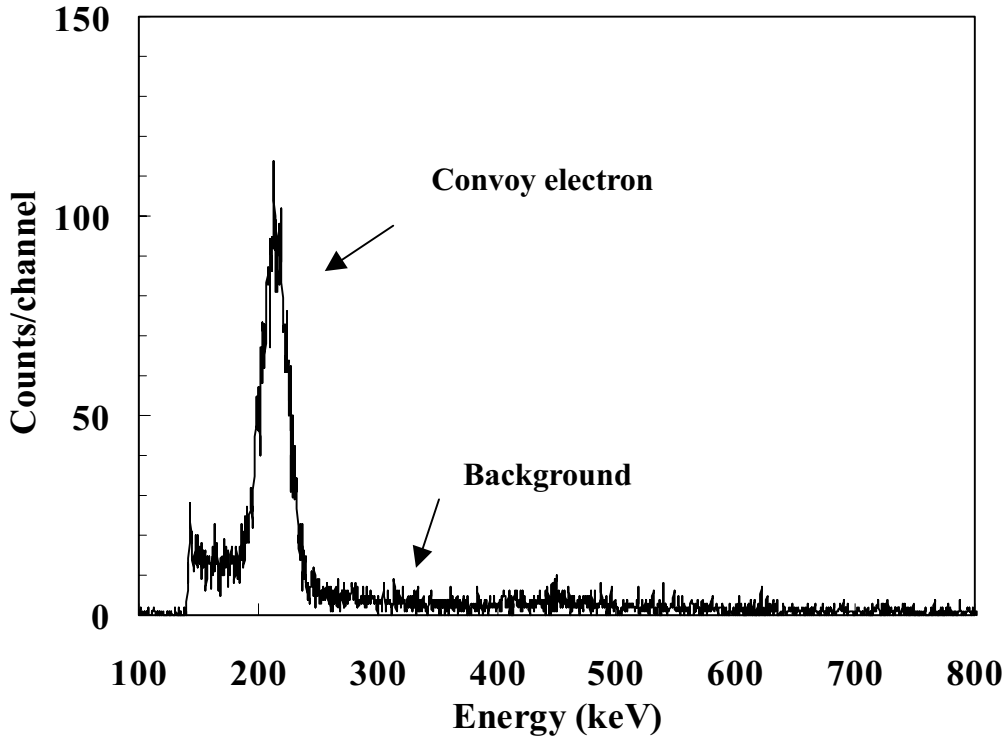

Fig.4.4 Typical energy spectrum detected by the SSD for a fixed magnetic field of the analyzer.

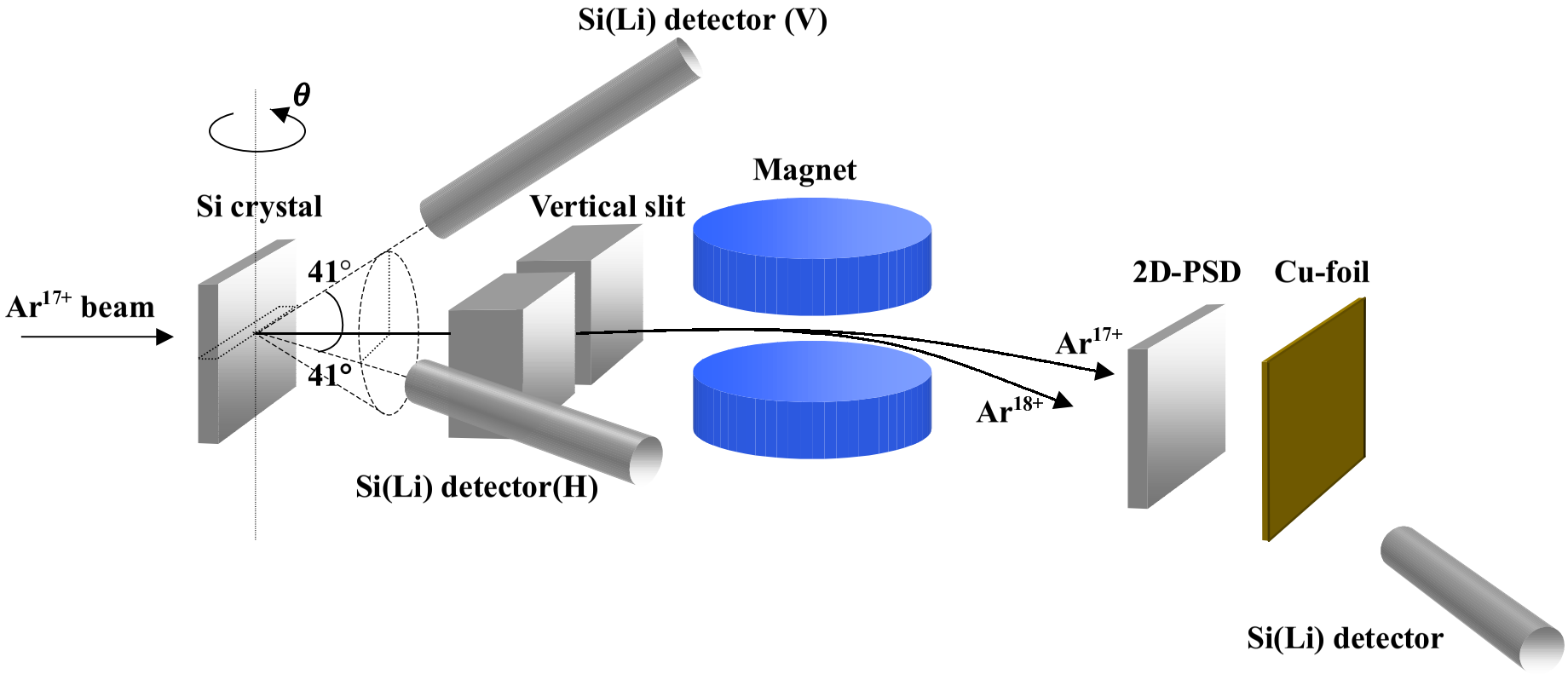

Fig.4.5 Schematic drawing of experimental setup for measuring the de-excitation X-rays

4.3. Measurement of charge state distribution

4.3.1. RCE profile for charge state distribution

The fractions of Ar^{18+} transmitted through 78.5 μm Si crystal for (004) planar channeling case, and 94.7 μm Si crystal for (004), (220) and (1̄11) planar channeling cases are shown in Fig.4.6 as functions of the tilt angle from the [110] axis on the above channel plane. Sharp resonance peaks corresponding to (k,l) = (1,1), (1,2), (1,3), (1,5), (1,6) and (k,l) = (1,1), (1,3), (1,5) were observed for (220) and (1̄11) planar channelings, respectively. Resonance peaks corresponding to (k,l) = (1,4) for (220) planar case and (k,l) = (1,2) and (1,4) for (1̄11) planar case were absent because of the selection rule discussed in Sec.2.3.2. In the case of (004) planar channeling, all resonance peaks from (k,l) = (1,1) to (1,6) were observed as expected.

4.3.2. Fine structure of (k,l) = (1,1) resonance

Results of the fine scan around the (k,l) = (1,1) resonance for the (220) planar channeling with 94.7 and 21 μm crystals are shown in Fig.4.7. The lower scale is the tilt angle from the [110] axis, and the upper scale is the transition energy corresponding to the tilt angle by Eq.(2.96). In the case of 94.7 μm crystal (SSD), the fraction of ionized Ar^{18+} was ~80 percent for off-resonance, and increased to ~95 percent under the resonance condition. The resonance was split into two peaks because of the spin-orbit interaction. Dotted lines in the figure indicate the transition energies of hydrogen-like Ar from 1s to n = 2 (J = 1/2 and J = 3/2) states in vacuum, which are 3.3182 and 3.3230 keV, respectively. The J = 1/2 peak has a doublet structure originating in the Stark effect by the static crystal field.

In the present experiment, the energy deposition of the ion to the target crystal (SSD) was also measured in coincidence with its charge state. Survived Ar^{17+} fraction after the transmission through the crystal with the thickness, z_0, is a function of the tilt angle, θ, and the energy deposition, ΔE, *i.e.*, $f^{17}(\theta, \Delta E, z_0)$. Fig.4.8 shows a contour map of $f^{17}(\theta, \Delta E, z_0)$. The abscissa and the ordinate are the tilt angle and the energy deposition, respectively. The left scale of the ordinate is the oscillation amplitude corresponding to the energy deposition through the simulated results in Sec.3.4.5. Channeled ions experience incoherent ionization, incoherent excitation/de-excitation, and coherent excitation/de-excitation. Accordingly, the fraction, $f^{17}(\theta, \Delta E, z_0)$, reflects the contributions of incoherent ionization by the target electron impact as well as the ionization subsequent to the coherent excitation. To describe the atomic process of the channeled ion rigorously, the time dependent Schrödinger equation including the coherent and incoherent processes [14] should be solved. However, in this section, a simple rate equation was preliminarily adopted to extract the ionized fraction through the RCE process from the experimental result [86], which is

$$\frac{df^{17}(\theta, \Delta E, z)}{dz} = -(k_R + k_i) f^{17}(\theta, \Delta E, z), \tag{4.2}$$

where k_R and k_i are ionization rates per unit length through the RCE and through only incoherent processes, respectively. For off-resonance case, *i.e.*, $\theta = \theta_{off}$, k_R becomes to 0. The ionization rate, k_i, is considered to be constant except when the ions get off the channeling condition. Solving Eq.(4.2), survived Ar^{17+} fractions after transmission

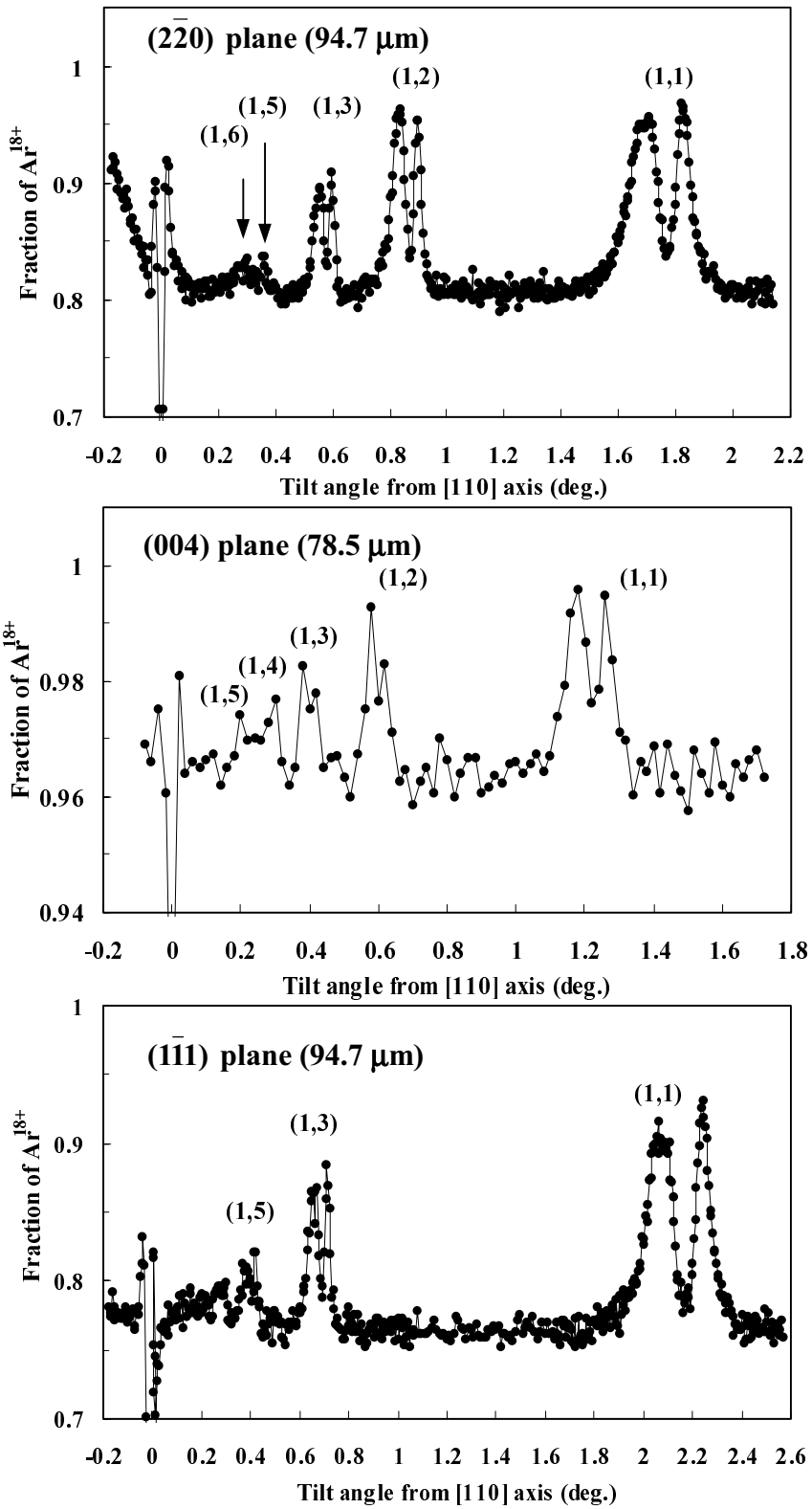

Fig.4.6 Fraction of ionized Ar^{18+} ions as a function of the tilt angle from [110] axis under (220), (004) and (1$\bar{1}$1) planar channeling conditions.

through the crystal under the RCE and off-resonance conditions are given by

$$f^{17}(\theta, \Delta E, z_0) = e^{-(k_R + k_i) z_0} \tag{4.3}$$

and

$$f^{17}(\theta_{off}, \Delta E, z_0) = e^{-k_i z_0}, \tag{4.4}$$

respectively. Here, an ionized fraction only through the RCE process, *i.e.*, without the incoherent ionization from the ground state, is introduced to evaluate the subsequent ionized fraction after the RCE, which is given by

$$F_{RCE}^{17\to18}(\theta, \Delta E) = 1 - e^{-k_R z_0}. \tag{4.5}$$

Adopting Eqs.(4.3) and (4.4), $F_{RCE}^{17\to18}(\theta, \Delta E)$ can be written as

$$F_{RCE}^{17\to18}(\theta, \Delta E) = 1 - f^{17}(\theta, \Delta E, z_0) \big/ f^{17}(\theta_{off}, \Delta E, z_0). \tag{4.6}$$

The contour map of the fraction, $F_{RCE}^{17\to18}(\theta, \Delta E)$, is shown in Fig.4.9. The fraction, $F_{RCE}^{17\to18}(\theta, \Delta E)$, becomes larger as the increase of the oscillation amplitude. This is due to the large RCE probability near the channel wall. The fact that oscillating ions spend longer time near the turning point of the trajectory than near the channel center tends to enhance $F_{RCE}^{17\to18}(\theta, \Delta E)$ for the larger amplitude. Fig.4.10 shows calculated energy levels of n = 2 states (Fig.2.15) described in the linear scale of the energy deposition, where the oscillation amplitude corresponding to the energy deposition is regarded as the distance form the channel center. The map of $F_{RCE}^{17\to18}(\theta, \Delta E)$ reflects the energy level of n = 2 states, and the wide splitting between Level 1 and 2 was clearly observed. The energy resolution of the SSD was ~80 keV. However, the experimental result was blurred by the energy straggling, which amounts to ~1 MeV. Moreover, there is a possibility of RCE not only at the turning point but also at other positions along the trajectory, and this fact also obscured the experimental results. As a result, no dip between Level 3 and 4 was observed.

Fig.4.7b is the (k,l) = (1,1) resonance profile for a crystal with a thickness of 21 μm. In this case, the fraction of ionized Ar^{18+} after transmission through the crystal was reduced to ~60 percent for off-resonance, while the fraction for thicker 94.7 μm crystal was ~80 percent. Under the RCE condition, the fraction increased to ~80 percent. The profile shows two peaks and the doublet structure of the left peak, which are the same features as those for 94.7 μm crystal (Fig.4.7a). However, the doublet structure was more clearly observed compared with the thicker case. This result is explained in the following way. From the electron impact ionization cross section [79] and the calculated target electron and nuclear densities averaged along the ion trajectory, the mean-free-path for 2p-ionization, $\lambda_{i(2p)}$, for channeled ions with the large oscillation amplitude (= 0.72 Å) is estimated to be ~1.6 μm. Therefore, once they are excited, they are easily ionized. On the other hand, the value of $\lambda_{i(2p)}$ for the best channeled ions is estimated to be ~58 μm, and they mostly maintain the incident charge state after passing through the 21 μm crystal even if they are excited. We can understand from Fig.4.10 that the channeled ions with the large oscillation amplitude excited to Level 1 and 2 correspond to the left and right peaks of the doublet structure, and the best channeled ions excited to Level 1 and 2 correspond to the dip. Therefore, the clear doublet structure in Fig.4.7b was formed. However, in the case of the 94.7 μm crystal, which is thicker than $\lambda_{i(2p)}$ for the best channeled ions, excited ions are eventually ionized. As a result, the dip was filled up, and the doublet structure was not clearly observed.

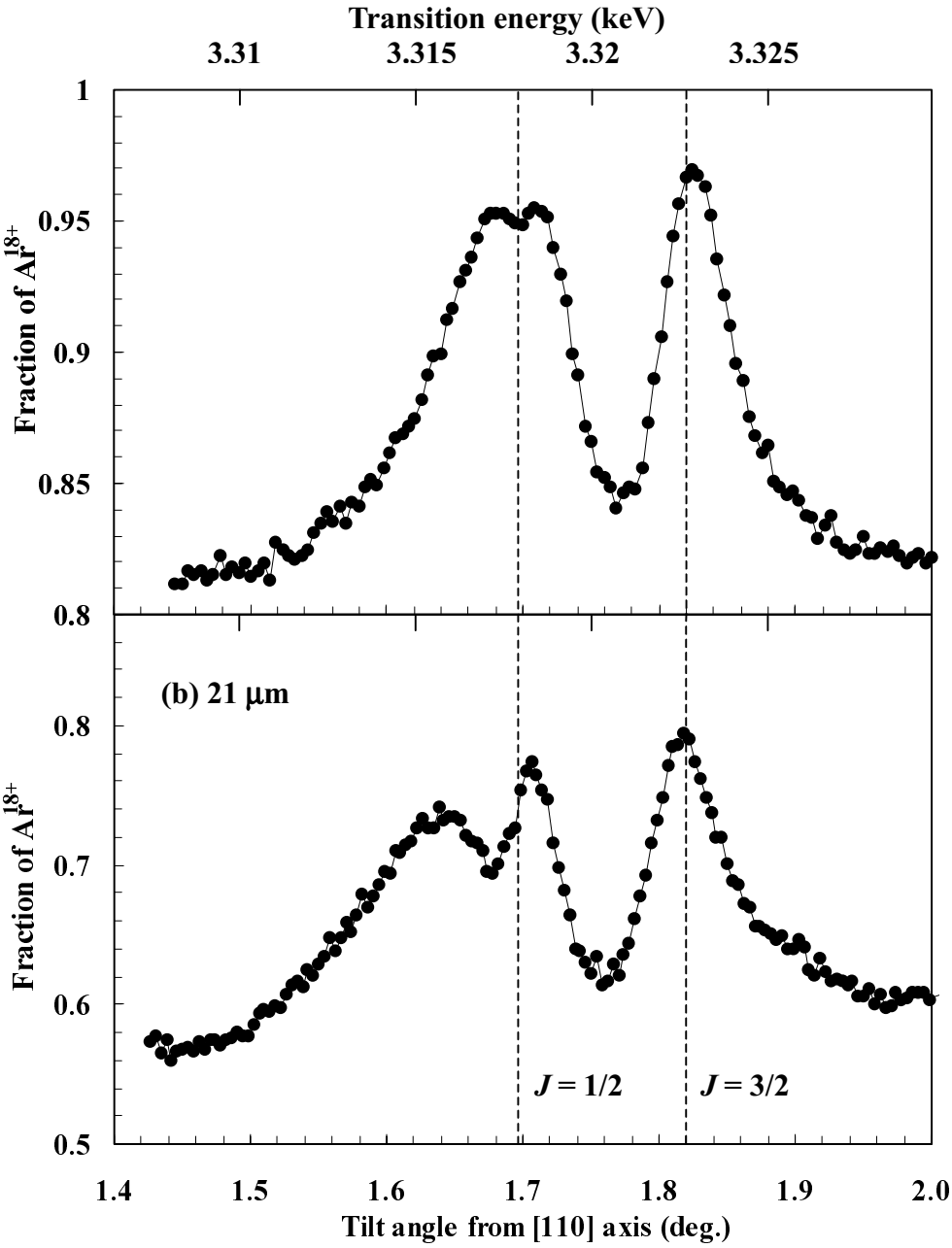

Fig.4.7 Detailed resonance profile of $(k,l) = (1,1)$ for (220) planar channeling in (a) 94.7 μm Si and (b) 21 μm Si. Lower scale is the tilt angle from [110] axis, and upper scale is the transition energy corresponding to the tilt angle. Dashed lines indicate the resonance conditions for 1s-2p transitions (J = 1/2 and J= 3/2) of hydrogen-like Ar in vacuum.

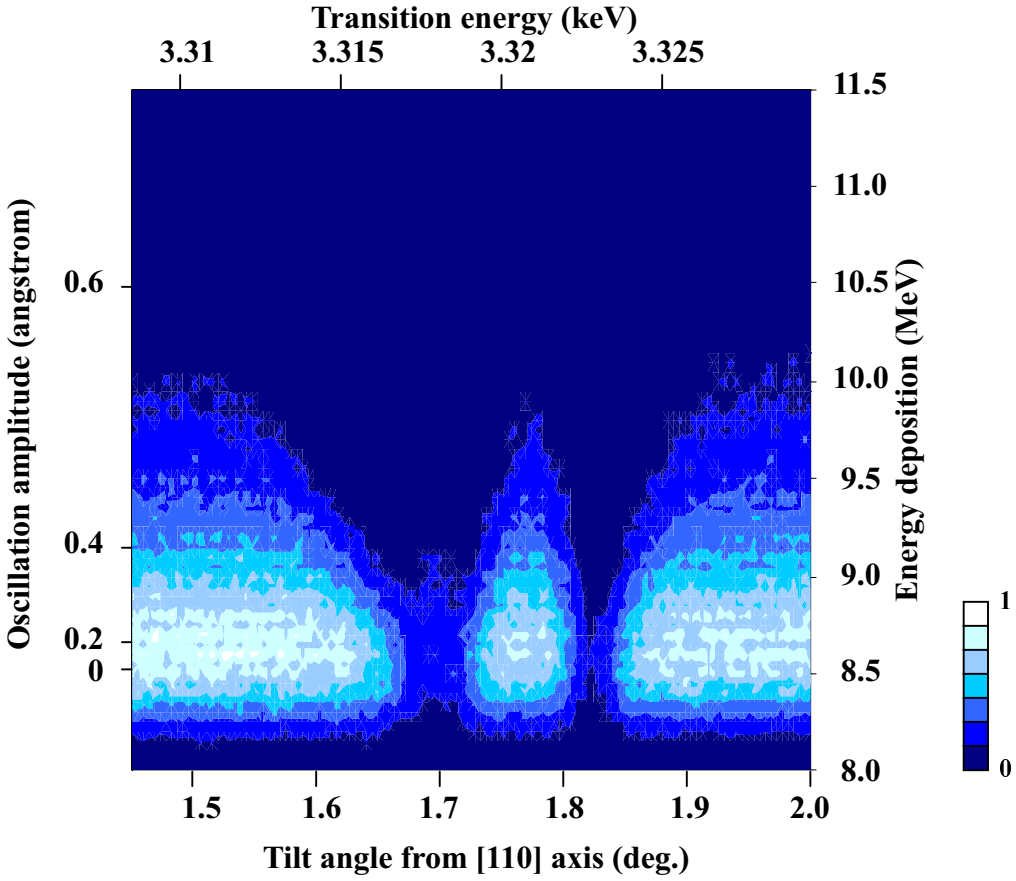

Fig.4.8 Contour map of fraction of survived Ar^{17+} ions with 94.7 μm Si as a function of the tilt angle and the energy deposition. Upper and left scales are the transition energy and the oscillation amplitude corresponding to the tilt angle and the energy deposition, respectively.

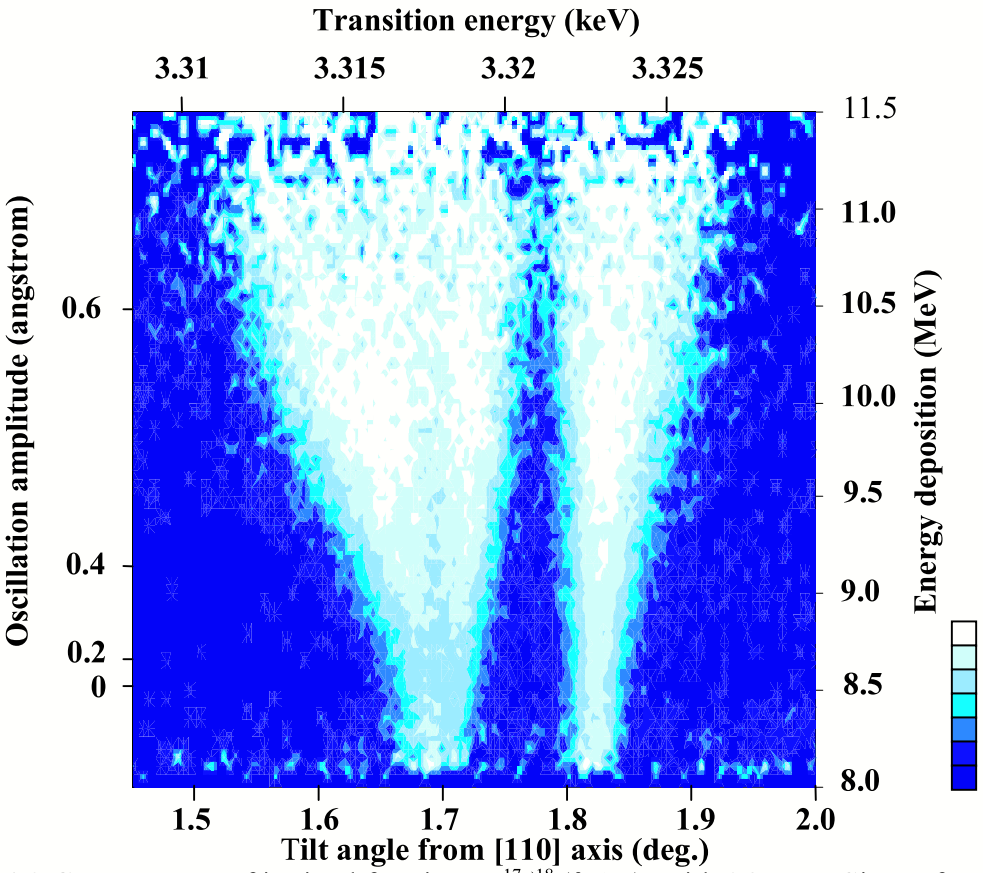

Fig.4.9 Contour map of ionized fraction, $F_{\mathrm{RCE}}^{17\rightarrow18}(\theta,\Delta E)$, with 94.7 μm Si as a function of the tilt angle (transition energy) and the energy deposition (oscillation amplitude).

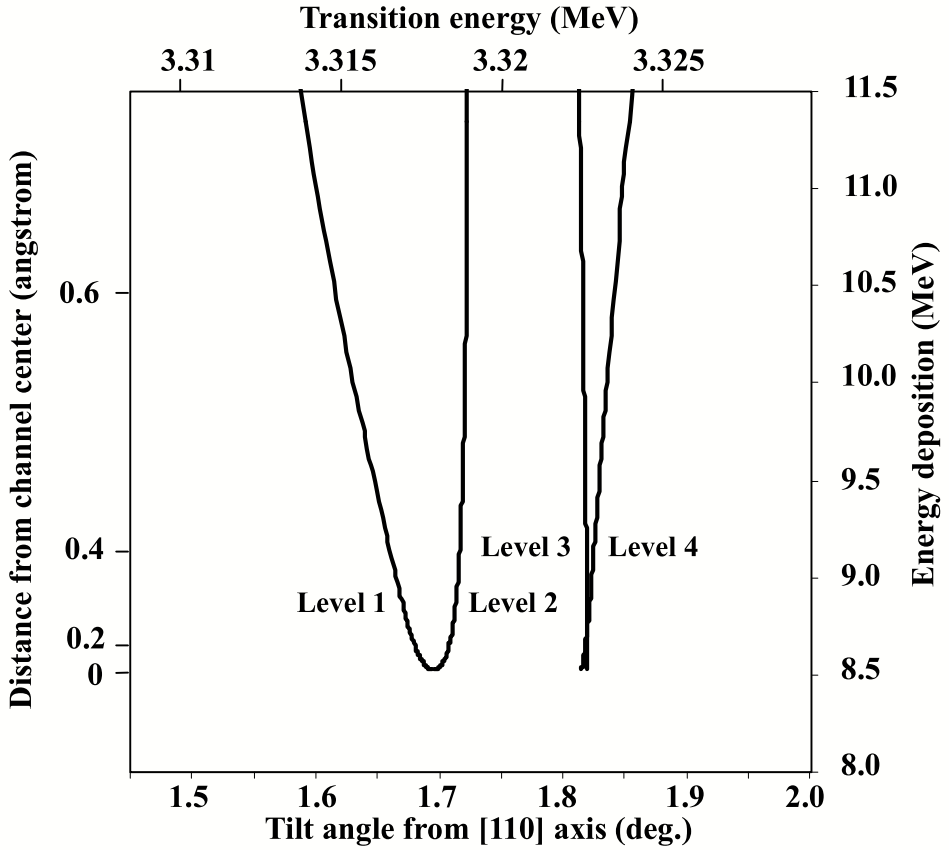

Fig.4.10 Calculated transition energy from 1s to $n = 2$ states of hydrogen-like Ar ion in vacuum as a function of the energy deposition corresponding to the oscillation amplitude.

4.3.3. Possible application to high precision atomic spectroscopy

Fig.4.11 is a sliced section of the contour map in Fig.4.9 in the range from 8.25 to 8.85 MeV, which corresponds to the channeled ions near the channel center. At the channel center, the crystal static field has little effect, and the splitting into two peaks dominantly originated from the spin-orbit interaction. Observed width (HWHM) of the $J = 3/2$ peak is 0.94 eV. The beam angular divergence ($\Delta\theta = 0.12$ mrad) affect to the peak width, which corresponds to the fluctuations of the transition energy of 0.26 eV. The fluctuation of the incident ion energy ($\Delta E_0/E_0 = 4\times10^{-4}$) also affect to the peak. In this experiment, the beam was collimated by the 1 mmϕ iron collimator, and the energy fluctuation may be suppressed, which is estimated to be $\Delta E_0/E_0 = 2\Delta p_0/p_0 \sim 2\Delta\theta = 2.4 \times10^{-4}$. This fluctuation corresponds to the peak width (fluctuation of the transition energy) of 0.47 eV. The total fluctuation of the transition energy amounts to $\sqrt{(0.26)^2 + (0.47)^2}$ = 0.54 eV. The energy loss of the best channeled ion in 94.7 μm Si crystal is ~9 MeV, which corresponds to ~1.1 eV-shift of the transition energy. However, a half of the ion path length per Rabi oscillation, $\lambda_R/2$, for the best channeled ion is 6.7 μm, *i.e.*, the RCE occurs mostly near the entrance surface of the crystal. Accordingly, an effective energy loss in 6.7 μm thickness affecting the resolution is reduced to ~0.078 eV, which is much smaller than the above fluctuation. Therefore, the resonance width is estimated to be $\sim\sqrt{(0.94)^2 - (0.54)^2}$ = 0.77 eV, which is 2.3 $\times10^{-4}$ of the transition energy. The relative resonance width, $\delta E/E_{\mathrm{trans}}$, is given by

$$\frac{\delta E}{E_{\mathrm{trans}}} \sim \frac{h/t}{E_{\mathrm{trans}}} = \frac{h\upsilon/nd}{E_{\mathrm{trans}}} \sim 1/n, \tag{4.7}$$

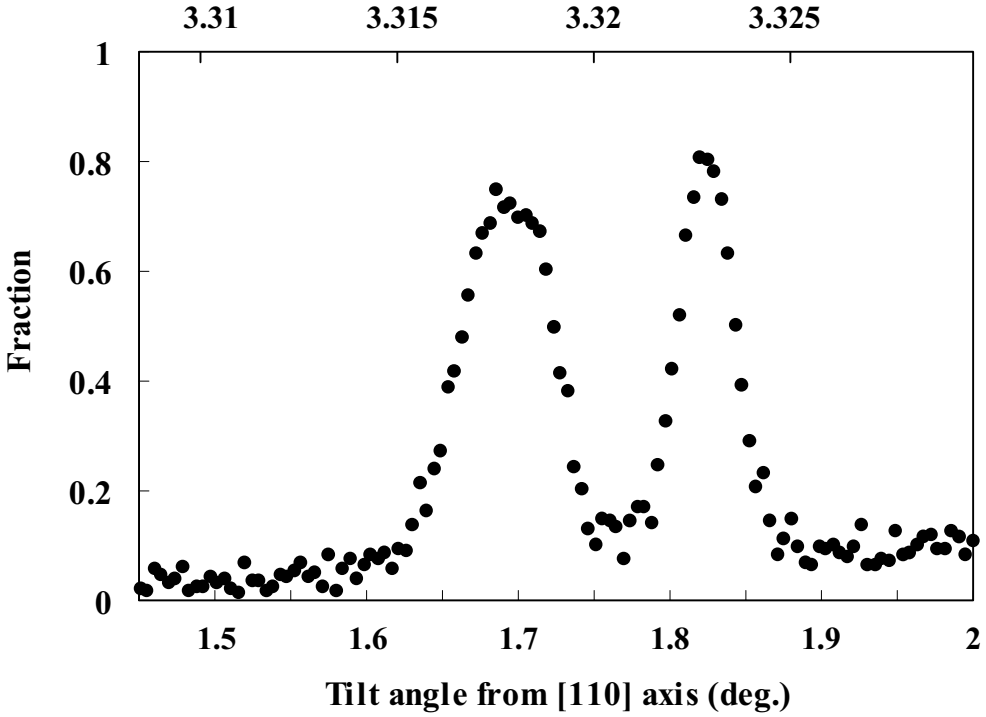

Fig.4.11 Ionized fraction through RCE process in the sliced section at energy range from 8.25 to 8.85 MeV.

where t is the perturbation time, d is the distance between atomic strings, and n is the number of the strings which the ion traverses in the time t. Accordingly, to achieve the relative width, $\delta E/E_{trans}$ ~2 $\times 10^{-4}$, n should be ~5 $\times 10^{3}$, *i.e.*, the coherent length of the RCE for the best channeled ions amounts to ~5 $\times 10^{3} d$, which is of the order of μm.

Fig.4.12 shows the $J = 3/2$ peak in Fig.4.11 fitted by the Gaussian shape. From the fitting, the peak position is determined within an accuracy of 0.04 eV. The determined peak position corresponds to the average of shifted energies (0.23 eV) for transition to Level 3 and 4, because the $J = 3/2$ state is split, shifting by 0.32 eV (Level 3) and 0.14 eV (Level4) to lower energy side the due to the wake field and the second order crystal field. If both transition energies from 1s to 2p and 1s to 3p are measured in the accuracy of 0.04 eV for ions with the same energy, the absolute ion energy can be determined within the precision of 9 $\times 10^{-5}$. The accuracy of 0.04 eV means that the Lamb shift of hydrogen-like Ar (1.14 eV) can be determined in the precision of 3.5 percent, which is of the same order of 1.5 percent in the latest measurement [87]. Therefore, this measurement has a possibility to become a new method of atomic spectroscopy with a high precision.

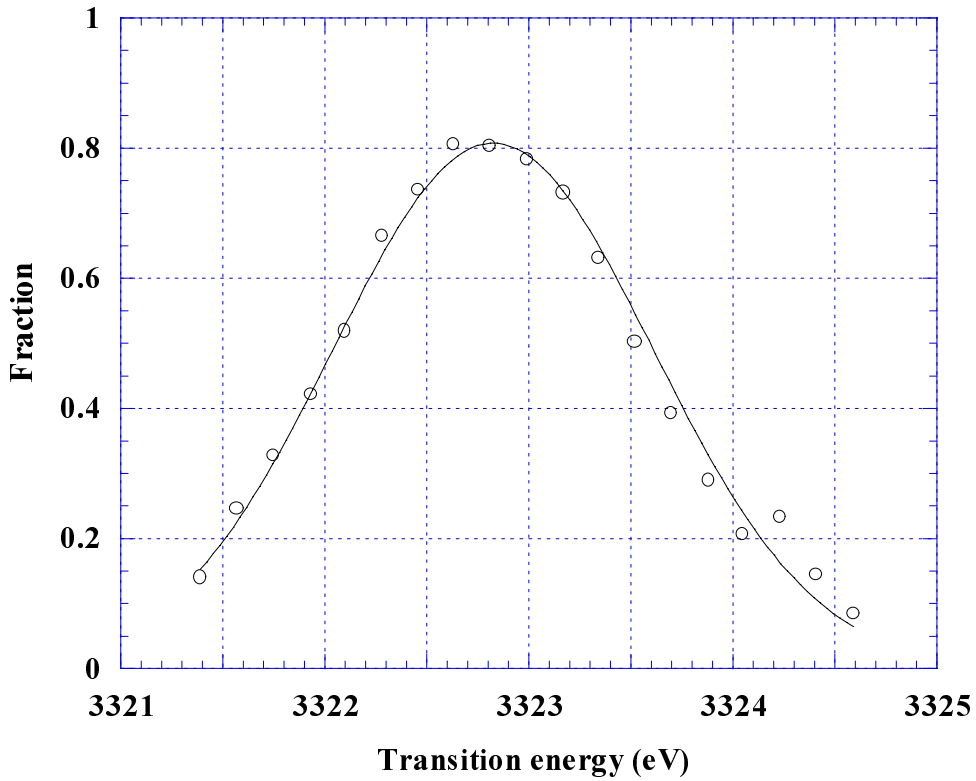

Fig.4.12 Resonance peak for $J = 3/2$ in Fig.4.11 with the fitting line by the Gaussian shape.

4.4. Measurement of convoy electron

Momentum spectra of convoy electrons were obtained by the measurement with the magnetic analyzer, and were transformed to energy spectra through the relations between the differential cross sections,

$$\frac{d\sigma}{dE} = \frac{dp}{dE}\frac{d\sigma}{dp} = \frac{\sqrt{(mc^2)^2 + (pc)^2}}{pc^2}\frac{d\sigma}{dp}. \tag{4.8}$$

Fig.4.13a is a typical energy spectrum of convoy electrons for 530 μg/cm^2 (2.35 μm) amorphous C target. Energy of the convoy electron is calculated to be 214 keV from the projectile velocity. Because the energy loss of the convoy electron in the target is quite small (~1 keV), the measured peak energy of the convoy electron agrees with the calculation, and the convoy electrons form a "cusp" shape in the energy spectrum.

Fig.4.13b shows spectra of convoy electrons produced with a 21 μm Si crystal for 1) random incident ions, 2) (220) planar channeled ions (off-resonance), and 3) (220) planar channeled ions under the RCE condition (θ = 1.82°). In the Si case, the energy loss of the convoy electron is significant. The peak position was 8 keV shifted to the lower energy side, and the spectrum became broader due to the multiple scattering. The energy loss of the incident ion is at most 0.025 percent even for random case, which can be neglected compared with that of the convoy electron. Calculated energy loss of electron with the energy of 214 keV is ~11 keV. Considering the ionization mean-free-path (3.3 μm), effective thickness is reduced to ~18 μm, and the energy loss of electron becomes to ~9.5 keV. Therefore, the experimental peak shift of 8 keV is reasonable. A peak shift of the spectrum for channeled ions (off-resonance) was 5 keV, which is smaller than that of the random case. The 5 keV-energy loss corresponds to the path length of ~10 μm for free electron, *i.e.*, incident Ar^{17+} ions were ionized after ~10 μm path. However, the ionization mean-free-path of channeled Ar^{17+} ions is estimated to ~30 μm from the experimental result of survived Ar^{17+} fraction under the channeling condition. The result indicates most of the Ar^{17+} ions keep their incident charge state after ~10 μm path. This inconsistency is possibly explained by the electron diffraction effect. The above discussion about the energy loss is for random incident electron. When the convoy electrons travel along the channel plane, the 5 keV-energy loss can be attributed to the abnormal absorption due to the electron diffraction (see appendix2), because the number of the quantum state, n_p, given by Eq.(A.19) is ~0.4 for 214 keV electron. Under the RCE condition, the shift of the spectrum increased to 7 keV, because the ionization mean-free-path of ~15 μm estimated from the experimental result is smaller than that for off-resonance. Similar to the off-resonance case, the 7 keV-energy loss corresponding to the ~13 μm path for random electron may contain the electron diffraction effect. The intensity of convoy electrons increased, and the spectrum became sharper (FWHM ~17 keV) compared with the off-resonance case (~22 keV). This result agrees with the theoretical prediction in Ref.[59] that the width of the cusp shape for convoy electrons from 2s or $2p_1$ state is narrower than that from the ground state, because the ionization from n = 2 states increases under the RCE condition.

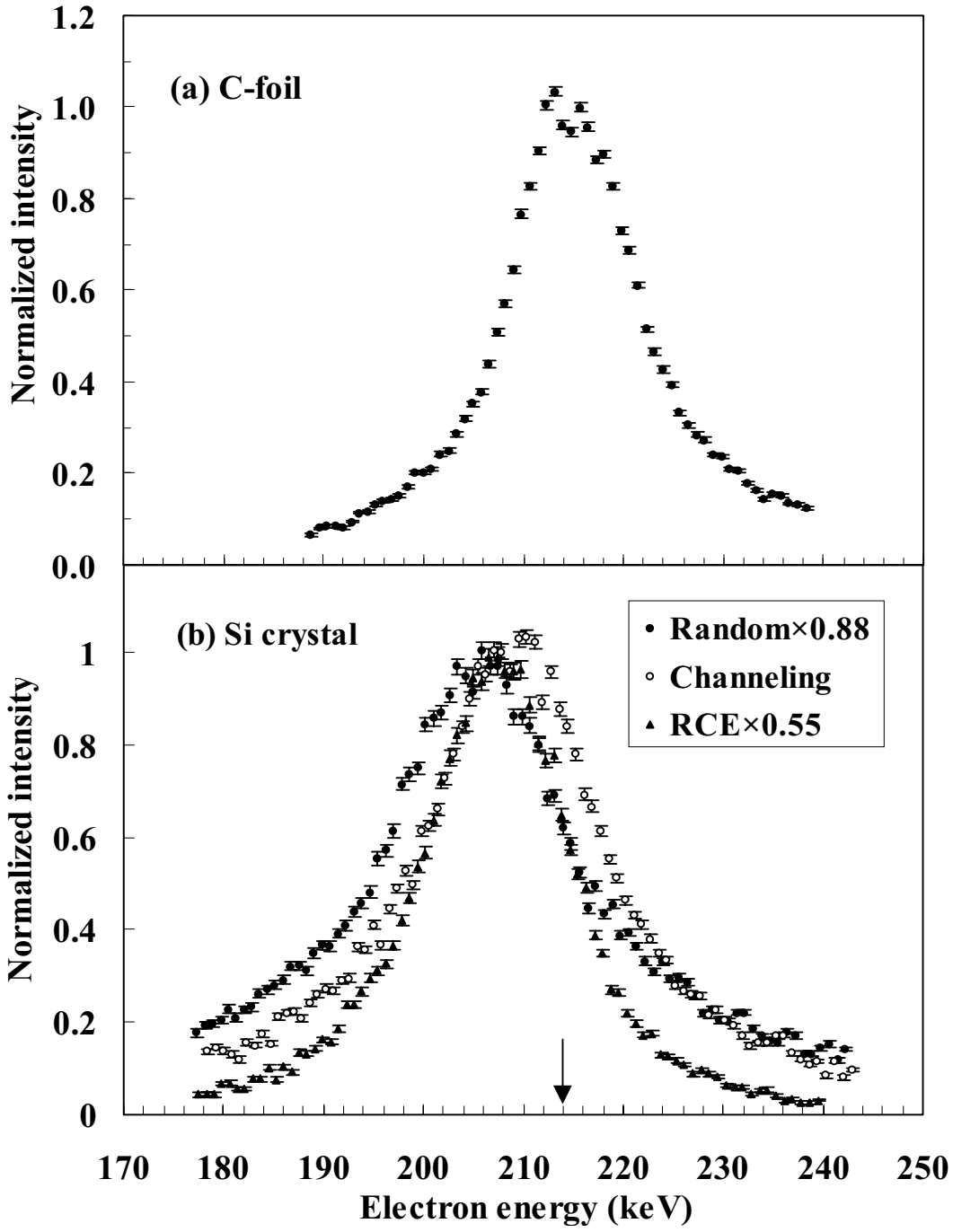

Fig.4.13 Energy spectra of convoy electrons with (a) C-foil (530 μg/cm^2) and (b) Si crystal (21 μm) for random incidence, channeling (off-resonance) and RCE condition (θ = 1.82°). The arrow indicates the energy of electron with the same velocity as the projectile.

The intensity of convoy electrons at the peak position for the RCE condition (θ = 1.82 °) was plotted as a function of the tilt angle in Fig.4.14. The profile has two-peak structure similar to the charge state profile. The intensity of convoy electrons under the RCE condition is two times larger than that for off-resonance. Such a clear resonance profile for convoy electrons has never been observed in the previous experiments with lower energy ions [18]. There is a difference at the doublet structure of the J = 1/2 peak, θ ~1.64° and ~1.71°, corresponding to Level 1 and 2. The right peak of the doublet (θ ~1.71°) in the charge state profile vanished in the convoy electron profile. The shape of the spectrum for convoy electrons depends on the initial state of the loss (convoy) electron. The characteristics of resonance profile for convoy electrons can be attributed to the composition of the initial states, *i.e.*, n = 2 states, under the channeling condition. According to the theoretical prediction, the convoy electrons from $2p_0$ state ($2p_z$ state in the present paper) form an "anti-cusp" shape in the energy spectrum. The $2p_z$ component in Level 2 is much larger than that in Level 1 especially for the large distance from the channel center (see Fig.2.16). The energy spectrum of convoy electrons from Level 2 is considered to be broader, and has a lower peak height compared with that of convoy electrons from Level 1. As a result, the height of the right peak (θ ~1.71°) becomes lower compared with the left peak (θ ~1.64°).

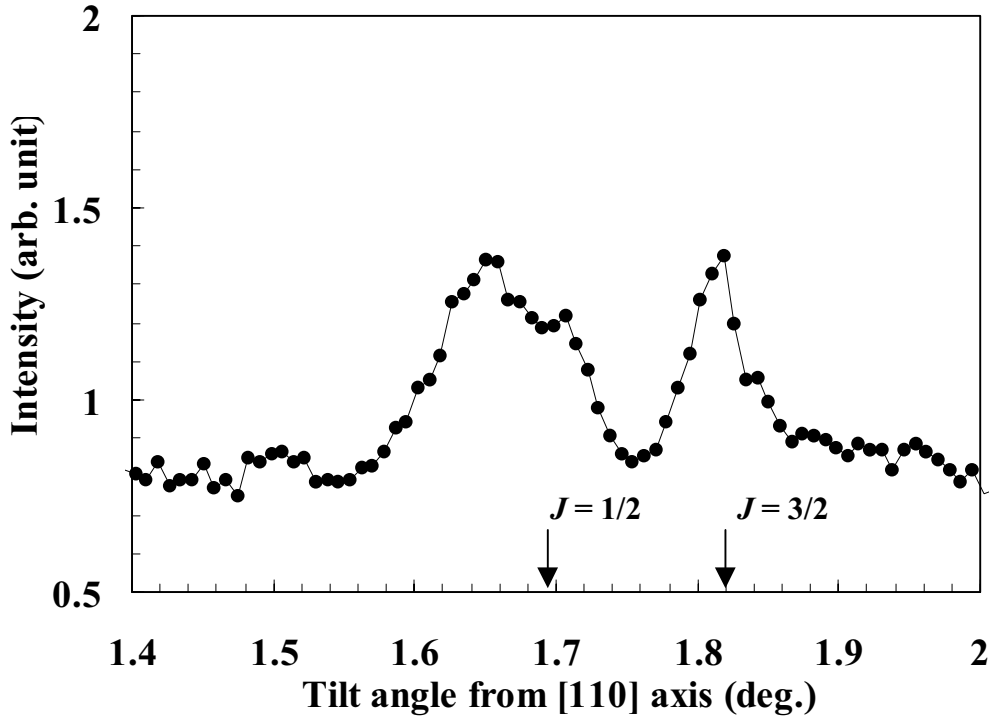

Fig.4.14 Intensity of convoy electron for 21 μm Si crystal as a function of the tilt angle from [110] axis. Arrows indicate n = 2 states (J = 1/2 and 3/2) in vacuum.

4.5. Measurement of de-excitation X-rays

4.5.1. X-ray energy spectra

X-ray energy spectra for random incidence, channeling (off-resonance), and RCE condition ($\theta = 1.82°$) are shown in Fig.4.15. The thickness of the adopted Si crystal was 21 μm. Si K X-rays are seen as a peak around 1.7 keV. De-excitation X-rays from Ar ions are Doppler shifted from 3.3 keV to 5.0 keV. The detection angle of 41° in the laboratory frame corresponds to 84.4° in the projectile frame, *i.e.*, the observed X-rays were emitted to the direction almost perpendicular to the beam direction. Although 1s-2p excitation probability for channeling case is smaller, the intensity of de-excitation X-rays becomes larger compared with the random incidence, because the 2p-ionization probability of channeled ions is much smaller, and consequently, excited ions under the channeling condition decay more *via* the X-ray emission compared with the random incidence. Under the RCE condition, the coherent excitation process becomes dominant, and the intensity of the de-excitation X-rays is further enhanced.

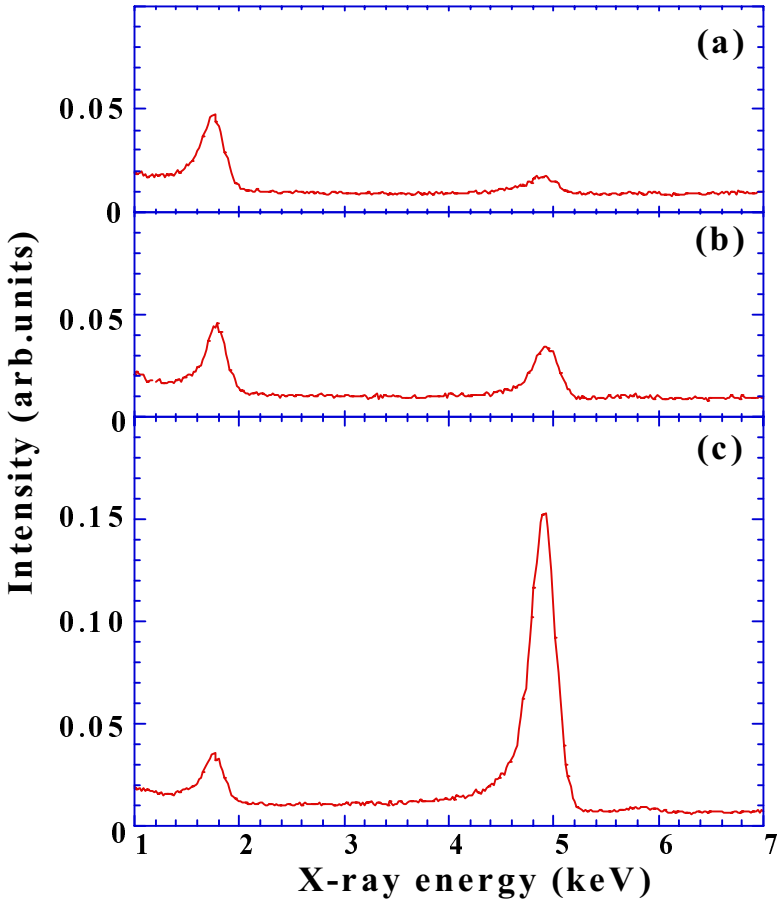

Fig.4.15 X-ray energy spectra for (a) random incidence, (b) channeling (off-resonance) and (c) RCE condition ($\theta = 1.82°$).

4.5.2. RCE profile for de-excitation X-rays

Intensities of de-excitation X-rays measured by the Si(Li)-detectors (H) and (V) are plotted as functions of the tilt angle from [110] axis in Fig.4.16. Closed and open circles are the data for the detectors (H) and (V), respectively. The right scale of ordinate in Fig.4.16 is the number of X-rays per incident ion estimated with an assumption of isotropic X-ray emission. The X-ray resonance profile shows (1) two-peak structure (J = 1/2 and J = 3/2) similar to the resonance profiles for the charge state and convoy electrons, (2) much lower height of the J = 1/2 peak compared with the J = 3/2 peak. (3) disappearance of the doublet structure in the J = 1/2 peak, which was clearly seen in the charge state profile (Fig.4.7b), and (4) no anisotropy of the X-ray emission.

The feature (1) is due to the level splitting by spin-orbit interaction as discussed in Sec.4.3.2. The feature (2) can be explained as a dominance of 2s component in Level 1 and 2 as shown in Fig.2.16. Ions excited to 2s state, which has a long lifetime, hardly decay with the X-ray emission because of the much larger probability of 2s-ionization. This fact results in the suppression of the J =1/2 peak. On the other hand, 2s state in Level 3 and 4 is a minor component. Accordingly, the J = 1/2 peak corresponding to Level 1 and 2 is smaller than the J = 3/2 peak corresponding to Level 3 and 4.

To discuss the feature (3), several mean-free-paths are listed in Table3, and a rough sketch of probabilities as a function of the distance from channel center is shown in Fig.4.17. A following discussion is about ionization or de-excitation only from 2p state. Actually, n = 2 states contain 2s component, but, the difference of the ionization probability between 2s and 2p states is not so significant, and the radiative lifetime becomes at most 2 times longer, when the fraction of 2s component is 50 percent. Therefore, the discussion with mean-free-paths for 2p-ionization, $\lambda_{i(2p)}$, and for de-excitation, $\lambda_{x2p)}$, is reasonable. Values of $\lambda_{i(2p)}$ for the best channeled ion and the channeled ions with the oscillation amplitude of 0.72 Å are ~58 and ~1.6 μm, respectively. The value of $\lambda_{x(2p)}$ is ~4.6 μm [83]. It is noted that $\lambda_{x2p)}$ is independent of the distance from the channel center. For channeled ions with the large oscillation amplitude, $\lambda_{i(2p)}$ is shorter than $\lambda_{x(2p)}$, *i.e.*, these ions have a small probability of radiative decay, although the RCE probability increases as the distance from the channel center increases. On the other hand, $\lambda_{i(2p)}$ for channeled ions near the channel center is much longer than $\lambda_{x(2p)}$, and excited ions mostly decay with the X-ray emission. The best channeled ions excited to Level 1 or 2 correspond to the dip position of the charge state profile (tilt angle θ ~1.68 °). Because of the dominance of the X-ray emission from the ions near the channel center, the dip was not formed in the X-ray profile.

The feature (4) can be qualitatively explained as follows. According to the above discussion, the channeled ions near the channel center mainly contribute to the X-ray profile. As shown in Fig.2.16, the ratio of $2p_x$, $2p_y$ and $2p_z$ components in Level 1 and 2 is almost 1 : 1 : 1 for ions near the channel center. As for Level 3 and 4, the ratio of $2p_x$, $2p_y$ and $2p_z$ components is not 1 : 1 : 1 for each level. However, the energy difference between Level 3 and 4 is so small near the channel center (see Fig.2.15) that both Level 3 and 4 are partially on resonance and the X-rays form Level 3 and 4 are mixed in the right peak. The ratio of $2p_x$(Level 3)+$2p_x$(Level 4), $2p_y$(Level 3)+$2p_y$(Level 4) and $2p_z$(Level 3)+$2p_z$(Level 4) components becomes ~ 1 :1 : 1. Moreover, the probabilities of RCE to each level can be regarded to be almost equal with each other. As a result, the anisotropy of de-excitation X-rays from Level 1, Level 2 and J = 3/2 state (Level 3 +

Level 4) was also not observed.

Assuming that the distribution of the X-ray emission is isotropic in the projectile frame, the number of radiative decays per incident ion is estimated to be ~0.2 at the right peak (θ = 1.82 °) from consideration of the geometrical efficiency of the detector. The Ar^{18+} fraction due to RCE increased by 20 percent (from 60 to 80 percent) as shown in Fig.4.7b. It means that the event numbers of X-ray emission and ionization are comparable in this case.

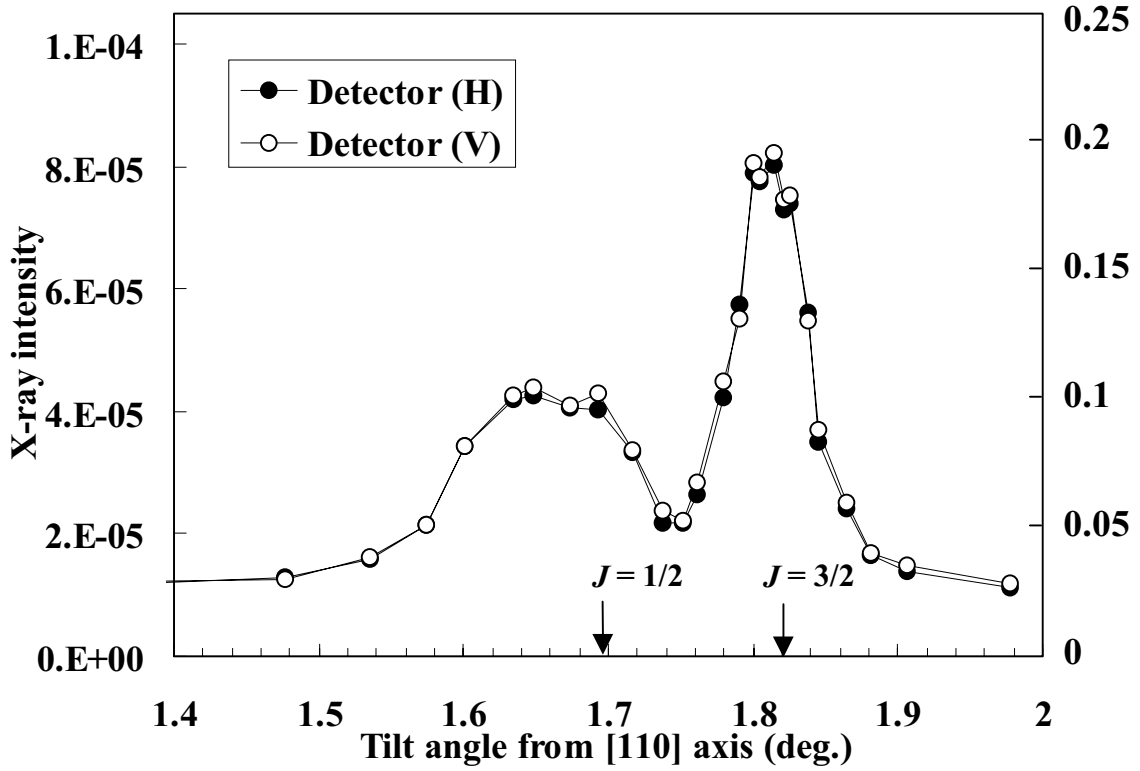

Fig.4.16 Intensity of de-excitation X-rays measured by the two Si(Li)-detector as a function of the tilt angle from [110] axis. Arrows indicate n = 2 states (J = 1/2 and 3/2) in vacuum. The right scale indicates the number of the X-rays per incident ion.

Table3 Mean-free-paths for 2p-ionization, $\lambda_{i(2p)}$, radiative decay from 2p, $\lambda_{x(2p)}$, intra-shell transition from 2s-2p, $\lambda_{e(2s-2p)}$, and a half of the path length per Rabi oscillation, $\lambda_R/2$, for best channeled ions and the ions with large oscillation amplitude (=0.72 Å).

	Best channeled	Amplitude = 0.72 Å
$\lambda_{i(2p)}$	58 μm	1.6 μm
$\lambda_{x(2p)}$	4.6 μm	4.6 μm
$\lambda_{e(2s-2p)}$	62 μm	1.7 μm
$\lambda_R/2$	6.7 μm	0.9 μm

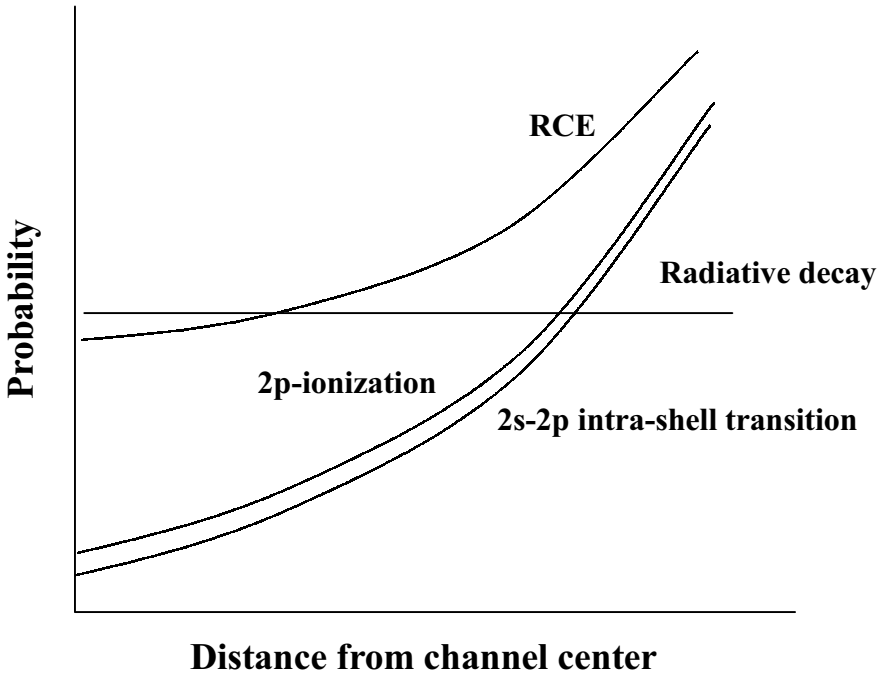

Fig.4.17 Rough sketch of probabilities of 2p-ionization, 2s-2p intra-shell transition, and radiative decay and RCE as a function of the distance from the channel center.

4.6. Monte Carlo simulation of RCE

To understand the RCE phenomena quantitatively, a Monte Carlo simulation was performed. The time evolution of $n = 2$ state through coherent processes is described as in Eq.(2.114). Incoherent processes should be included in the right hand side of Eq.(2.114) as imaginary parts [13-15]. However, the situation is so complex that it is difficult to solve Eq.(2.114) rigorously. The distance from the channel center, x, changes together with the channeling oscillation, and the transition amplitude, $M_{21}(x)$, is actually a function of time t. Moreover, the energy difference between the ground state and an $n = 2$ state, E_{trans}, also depends on x (see Fig.2.15), *i.e.*, it is also a function of t. Further, the path lengths of the ion per channeling oscillation and per Rabi oscillation are comparable. Accordingly, the Rabi frequency varies at every moment, and the transition probability can not be described as a simple sinusoidal curve as in Eq.(2.121). Considering only the straight line trajectory, *i.e.*, fixing the impact parameter, is one of the method to simplify the calculation [15]. In the present simulation, the ion trajectories were exactly calculated, and the impact parameter dependence of $M_{21}(\mathrm{x})$ and E_{trans} was taken into account. The probability of coherent excitation (de-excitation) was given at every step, Δz, *i.e.*, it was treated as "incoherent-like", where Δz is a step of ion position along the beam direction.

A flow chart of the simulation is shown in Fig.4.18. If x is constant, the population probability in one of the $n = 2$ states for channeled ions at position, x, is given by

$$\left|a_2(t)\right|^2 = \frac{4\left|M_{21}(x)\right|^2}{\hbar^2 \Omega^2} \sin^2 \frac{\Omega}{2} t \,. \tag{4.9}$$

Modifying Eq.(4.9), the transition probability from 1s to an $n = 2$ state per step, Δz, was put as

$$w_{21}(x) = \frac{4M_{21}^2(x)}{\hbar^2 \Omega^2(x)} f_{\mathrm{t}}(\Delta z) \,, \tag{4.10}$$

where $f_{\mathrm{t}}(\Delta \mathrm{z})$ is a fitting parameter depending on Δz. Eq.(4.10) means that the sinusoidal increase (or decrease) of the population in the $n = 2$ state, *i.e.*, Rabi oscillation effect, was averaged, and the effect was represented by the parameter, $f_{\mathrm{t}}(\Delta z)$. In the simulation, a step of the ion position along the beam direction, Δz, was selected to be $10d_{\mathrm{p}}$ ($=1.92\times10^{-3}$ μm) which is $\sim10^{-3}$ of the wavelength of the channeling oscillation, but is long enough for the ion to feel the crystal periodicity. The parameter, $f_{\mathrm{t}}(\Delta z)$, is expected to be ~ 10^{-3}, because $w_{21}(x)$ should be of the order of unity, when the ion passes several μm ($\sim\lambda_{\mathrm{R}}/2$). The transition probability from an $n = 2$ to 1s state is also given by Eq.(4.10).

As for the incoherent processes, the calculated results of electron impact ionization and excitation cross sections with the plane wave Born approximation [79] were adopted. In the simulation, $n \geq 3$ states were not considered, and excited ions to $n \geq 3$ states were regarded as ionized. The 1s-, 2s- and 2p-ionization cross sections, $\sigma_{\mathrm{i(1s)}}$, $\sigma_{\mathrm{i(2s)}}$ and $\sigma_{\mathrm{i(2p)}}$ were replaced with

$$\sigma'_{\mathrm{i(1s)}} = \sigma_{\mathrm{i(1s)}} + \sigma_{\mathrm{ex(1s\to n=3)}} + \sigma_{\mathrm{ex(1s\to n=4)}} + \cdots, \tag{4.11}$$

$$\sigma'_{\mathrm{i(2s)}} = \sigma_{\mathrm{i(2s)}} + \sigma_{\mathrm{ex(2s\to n=3)}} + \sigma_{\mathrm{ex(2s\to n=4)}} + \cdots, \tag{4.12}$$

$$\sigma'_{\mathrm{i(2p)}} = \sigma_{\mathrm{i(2p)}} + \sigma_{\mathrm{ex(2p\to n=3)}} + \sigma_{\mathrm{ex(2p\to n=4)}} + \cdots, \tag{4.13}$$

where σ_{ex} is an excitation cross section. Ionization cross sections from an $n = 2$ state

were calculated with Eq.(4.12) and (4.13) considering the ratio of 2s and 2p components. Strictly speaking, the ionization probabilities from $2p_x$, $2p_y$ and $2p_z$ states are different from each other, when the spatial distribution of the bound electron and the density of the target electron flux are considered. However, the difference is not considered to be so significant, because the orbital radius of electron in 2p state (~0.14 Å) is much smaller than the inter-planar distance (1.92 Å). The cross sections for excitation from 1s to an n = 2 state and for intra-shell transition between n = 2 state were similarly calculated considering the compositions of 2s and 2p components in each n = 2 state. Here, the cross section from 2s to 2p and that from 2p to 2s are regarded to be equal. Following Eq.(2.46) for random incidence, the cross section per atom was written as

$$\sigma_t = \left[\frac{n_e(x) + Z_2^2 N(x)}{N} \right] \sigma_e , \tag{4.14}$$

where $n_e(x)$ and $N(x)$ are the local electron and nuclear densities, respectively.

The radiative life time of an n = 2 state in the projectile frame, τ, is given by

$$\frac{1}{\tau} = \frac{|c_{2s}|^2}{\tau_{2s}} + \frac{|c_{2px}|^2 + |c_{2py}|^2 + |c_{2pz}|^2}{\tau_{2p}} , \tag{4.15}$$

where τ_{2s} and τ_{2p} are the life times of 2s and 2p states, which are 3.5×10^{-9} and 1.53×10^{-14} sec, respectively [84,85]. A probability of radiative decay within a time step, $\Delta t'$ (= $\Delta z/v$), in the laboratory frame is written as

$$P_x = \Delta t'/\gamma\tau. \tag{4.16}$$

An angular distribution of de-excitation X-rays from an n = 2 state was represented as an average of those from 2s, $2p_x$, $2p_y$ and $2p_z$ states with a consideration of the ratio of each component, $|c_{2s}|^2$, $|c_{2px}|^2$, $|c_{2py}|^2$ and $|c_{2pz}|^2$. The angular distribution from 2p state is in accordance with Eq.(4.1) in the projectile frame, and should be transformed to the laboratory frame through the Lorentz transformation,

$$\tan\theta' = \frac{\sqrt{1-\beta^2}\sin\theta}{\cos\theta + \beta} , \tag{4.17}$$

where θ and θ' are angles in the projectile and the laboratory frames, respectively. The X-ray absorption within the Si crystal was considered, which depends on the depth of the position where the ion emitted the X-ray [88].

The angular distribution of the incident beam was represented by a Gaussian distribution whose standard deviation is equal to the experimental one. The fluctuation of the incident beam energy ($\Delta E_0/E_0$ = 2.4 $\times10^{-4}$) was also included. The ion which approached the channel wall closer than the one-dimensional amplitude of the lattice vibration, u_1, was regarded as a random incident ion, and only the incoherent processes were assumed to take place for random ions.

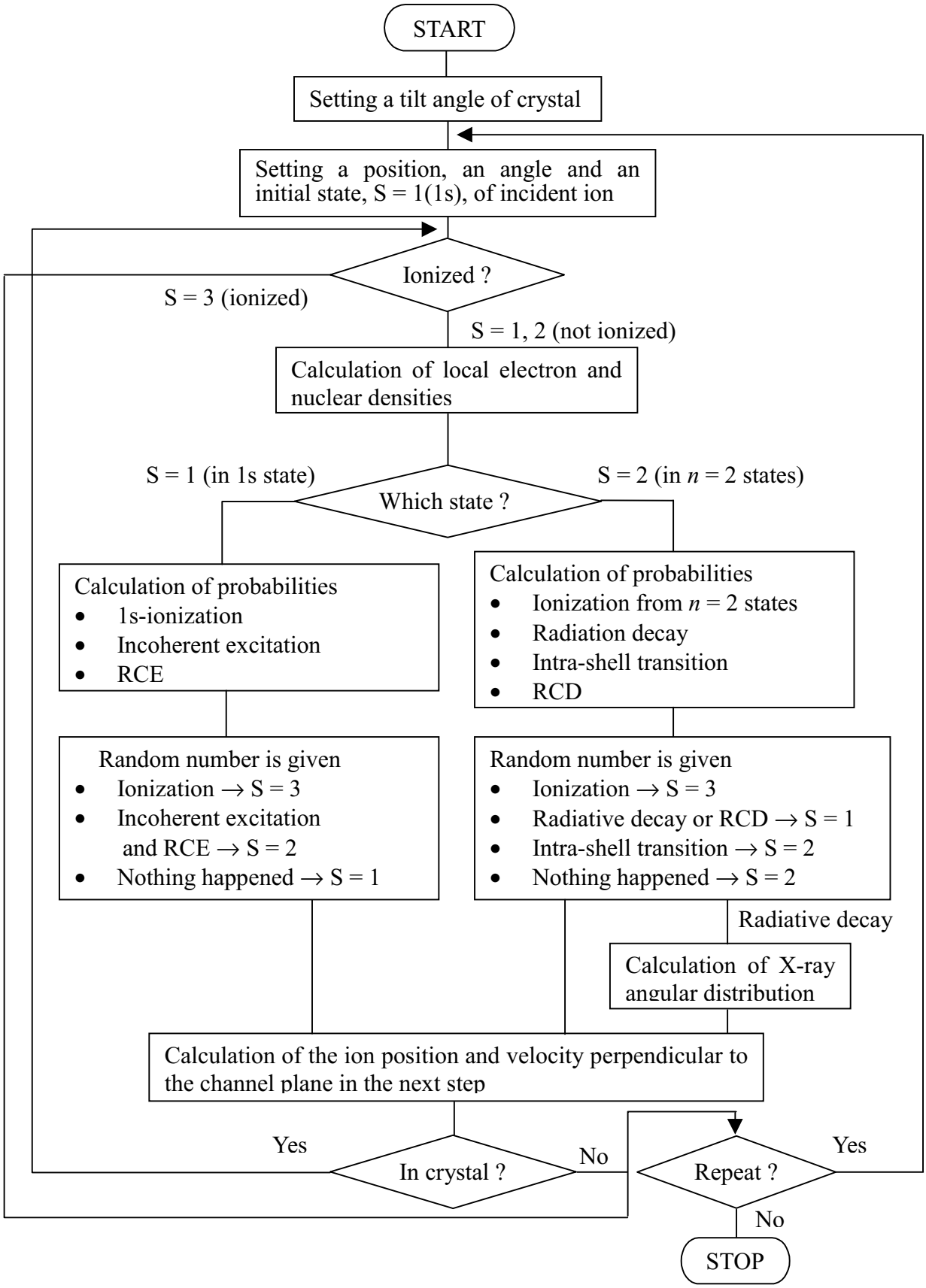

Fig.4.18 Flow chart of the simulation for atomic processes of channeled ions

4.7. Results and discussion

The simulated results of the fraction of ionized Ar^{18+} ions transmitted through 21 μm Si crystal for f_t = 0.005, 0.001 and 0.0001 are shown in Fig.4.19. The simulated result for f_t = 0.001 is the closest to the experimental result which is given by the solid line. Although the details of the structure such as the doublet of the left peak (J = 1/2) was not reproduced, the general feature agrees with the experimental result. Fig.4.19 tells ;

(1) For f_t = 0.005 : the fraction of Ar^{18+} for off-resonance becomes larger, but, that under resonance conditions does not increase so much compared with the case for f_t = 0.001. As a result, the two-peak (J = 1/2 and J = 3/2) structure was obscured.

(2) For f_t = 0.0001 : the fraction of Ar^{18+} does not reach ~80 percent even under resonance conditions.

These results can be understood as follows. The time evolutions of the population in n = 2 states, $P_2(t)$, for several values of f_t, and for on- and off-resonance are shown in Fig.4.20. For f_t = 0.001, $P_2(t)$ for on-resonance is close to 0.5, and that for off-resonance is much smaller than 0.5, when the ions pass through the crystal ($t' = t_0 \equiv z_0/v$), where z_0 is the target thickness and v is the ion velocity. For f_t = 0.005, however, the value of P_2 (t_0) is close to 0.5 even for off-resonance. For on-resonance, the reiteration of RCE and RCD becomes quite frequent, but the value of $P_2(t_0)$ does not exceed 0.5, and further enhancement of Ar^{18+} fraction did not occur. This situation led to the result (1). On the other hand, for f_t = 0.0001, the value of P_2 (t_0) is much smaller than 0.5 even for on-resonance, and this causes the result (2).

The simulated results of resonance curve for X-rays are shown in Fig.4.21. The two-peak structure and the suppression of the left peak reproduce the experimental result quite well. The isotropic distribution observed in the right peak is also reproduced in this simulation, and that in the left peak remains slightly. The X-ray intensity is 1.5 times larger than the experimental result, but the agreement is considered to be satisfactory. The X-ray intensity in the lower energy part of the left peak (θ = 1.6° – 1.65°, corresponding to Level 1) is slightly smaller than the experiment. As for the simulated result of charge state distribution (Fig.4.19), the left peak of the doublet structure (corresponding to Level 1) did not appear. In other words, both ionization and de-excitation from Level 1 occur with a larger probability than the simulation.

Fig.4.22 shows event numbers per unit length of RCE and RCD as functions of the distance from the channel center, x, for channeled ions with the oscillation amplitude of 0.72 Å, which is injected into the crystal in parallel to the channel plane, under the resonance condition of θ = 1.82°. The result shows that most part of the RCE process occurs near the turning point of the ion trajectory, which was also revealed by the measurement of the impact-parameter dependent RCE in Sec.4.3. The event numbers per unit length of RCE and RCD processes as functions of the ion position along the beam direction, z, have structures as shown in Fig.4.23a. It is related to the oscillatory trajectory of the channeled ions. When the ion approaches the turning point of the trajectory, the RCE probability increases because of the increase of the crystal field. The probability takes the maximum and minimum values at the turning point and the channel center, respectively. Sharp dips in Fig.4.23a correspond to the position, z, that the ions are at the channel center. The event numbers of 1s-ionization and ionization from n = 2 states are shown in Fig.4.23b. They have a clear oscillation structure, and the

frequency corresponds to that of the oscillation of the ion trajectory, because the ionization probability has the maximum value every time that the ions approach the turning point where the electron and nuclear densities are the largest. As the result of the competition with 1s-ionizations, the event number of RCE decreases near the turning point, because the slope of the increase of 1s-ionization is steeper than that of RCE, and ions in the ground state are ionized before the RCE occurs. Therefore, small dips in Fig.4.23a correspond to the turning points.

Fig.4.24 shows the event numbers per unit length of RCE, RCD, 1s-ionization, ionization from $n = 2$ states, intra-shell transition between $n = 2$ states and radiative decay as functions of x for channeled ions with all trajectories. The event number of RCE and RCD have a peak at x ~0.4 Å, although RCE and RCD probabilities for channeled ions with larger oscillation amplitude are larger. This is due to the competition with ionizations from 1s and $n = 2$ states, which have the large probability (event number) at the large distance from the channel center as shown in Fig.4.24b. Most of the intra-shell transition occurs near the channel wall similar to the ionization from 1s and $n = 2$ states. On the other hand, de-excitation X-rays are mostly emitted from the ions at the region of $x < 0.5$ Å where the ionization and intra-shell transition do not occur too much. It means that the intra-shell transition, which tends to stir the composition of 2s, $2p_x$, $2p_y$ and $2p_z$ in the initial excited state, scarcely affects the X-ray resonance profile. In fact, the observed X-ray profile (Fig.4.16) keeps the information of the initial excited state, *i.e.*, the left peak becomes smaller than the right peak. This simulated result supports the discussion about the experimental X-ray profile in Sec.4.5.

Event numbers per unit length of RCE, RCD, 1s-ionization, ionization from $n = 2$ states, intra-shell transition and radiative decay as functions of z for channeled ions with all trajectories are shown in Fig.4.25. The event numbers of RCE and RCD reflect the evolution of the population in the ground and $n = 2$ states, respectively. It is noted that 70 percent of the RCE processes occur in the region of 10 μm from the entrance surface. The oscillation structure of the event number of RCE due to the ion trajectory, which is seen in the case of a single trajectory (Fig.4.23a), disappears as a result of the averaging for all trajectories. On the contrary, the oscillation structure of ionization remains in the shallow region because of the strong dependence on the ion position. The 1s-ionization and $n = 2$ ionization (or intra-shell transition) also reflect the evolution of the population in the ground and $n = 2$ states, respectively, as well as the effect of the ion trajectory, and they mostly occur near the entrance surface similar to the RCE. However, the radiative decay does not have a significant z-dependence. It means that the charge state and the convoy electrons present the information on the RCE occurred closer to the entrance surface, and the X-rays contain that on the RCE occurred in the whole region of the crystal.

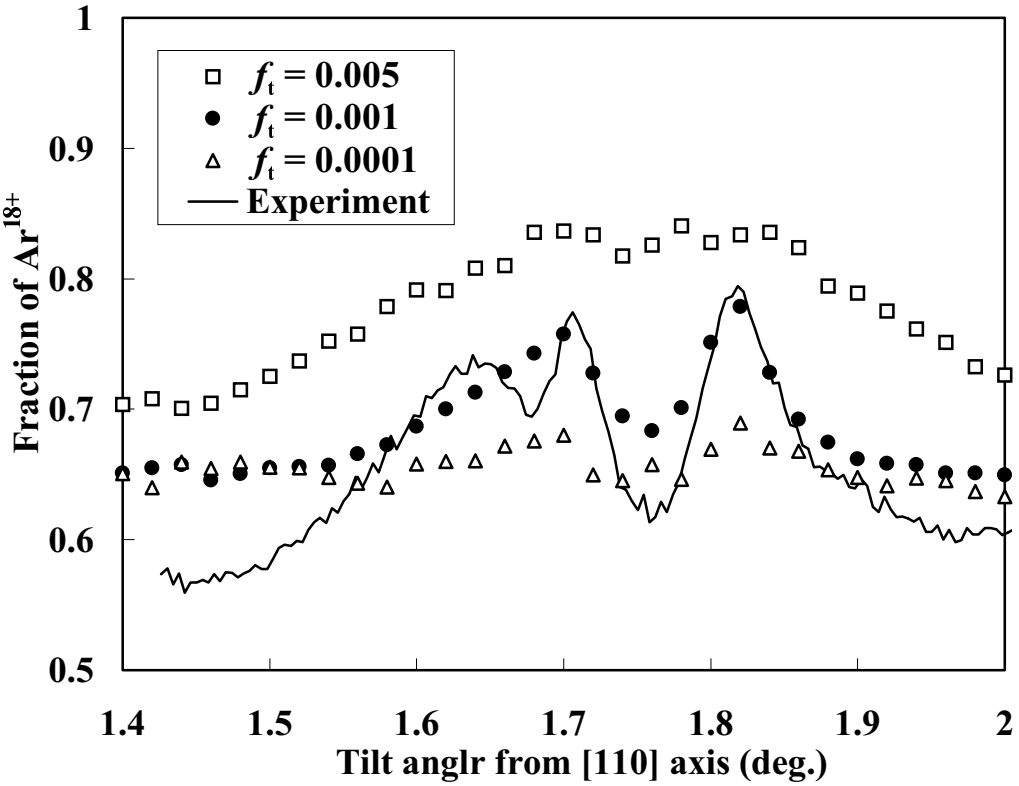

Fig.4.19 Simulated fraction of ionized Ar^{18+} ions as a function of the tilt angle from [110] axis.

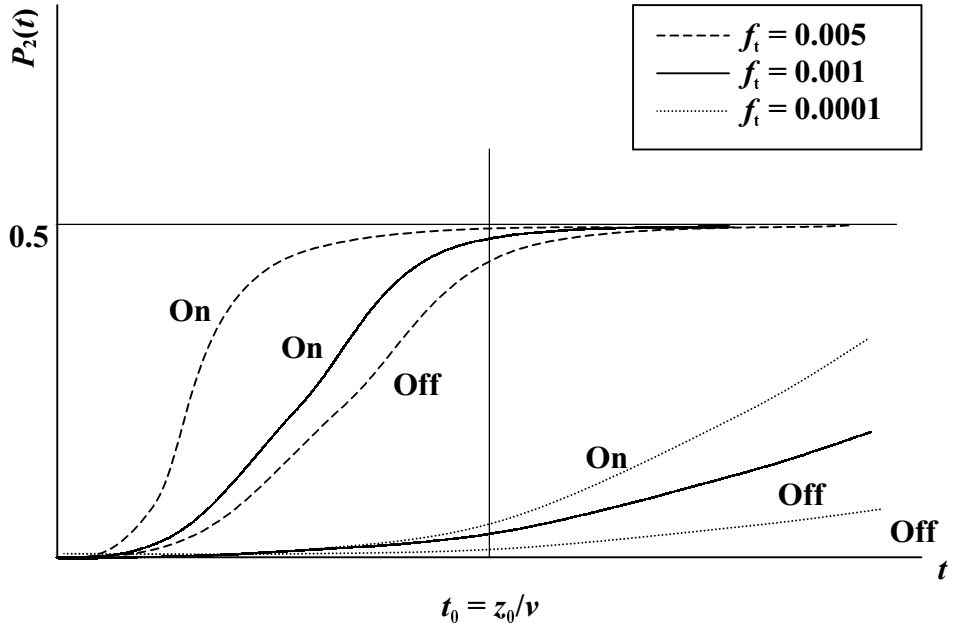

Fig.4.20 Time evolution of probability that the ion exists in n = 2 states for several values of f_t, and for on- and off-resonance.

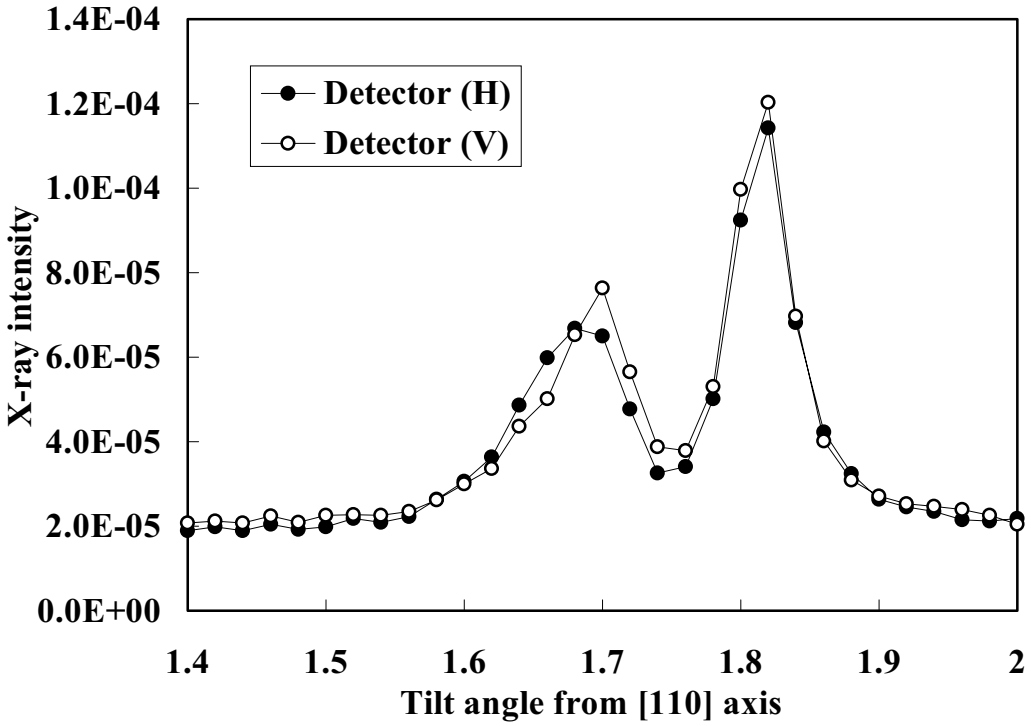

Fig.4.21 Simulated result of detected X-rays by the detectors (H) and (V). The vertical axis is the X-ray intensity per ion.

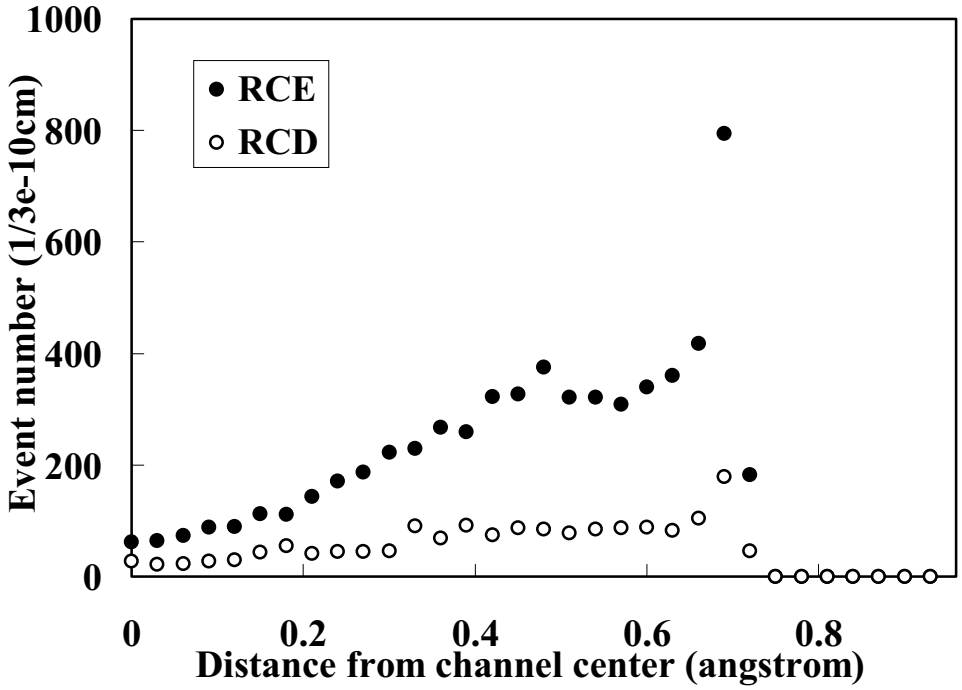

Fig.4.22 Event number per unit length of RCE and RCD as a function of the distance from the channel center for channeled ions with the oscillation amplitude of 0.72 Å (injected into the crystal in parallel to the channel plane) under the resonance condition of $\theta = 1.82°$.

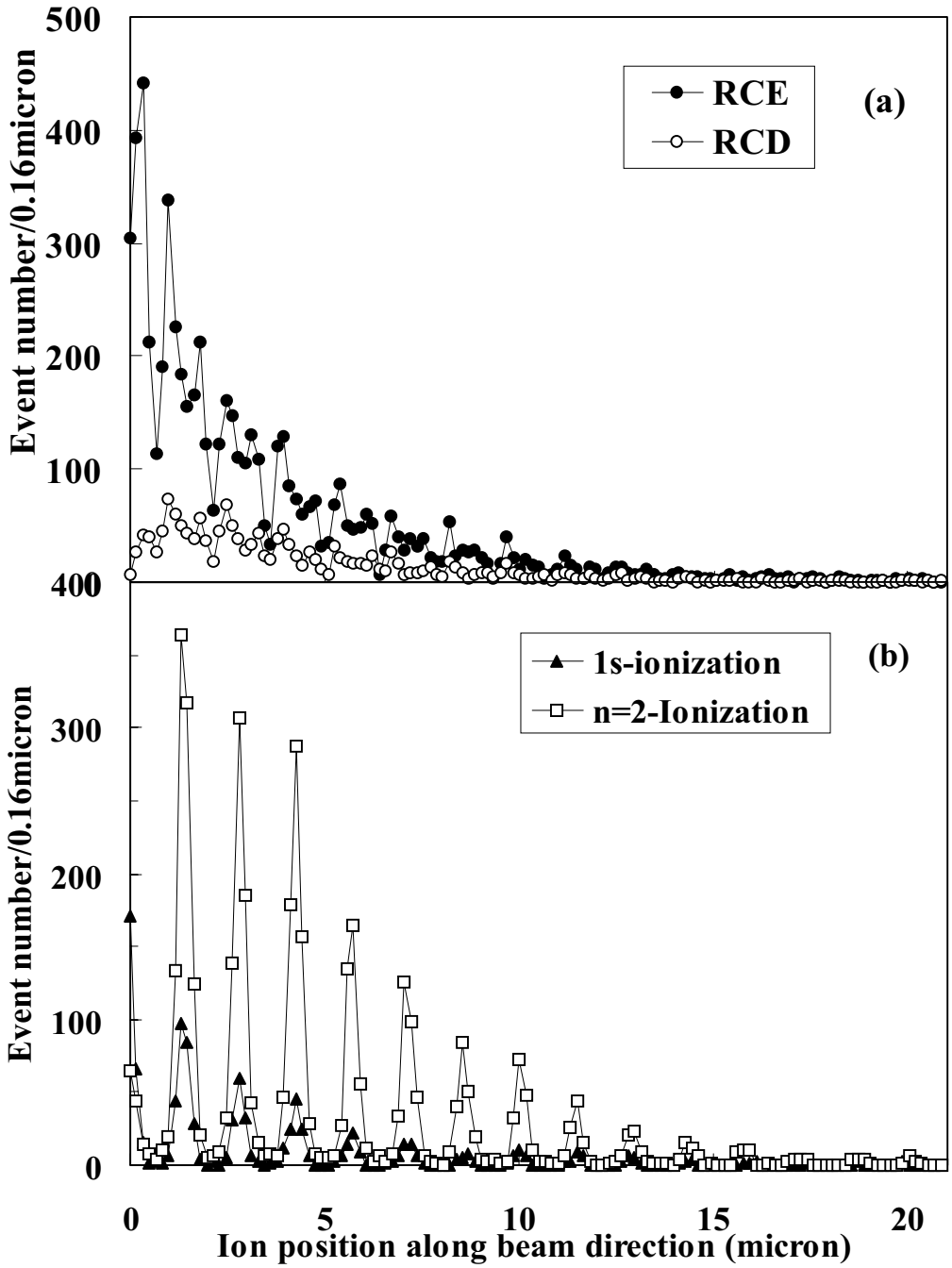

Fig.4.23 Event number per unit length of (a) RCE, RCD, (b) 1s-ionization and ionization from n = 2 states as a function of the ion position along the beam direction for channeled ions with the oscillation amplitude of 0.72 Å (injected into the crystal in parallel to the channel plane under the resonance condition of θ = 1.82°.

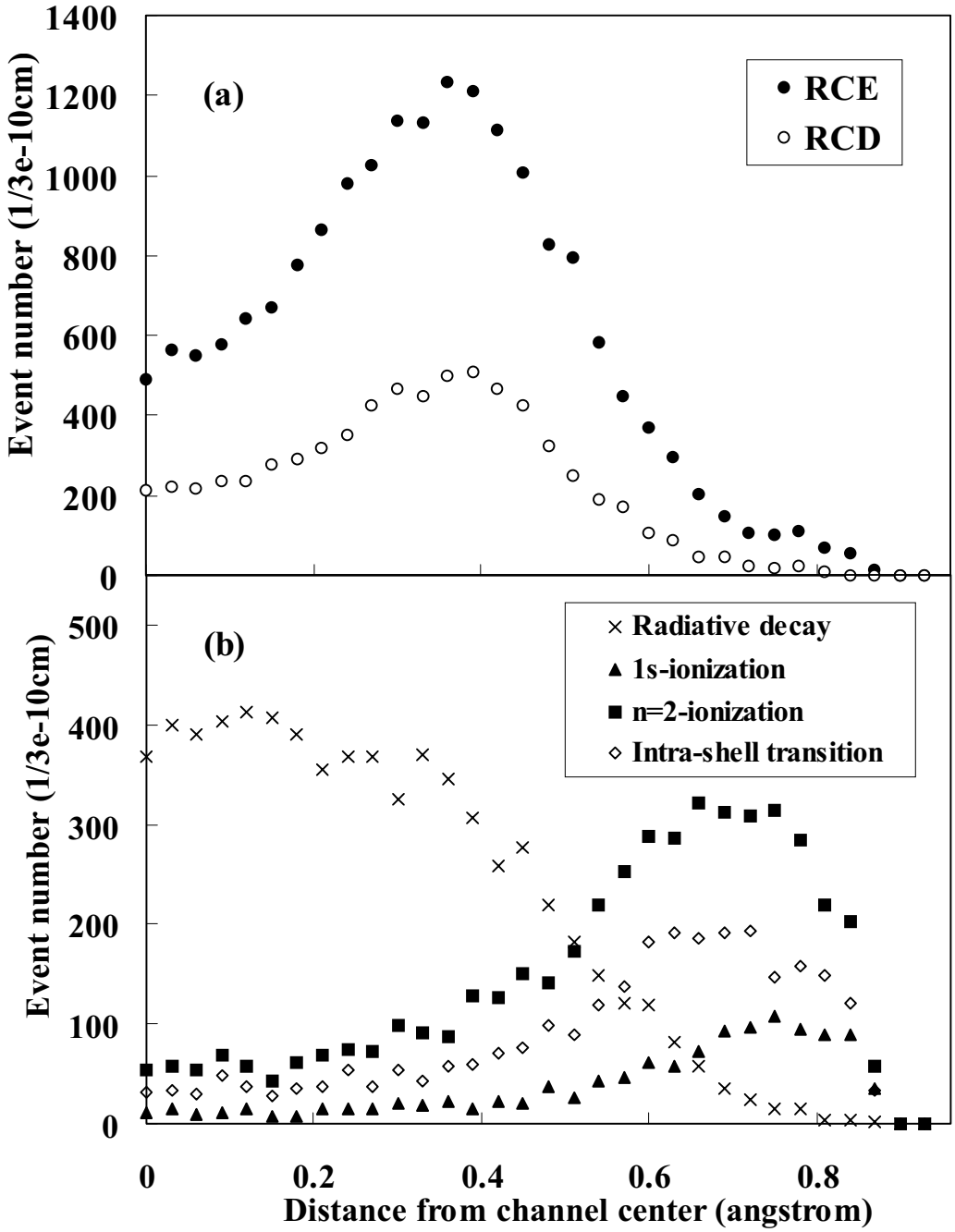

Fig.4.24 Event number per unit length of (a)RCE, RCD (b) 1s-ionization, ionization from n = 2 states, Intra-shell transition and radiative decay as a function of the distance from the channel center for channeled ions with all trajectories under the resonance condition of $\theta = 1.82°$.

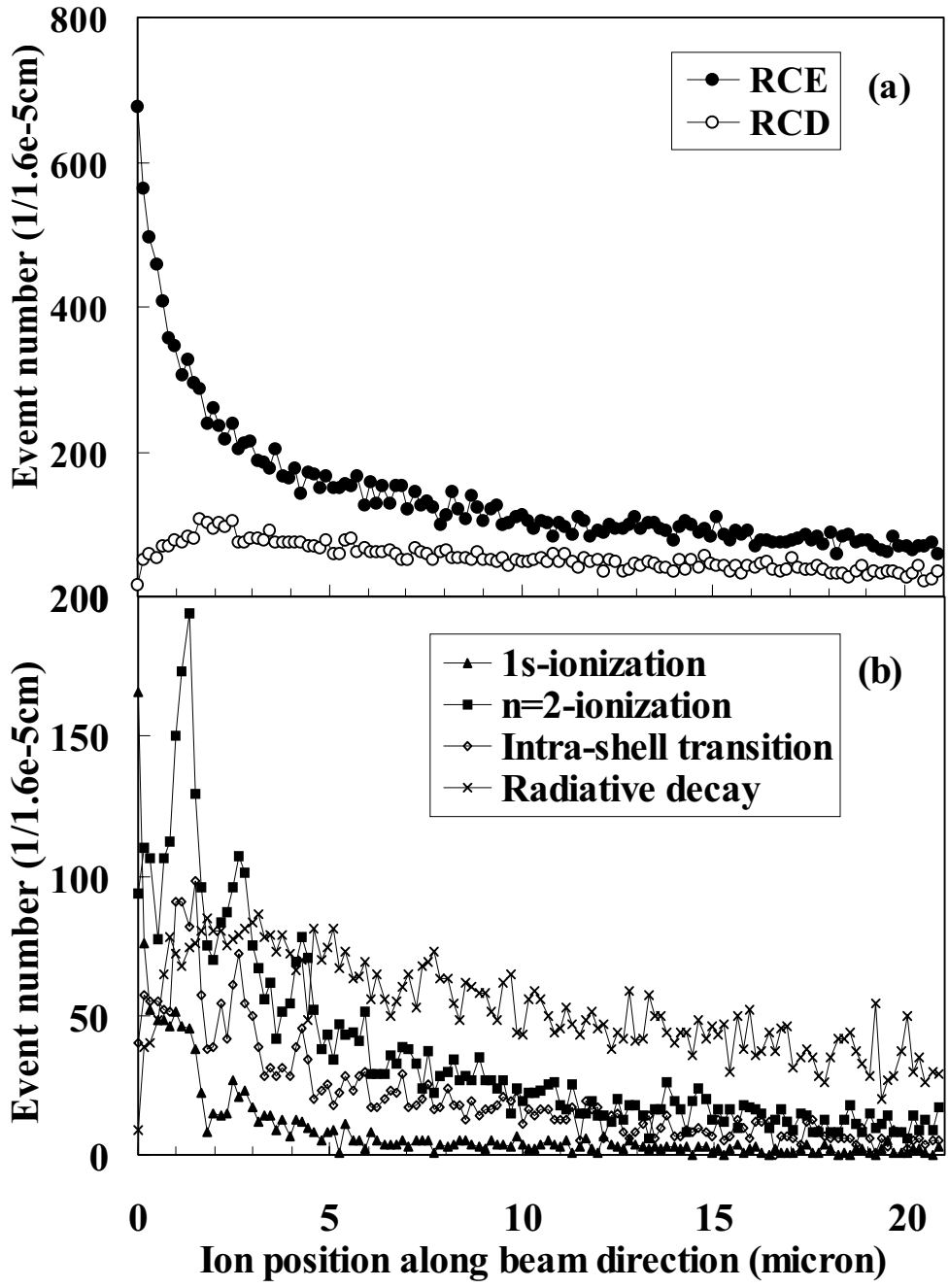

Fig.4.25 Event numbers per length of (a) RCE, RCD, (b) 1s-ionization, ionization from n = 2 states, intra-shell transition and radiative decay as a function of the ion position along the beam direction for channeled ions with all trajectories under the resonance condition of $\theta = 1.82°$.

5. Summary

5.1. Channeling experiment

Energy depositions of 290 MeV/u C^{6+} ions and 390 MeV/u Ar^{17+} ions in a Si crystal for random incidence and under [110] axial and (004), (220) and (111) planar channeling conditions were measured adopting a totally depleted silicon detector (SSD) as a target crystal. The energy depositions of the [110] axial, and (004), (220) and (111) planar channeled C^{6+} ions in 524 μm Si crystal were reduced to 5.8, 7.7, 6.6 and 5.2 MeV, respectively, compared with 11.8 MeV for random incidence. The angular divergence of transmitted ions under the channeling condition became smaller compared with the random incident case. A calculation of the energy deposition of planar channeled ions was also performed adopting a stopping power formula based on the Lindhard's theory. A fitting parameter, *f*, in the formula was selected so that the peak position agrees with the experimental result. The shape of the simulated energy deposition spectra well reproduced those of the measured spectra. In the calculation, an effect of escaped electrons produced by the collision with the projectile, *i.e.* the difference between the energy loss and the energy deposition, was taken into account, which was evaluated from a Monte Carlo simulation for a random incident case. This effect amounts to 16 percent of the energy loss for 390 MeV/u Ar ions with 19.4 μm Si target. The relation between the energy deposition and the oscillation amplitude of the channeled ion was also obtained from the calculation.

A charge state distribution of Ar ions transmitted through 94.7 μm crystal under the channeling condition was also measured. For random incidence, most of the incident Ar^{17+} ions were ionized, but, a fraction of survived Ar^{17+} ions increases to 20 percent for (220) planar channeling case. At the same time, energy depositions of Ar ions with the exit charge of 18+ and 17+ (charge-frozen) were measured.

5.2. Observation of RCE

Resonant coherent excitation (RCE) from 1s to n = 2 states of 390 MeV/u hydrogen-like Ar ions planar channeled in a Si crystal was observed through measurements of the charge state distribution, convoy electrons and de-excitation X-rays. By measuring the energy deposition in coincidence with the charge state of transmitted ions, the impact-parameter dependent RCE profile was obtained, which reflects the energy level splitting of n = 2 states. A splitting between Level 3 and 4 is so narrow that they were not resolved in the experiment. The profile shows that the RCE probability becomes larger as the increase of the oscillation amplitude, and the RCE occurs mainly near the turning point of the ion trajectory. The resonance profiles for convoy electrons and de-excitation X-rays were also obtained, which have different features from that for the charge state. This result reflects the nature of n = 2 state which are the linear combination of 2s, $2p_x$, $2p_y$ and $2p_z$ states. The dominance of 2s state in Level 1 and 2 resulted in the suppression of the left peak for the X-ray profile. The anisotropy of the de-excitation X-ray emission was not observed through the measurement by two detectors located on the horizontal and vertical planes to the channel plane. It can be explained as follows. Only the channeled ions with the small oscillation amplitude contribute to the X-ray profile, because the ionization process is dominant near the channel wall. The fraction of 2s, $2p_x$, $2p_y$ and $2p_z$ components in

Level 1, Level 2 and the state of $J = 3/2$ (Level 3 and 4) is almost 1 : 1 : 1 near the channel center. Therefore, only an isotropic distribution of X-rays can be observed.

A Monte Carlo simulation for atomic process of the channeled ions under the RCE condition was performed. The probability of the coherent process was given at each step, that is, the process was treated as "incoherent-like". However, the transition probability and the transition energy, which depend on the ion position, were included calculating the ion trajectory exactly. As a result, a good agreement with the experimental resonance profiles for charge state and de-excitation X-rays was obtained. By the simulation, it was confirmed that most of the RCE take place near the entrance surface. Moreover, the simulation indicates that the radiative decay primarily occurs in a region of $x < 0.5$ Å, and the intra-shell transition which tends to stir the composition of 2s, $2p_x$, $2p_y$ and $2p_z$ components mostly occur in a region of $x > 0.5$ Å. That is to say, the intra-shell transition has no effect for the X-ray profile, which supports the above discussion about the experimental result.

In the present experiment, the energy level splitting of $n = 2$ states ($J = 1/2$ and $J = 3/2$) was clearly observed. The measured resonance peak width is 0.94 eV, which is mainly due to the energy fluctuation and the angular divergence of the incident ion. Using the fitting by the Gaussian shape to the resonance peak, the transition energy can be obtained with a precision of 0.04 eV, if the absolute ion energy is determined with the precision less than 2.3×10^{-5}. This measurement has a possibility to give a new method of the atomic spectroscopy, *e.g.*, the determination of the 1s Lamb shift, in the high precision.

Appendix

1. Derivation of relativistic Bethe's stopping power formula

Bethe extended his stopping power formula for relativistic ions. Applying the first Born approximation, the differential cross section in Eq.(2.3) is rewritten as

$$d\sigma_{\mathrm{FB}} = \frac{2\pi Z_1^2 e^4}{m\upsilon^2}\left\{\frac{\left|F_{n0}(\boldsymbol{K})^2\right|}{Q^2(1+Q/2mc^2)^2} + \frac{\left|\boldsymbol{\beta}_t\cdot\boldsymbol{G}_{n0}(\boldsymbol{K})\right|^2}{[Q(1+Q/2mc^2)-(E_n-E_0)^2/2mc^2]^2}\right\}\left(1+\frac{Q}{mc^2}\right)dQ, \tag{A.1}$$

where $\boldsymbol{\beta}_t = \boldsymbol{\beta} - (\boldsymbol{\beta}\cdot\boldsymbol{K})\boldsymbol{K}/K^2$ is the component of $\boldsymbol{\beta}$ perpendicular to $\boldsymbol{K}$, $\boldsymbol{\beta} = \boldsymbol{v}/\mathrm{c}$,

$$F_{n0}(\boldsymbol{K}) = \left\langle n\left|\sum_j \exp(i\boldsymbol{K}\cdot\boldsymbol{r}_j)\right|0\right\rangle, \tag{A.2}$$

$$\boldsymbol{G}_{n0}(\boldsymbol{K}) = \sum_j \left\langle n\left|\boldsymbol{\alpha}_j \exp(i\boldsymbol{K}\cdot\boldsymbol{r}_j)\right|0\right\rangle, \tag{A.3}$$

$\boldsymbol{\alpha}_j$ is a relativistic current operator for the j-th electron. In the relativistic calculation, the relation between the variable, Q, and momentum transfer, $\hbar\boldsymbol{K}$, is modified as

$$\hbar^2K^2 = 2mQ(1+Q/2mc^2), \tag{A.4}$$

and the maximum and minimum energy transfers, $Q_{\max}$ and $Q_{\min}$, are given by

$$Q_{\max} = 2m\upsilon^2\gamma^2, \quad Q_{\min} = (E_n - E_0)^2/2m\upsilon^2, \tag{A.5}$$

In the same way as the non-relativistic calculation, the range of Q for the integration is divided into two parts by the value of Q_0. For small Q range, $Q_{\min}<Q<Q_0$, the matrix elements, $F_{n0}(\boldsymbol{K})$ and $\boldsymbol{G}_{n0}(\boldsymbol{K})$, can be approximated as

$$\left|F_{n0}(\boldsymbol{K})\right|^2 \sim K^2\left|\left\langle n\left|\sum_j x_j\right|0\right\rangle\right|^2, \tag{A.6}$$

$$\left|\beta_t\cdot\boldsymbol{G}_{n0}(\boldsymbol{K})\right|^2 \sim \beta_t^2(E_n-E_0)^2\left|\left\langle n\left|\sum_j y_j\right|0\right\rangle\right|^2 \Big/ \hbar^2c^2, \tag{A.7}$$

where x_j and y_j are coordinates of the j-th electron in the directions of $\boldsymbol{K}$ and $\boldsymbol{\beta}_t$, respectively. Substituting Eqs.(A.6) and (A.7) into Eq.(A.1), we obtain

$$d\sigma_{\mathrm{FB}} = \frac{2\pi Z_1^2e^4}{m\upsilon^2}\left\{\frac{K^2\left|\left\langle n\left|\sum_j x_j\right|0\right\rangle\right|^2}{Q^2} + \frac{2m\beta_t^2\beta^2Q_{\min}\left|\left\langle n\left|\sum_j y_j\right|0\right\rangle\right|^2/\hbar^2}{(Q-\beta^2Q_{\min})^2}\right\}dQ,$$

$$= \frac{4\pi Z_1^2e^4}{\hbar^2\upsilon^2}\left\{\frac{\left|\left\langle n\left|\sum_j x_j\right|0\right\rangle\right|^2}{Q}dQ + \frac{\beta^4\left|\left\langle n\left|\sum_j y_j\right|0\right\rangle\right|^2(1-X^2)}{(1-\beta^2X)^2}dX\right\}, \tag{A.8}$$

where the approximation of $Q<<mc^2$ is used, and β_t can be written as

$$\beta_t^2 = \beta^2(1-Q_{\min}^2/Q^2). \tag{A.9}$$

The parameter $X = Q_{\min}/Q$ is introduced in Eq.(A.8), where the range of integration of X is from $Q_{\min}/Q_0(\sim 0)$ to 1. Then, the stopping power from the range of $Q_{\min}<Q<Q_0$ is given by

$$S_{Q<Q_0} = N\sum_n (E_n - E_0)\int d\sigma_{\mathrm{FB}}$$
$$= \frac{2\pi N Z_1^2 Z_2 e^4}{m\upsilon^2}\left\{\ln\frac{2mv^2 Q_0}{I^2} + \ln\frac{1}{1-\beta^2} - \beta^2\right\}. \tag{A.10}$$

For large Q range, $Q_0<Q<Q_{\max}$, the electron in the initial state can be regarded as a free electron, and the variable, Q, corresponds to the energy transfer from the ion to the electron. Adopting the Dirac wave functions averaged for up and down spin orientations into Eq.(A.2) and Eq.(A.3), the matrix elements are

$$\left|F_{n0}(\boldsymbol{K})\right|^2 \sim \frac{1+Q/2mc^2}{1+Q/mc^2}, \tag{A.11}$$

$$\left|\boldsymbol{\beta}_{\mathrm{t}}\cdot\boldsymbol{G}_{n0}(\boldsymbol{K})\right|^2 \sim \beta_{\mathrm{t}}^2\,\frac{Q/2mc^2}{1+Q/2mc^2}. \tag{A.12}$$

In this Q-range, β_{t} can be written as

$$\beta_{\mathrm{t}}^2 = \beta^2 - \frac{Q/2mc^2}{1+Q/2mc^2}. \tag{A.13}$$

With the substitution of Eqs.(A.11)–(A.13), Eq.(A.1) results in

$$d\sigma_{\mathrm{FB}} = \frac{2\pi Z_1^2 e^4}{m\upsilon^2 Q^2}\left(1 - \frac{\beta^2 Q}{2m\upsilon^2\gamma^2}\right)dQ, \tag{A.14}$$

where the second term of Eq.(A.14) is originated from the electron spin. The stopping power from the range, $Q_0<Q<Q_{\max}$, is obtained as,

$$S_{Q>Q_0} = N\int_{Q_0}^{Q_{\max}}\sum_n (E_n - E_0)d\sigma_{FB},$$
$$= \frac{2\pi N Z_1^2 Z_2 e^4}{m\upsilon^2}\left(\ln\frac{2m\upsilon^2\gamma^2}{Q_0} - \beta^2\right). \tag{A.15}$$

Summing Eq.(A10) and Eq.(A15), the total stopping power becomes

$$S = \frac{4\pi N Z_1^2 Z_2 e^4}{m\upsilon^2}\left(\ln\frac{2m\upsilon^2\gamma^2}{I} - \beta^2\right), \tag{A.16}$$

which is called “relativistic Bethe’s formula”.

2. Channeling of electrons

In the case of the channeling of ions, a classical treatment can be applied. However, it is not always possible to define the classical trajectory for channeled electrons because of the large de Broglie wave length. The number of the quantum state for the particle bound to the channel plane is given by

$$n_{\mathrm{p}} = \frac{1}{h}\oint p(x)dx,$$
$$= \frac{4}{h}\int_0^{d_{\mathrm{p}}/2}\sqrt{2MU_{\mathrm{p}}(x)}dx, \tag{A.17}$$

where $p(x)$ is the momentum component along x-axis, and M is a mass of channeled particle. Approximating the planar potential, $U_{\mathrm{p}}(x)$, as the harmonic oscillator type potential with using the relation of Eq.(2.62), $U_{\mathrm{p}}(x)$ is expressed as

$$U_{\mathrm{p}}(x) = \frac{E\psi_{\mathrm{p}}^2}{a_{\mathrm{TF}}^2} x^2 . \tag{A.18}$$

Substituting Eq.(A.18) into Eq.(A.17), the number of the quantum state is derived as

$$n_{\mathrm{p}} = \frac{pd_{\mathrm{p}}^2 \psi_{\mathrm{p}}}{2ha_{\mathrm{TF}}} . \tag{A.19}$$

In the case of axial channeling, the number of the state is given by

$$n_{\mathrm{a}} = n_{\mathrm{p1}} n_{\mathrm{p2}}, \tag{A.20}$$

where n_{p1} and n_{p2} are the numbers of the quantum state for planar channelings that the planes including the noticed axis are orthogonal. The trajectory of the channeled particle can be classically defined for n_{p} (or n_{a}) much larger than unity. If n_{p} (n_{a}) approaches to unity, the electron diffraction effect becomes important. Spatial distributions of transmitted (a)2.43 MeV protons along Ge <111> axis and (b)1 MeV electrons along Cu <111> axis are shown in Fig.A.1. We can see the characteristic “star pattern”, which is seen for classically channeled particles, in case (a). On the contrary, the diffraction pattern appears in the case (b). The numbers of the quantum states for the case (a) and (b) are ~100 and ~1.6, respectively. The value for the classification between the channeling and the diffraction was determined to n_{a} ~3 from the experimental results, which depends more or less on the kind of axis [89].

The electron penetrating a crystal is described as the linear combination of the Bloch waves. For high energy electron, *i.e.*, n_{p} or n_{a} >>1, many Bloch waves are excited, and the classical description is permitted. Planer potentials for positron and electron are shown in Fig.A.2. The potential dip for positrons is inverted to the potential peak for electrons. Therefore, channeled electrons with small oscillation amplitudes spend a long time near the channel wall, and loose more energies compared with the random incident case. On the contrary, the energy loss of channeled electron with large oscillation amplitudes is smaller that that for random incidence. For low energy case, *i.e.*, n_{p} or n_{a} ≤1, only two Bloch waves are effectively excited [90,91]. One of them has nodes on the channel wall, and the other has nodes on the channel center. The former and the latter result in the abnormal transmission and absorption, respectively.

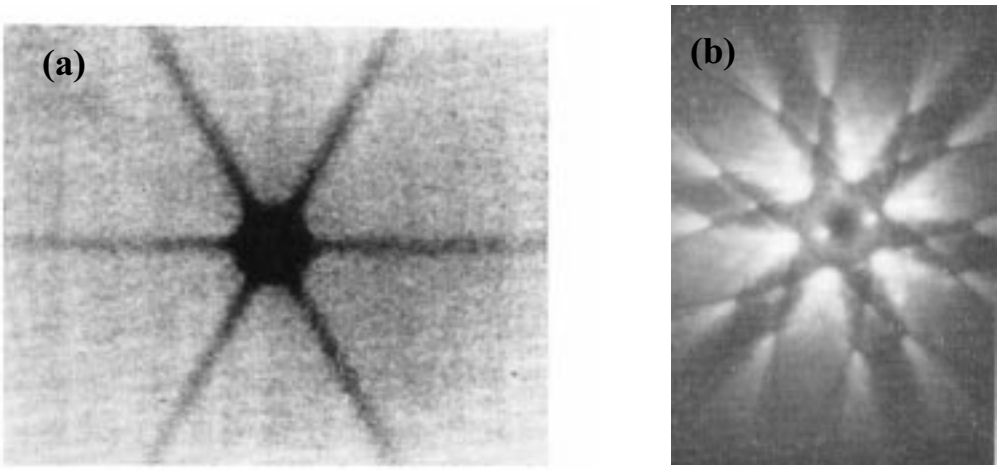

Fig.A.1 Spatial distributions of transmitted (a)2.43 MeV proton along Ge <111> axis and (b)1 MeV electron along Cu <111> axis.

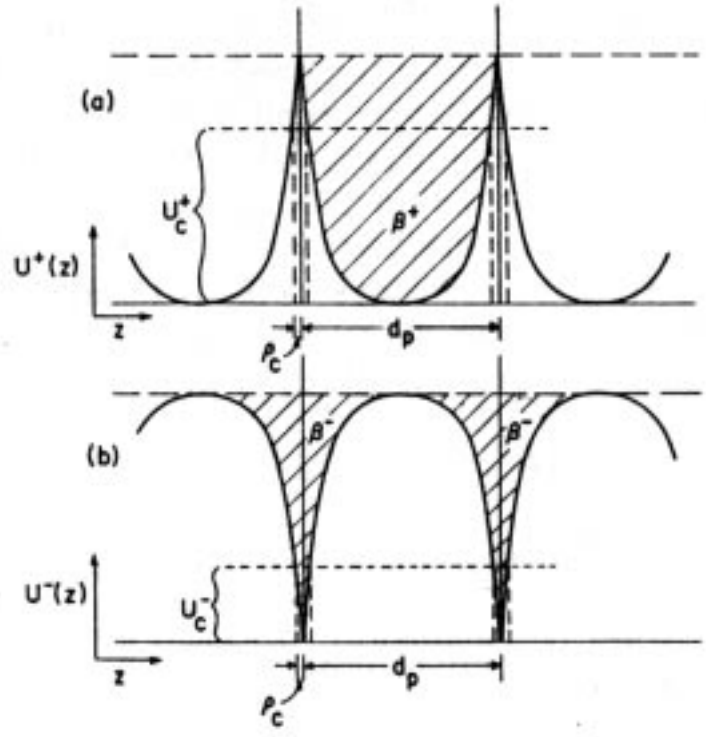

Fig.A.2 Planar potential for (a) positron and (b) electron.

Acknowledgements

I would like to express my hearty thanks to my supervisor, Prof. Y. Yamazaki (Univ. of Tokyo, RIKEN), who introduced me this exciting theme. He gave me continuous encouragement and appropriate advice during this investigation.

I would like to express my sincere gratitude to Prof. K. Komaki (Univ. of Tokyo) who gave me many significant suggestions about the method of the simulation and the knowledge about crystal and channeling effect, etc. My simulation owes his calculated results of the transition amplitude and the transition energy in the crystal field.

I am very thankful to Prof. T. Azuma (Univ. of Tsukuba) who gave me various guidance and advice about experimental method and the analysis of the experimental data since he was a research associate of the laboratory.

I would like to express my best regards to Prof. S. Datz (Oak Ridge National Laboratory) for his precise and important suggestion about the experiment.

I would like to thank Mr. Y. Takabayashi (Univ. of Tokyo). This study is indebted his essential works as a collaborator.

I am grateful to collaborators at HIMAC, Dr. T. Murakami, Dr. E. Takada, Dr. A. Kitagawa, Dr. M. Torikoshi and Dr. M. Sano (Japan Atomic Research Institute, Kansai), who play an essential role in this investigation.

I acknowledge Dr. H. A. Torii (Univ. of Tokyo), a research associate of the laboratory. Discussions with him about the RCE simulation were very significant.

I appreciate Mr. T. Katoh and T. Kamiya, engineers at HIMAC, and also thank operators of HIMAC for their great supports.

I would like to thank Dr. H. Higaki, Dr. K. Franzen Yoshiki, Mr. T. Ichioka, Mr. Y. Morishita, Mr. Y. Iwai, Mr. N. Okabayashi, Mr. N. Kuroda, Mr. D. Murakoshi, Ms. A. Endoh (University of Tokyo), Mr. K. Kuroki (National Research Institute of Police Science), Dr. N. Ohshima (RIKEN), Dr. S. Ninomiya (Univ. of Ohsaka), Dr. K. Maki (National Institute of Bio-science and Human-technology), Mr. T. Takahira, Mr. Y. Tsuruta (Hitachi corp.), H. Matsushima (Fuji-film corp.), who enriched my life at Komaba.

Finally, I would like to express my appreciation to my parents, Katsuhiko Ito and Keiko Ito, who supported my student life in Tokyo.

References

[1] G. Dearnaley, “CHANNELING”, Edited by D. V. Morgen (John Wiley & Sons, 1973).

[2] D. S. Gemmel, Rev. Mod. Phys. **46**,129 (1974).

[3] S. Datz, J. Gomez del Campo, P. F. Dittner, P. D. Miller, and J. A. Biggerstaff, Phys. Rev. Lett. **38**, 1145 (1977).

[4] S. Andriamonje, et al., Phys. Rev. **A54**, 1404 (1996).

[5] J. U. Andersen, J. Chevallier, G. C. Ball, W. G. Davies, J. S. Forster, J. S. Geiger, J. A. Davies, H. Geissel, and E. P. Kanter, Phys. Rev. **A54**, 624 (1996).

[6] A. L’hoir, *et al*., Nucl. Instr. and Meth. **B48**, 145 (1990).

[7] T. Azuma, K. Komaki, M. Yamagata, Y. Yamazaki, M. Sekiguchi, T. Hattori, and T. Hasegawa, Nucl. Instr. and Meth. **B115**, 310 (1996).

[8] V. V. Okorokov, JETP Lett. **2**,111 (1965); Sov. J. Nucl.Phys. **2**, 719 (1966).

[9] S. Datz, C. D. Moak, O. H. Crawford, H. F. Krause, P. F. Dittner, J. Gomez del Campo, J. A. Biggerstaff, P. D. Miller, P. Hvelplund, and K. Knudsen, Phys. Rev. Lett. **40**, 843 (1978).

[10] F. Fujimoto, K. Komaki, A. Ootuka, E. Vilalta, Y. Iwata, Y.Hirao, T. Hasegawa, M. Sekiguchi, A. Mizobuchi, T. Hattori, and K. Kimura, Nucl. Instr. and Meth. **B33**, 354 (1988).

[11] O. H. Crawford and R. H. Ritchie, Phys. Rev. **A20**, 1848 (1979).

[12] Y. Yamashita and Y. H. Ohtsuki, Phys. Rev. **B22**, 1183 (1980).

[13] O. É. Krivosheev and Yu. L. Pivovarov, JETP Lett. 56, 240 (1992).

[14] F. J. García de Abajo and P. M. Echenique, Phys. Rev. Lett. **76**, 1856 (1996).

[15] A. Salin, A. Arnau, and P. M. Echenique, Phys. Rev. **A57**, 2772 (1998).

[16] H. F. Krause and S. Datz, Adv. in Atomic, Mol. And Opti. Phys. **37**, 139 (1996).

[17] J. U. Andersen, G. C. Ball, J. Chevallier, J. A. Davies, W. G. Davies, J. S. Forster, J. S. Geiger, and H. Geissel, Nucl. Instr. and Meth. **B119**, 292 (1996).

[18] K. Kimura, J. P. Gibbson, S. B. Elston, C. Biedermann, R. DeSerio, N. Keller, J. C. Levin, M. Breinig, J. Burgdörfer, and A. Sellin, Phys. Rev. Lett. **66**, 25 (1991).

[19] S. Datz, *et al.*, Radiat. Eff. and Def. in Solids **117** (1991).

[20] S. Datz, P. F. Dittner, H. F. Krause, C. R. Vane, O.H. Crawford, J. S. Forster, G. S. Ball, W. G. Davies, and J. S. Geiger, Nucl. Instr. and Meth. **B100**, 272 (1995).

[21] J. S. Forster, G. C. Ball, W. G. Davies, J. S. Geiger, J. U. Andersen, J. A. Davies, H. Geissel, and F. Nickel, Nucl. Instr. and Meth. **B107**, 27 (1996).

[22] L. C. Northcliffe and R. F. Schilling, Nucl. Data Tables. Sec.**A7**, 233 (1970).

[23] H. Bethe, Ann. Phys. (Leipzig) **5**, 325 (1930).

[24] H. Bethe, Z. Phys. **76**, 293 (1932).

[25] U. Fano, Ann. Rev. Nucl. Sci. **13**, 1 (1963).

[26] N. Bohr, Philos. Mag. **25**, 10 (1913); Philos. Mag. **30**, 581 (1915).

[27] A. H. Sørensen, Phys. Rev. **A55**, 2896 (1997).

[28] W. H. Barkas, J. N. Dyer, and H. H. Heckman, Phys. Rev. Lett. **11**, 26 (1963).

[29] J. D. Jackson and R. L. McCarthy, Phys. Rev. **B6**, 4131 (1972).

[30] J. C. Ashley, R. H. Ritchie, and W. Grandt, Phys. Rev. **B5**, 2393 (1972).

[31] H. H. Andersen, J. F. Bak, H. Knusen, and B. R. Nielsen, Phys.Rev. **A16**, 1929 (1977).

[32] H. Bichsel, University of Southern California, Phys. Dept. Tech. Report No.3 (1961); USC Report, USC-136-120 (1967).

[33] E. Bonderup, Mat. Fys. Medd. Dan. Vid. Selsk. **35**, no.17 (1967)
[34] N. F. Mott, Proc. R. Soc. Lond. **A124**, 42 (1929); Proc. R. Soc. Lond. **A135**, 42 (1932).
[35] J. Lindhard and A. H. Sørensen, Phys. Rev. **A53**, 2443 (1996).
[36] C. Scheidenberger *et al*., Phys. Rev. Lett. **73**, 50 (1994).
[37] R. M. Sternheimer, S. M. Seltzer, and M. J. Berger, Phys. Rev. **B26**, 6067 (1982).
[38] C. Scheidenberger *et al*., Phys. Rev. Lett. **77**, 3987 (1996).
[39] L. Landau, J. Phys. U.S.S.R. **8**, 201 (1944).
[40] H. D. Maccabee, M. R. Raju, and C. A. Tobias, Phys. Rev. **165**, 469 (1968).
[41] T. Tanabe, R. Ito, and S. Okabe, Nucl. Instr. and Meth **103**, 85 (1972).
[42] H. Iskef, J. W. Cunningham, and D. E. Watt, Phys. Med. Biol. **28**, 535 (1983).
[43] F. Hubert, R. Bimbot, and H. Gauvin, Atomic Data & Nucl. Data Tables **46**, 1 (1990).
[44] J. S. Marshall and A. G. Ward, Can. J. Research **A15**, 39 (1937).
[45] G. S. Khandelwal, B. H. Choi, and E. Merzbacher, At. Data **1**, 103 (1969).
[46] B. H. Choi, Phys. Rev. **A7**, 2056 (1973).
[47] J. H. Scofield, Phys.Rev. **A18**, 936 (1978).
[48] S. P. Khare and J.W. Wadehra, Can. J. Phys. **74**, 376 (1996).
[49] B. Feinberg, *et al*., Phys. Rev. **A47**, BR2370 (1993).
[50] J. R. Oppenheimer, Phys. Rev. **31**, 349 (1928).
[51] M. C. Brinkman and H. A. Kramers, Proc. Acad. Sci. Amsterdam **33**, 973 (1930).
[52] H. W. Schnopper, H. D. Betz, J. P. Delvaille, K. Kalata, A. R. Sohval, K. W. Jones, and H. E. Wegner, Phys.Rev. Lett. 29, 898 (1972).
[53] G. Raisbeck and F. Yiou, Phys.Rev. A4, 1858 (1971).
[54] Y. K. Kim, K. Cheng, Phys. Rev. A22, 61 (1980).
[55] R. Cabrera-Trujillo, S. A. Cruz, J. Oddershede, and J. R. Sabin, Phys. Rev. **A55**, 2864 (1997).
[56] P. Sigmund, Nucl. Instr. and Meth. **B69**, 113 (1992).
[57] M. Breinig, *et al.*, Phys. Rev. **A25**, 3015 (1982).
[58] J. P. Gibbson, et al., Phys.Rev.Lett. **67**, 481 (1991).
[59] J. Burgdörfer, M. Breinig, S. B. Elston, and I. A. Sellin, Phys. Rev. **A28**, 3277 (1983).
[60] Y. Takabayashi, T. Ito, T. Azuma, K. Komaki, Y. Yamazaki, H. Tawara, M. Torikoshi, A. Kitagawa, E. Takada, and T. Murakami, Physica Scripta, **T80**, 249 (1999).
[61] H. Rothard, D. H. Jakubaßa-Amundsen, and A. Billebaud, J. Phys. **B31**, 1563 (1998).
[62] P. K. Rol, J. M. Fluit, F. P. Viehböck, and M. DeJong, Proc. Fourth Inter. Conf. On Ionization Phenomena in Gases, edited by N. R. Nilsson, p.257 (North Holland, Amsterdam, 1960).
[63] J. A. Davies, J. Friensen, and J. D. McIntyre, Can. J. Chem. **38**, 1526 (1960); J. A. Davies, J. D. McIntyre, R. L. Cushing, and M. Lounsbury, Can J. Chem. **38**, 1535 (1960).
[64] J. Lindhard, Mat. Fys. Medd. Dan. Vid. Selsk. **34**, no.14 (1965).
[65] J. Lindhard and A. Winther, Mat. Fys. Medd. Vid. Selsk. **34**, no.4 (1964).
[66] A. R. Sattler and G. Dearnaley, Phys. Rev. Lett. **15**, 59 (1965).
[67] B. R. Appleton, C. Erginsov, and W. M. Gibson, Phys. Rev. **161**, 330 (1967).

[68] H. Esbensen and J. A. Golovchenko, Nucl. Phys. **A298** 382 (1978).
[69] H. Esbensen *et al.*, Phys. Rev. **B18**, 1039 (1978).
[70] M. T. Robinson, Phys. Rev. **179**, 327 (1969).
[71] S. Datz, C. D. Moak, T. S. Noggle, B. R. Appleton, and H. O. Lutz, Phys. Rev. **179**, 315 (1969).
[72] B. R. Appleton, S. Datz, C. D. Moak, and M. T. Robinson, Phys. Rev. **B4**, 1452 (1971).
[73] S. Datz, J. Gomez del Campo, P. F. Dittner, P. D. Miller, and J. A. Biggerstaff, Phys. Rev. Lett. **38**, 1145 (1977).
[74] D. Dauvergne, *et al*., Phys. Rev. **A59**, 2813 (1999).
[75] Y. Iwata, K. Komaki, Y. Yamazaki, M. Sekiguchi, T. Hattori, T. Hasegawa, and F. Fujimoto, Nucl. Instr. and Meth. **B48**, 163 (1990).
[76] K. Komaki, T. Azuma, T. Ito, Y. Takabayashi, Y. Yamazaki, M. Sano, M. Torikoshi, A. Kitagawa, E. Takada, and T. Murakami, Nucl. Instr. and Meth **B146**, 19 (1998).
[77] P. J. Mohr, "Atomic, Molecular, & Optical Physics Handbook" , Edited by G. W. F. Drake, p.341.
[78] T. Ito, T. Azuma, K. Komaki, Y. Yamazaki, T. Murakami, E. Takada, A. Kitagawa, M. Torikoshi and M. Sano, Physica Scripta, **T73**, 345 (1997).
[79] J. P. Rozet, C. Stéphan, and D. Vernhet, Nucl. Instr. and Meth. **B107**, 67 (1996).
[80] T. Ito, T. Azuma, K. Komaki, Y. Yamazaki, M. Sano, M. Torikoshi, A. Kitagawa, E. Takada, and T. Murakami, Nucl. Instr. and Meth. **B135**, 132 (1998).
[81] T. Ito, T. Azuma, K. Komaki, Y. Yamazaki, M. Torikoshi, A. Kitagawa, E. Takada, and T. Murakami, Physica Scripta. **T80**, 256 (1999).
[82] J. F. Ziegler, Handbook of Stopping Cross-Sections for Energetic Ions in All Elements (Pergamon Press, New York, 1980).
[83] Random component under the channeling condition was not taken into account in the simulation in Ref.80.
[84] H. A. Bethe, E. E. Salpeter, "Quantum Mechanics of One- and Two-Electron Atoms" (1957).
[85] S. P. Goldman and G. W. F. Drake, Phys. Rev. **A24**, 183 (1981).
[86] T. Azuma, Y. Ito, K. Komaki, Y. Yamazaki, M. Sano, M. Torikoshi, A. Kitagawa, E. Takada, and T. Murakami, Phys.Rev. Lett. **83**, 528 (1999).
[87] H. F. Beyer, R. D. Deslattes, F. Folkmann, and R. E. LaVilla, J. Phys. **B18**, 207 (1985).
[88] I. V. Mitchell and J. F. Ziegler, "Ion Beam Handbook for Material Analysis", Edited by J. W. Mayer and E. Rimini, (1977).
[89] F. Fujimoto, S. Takagi, K. Komaki, H. Koike, and Y. Uchida, Radiat. Eff. **12**, 153 (1972).
[90] H. Hashimoto, A. Howie, and M. J. Whelan, Proc. Roy. Soc. **A269**, 80 (1962).
[91] A. Howie, Phil. Mag. **14**, 223 (1966).